Mechanistic Understanding and Optimization of Printed Floating Gate Transistors for Chemical Sensing Applications

A Dissertation

SUBMITTED TO THE FACULTY OF

THE UNIVERSITY OF MINNESOTA

BY

Mathew Shaji Thomas

IN PARTIAL FULFILLMENT OF THE REQUIREMENTS

FOR THE DEGREE OF

DOCTOR OF PHILOSOPHY

Advisors: Prof Kevin D. Dorfman and Prof C. Daniel Frisbie

November 2020

Acknowledgements

I would first like to thank my thesis advisors, Prof Daniel Frisbie, and Prof Kevin Dorfman for their support and mentorship throughout my PhD. I owe a special thanks to Dr Scott White, who worked on the FGT platform before me, and trained me on multiple techniques relevant to the device. I would like to thank Dr Fazel Zare Bidoky, Dr Yan Wang, Dr Chang-Hyun Kim, Dr Elliot Schmidt, Dr Abel Demissie, Dr Chris Smith, Dr Julian Sheats, Dr Pranav Agrawal, Dr Xinglong Ren, and Dr Motao Cao for helping me during instrument troubleshooting and for training me for device fabrication and electronic characterization. I would also like to acknowledge the work done by junior students Demetra Adrahtas and Jiayi He in further clarifying the device model and collaborating with the Haynes research group to expand the range of detected targets respectively. I would like to thank the Minnesota Nanofabrication Centre (MNC) for its resources (and by extension, funding sources that support the MNC) and the MNC staff members for their training and troubleshooting help.

I want to thank Dr Greg Haugstad of the Characterization Facility at the University of Minnesota, for carrying out RBS characterization measurements that helped to solidify the results of my work. I would like to acknowledge generous funding from the Michael Baker family foundation, IPRIME at the University of Minnesota, and the Office of Naval research. I would also like to thank my committee members, Prof Chris Leighton, Prof Philippe Buhlmann, and Prof Alon McCormick, for agreeing to volunteer their time to assess my thesis submission and defense.

My parents, Dr Mini and Dr Shaji Thomas, have always supported me throughout my personal and professional journey, and I would like to thank them specially for their unwavering belief in me – the completion of this thesis would certainly not have been possible without them. I would also like to thank Dr Sunil and Dr Susan Thomas for their advice and support during my years living in the United States, as well as many other family members for their encouragement. Finally, I would also like thank all my friends and acquaintances in Minneapolis for enriching my PhD experience with our interactions.

Abstract

Monitoring of human environments, food and health for toxin, carcinogen, allergen and pathogen detection motivates the development of chemical and biosensing platforms that can be deployed in portable field applications. Transistors are suitable transducers for such devices due to their direct electronic response, compact size, and multiplexing capabilities. Electrolyte-gated transistors (EGTs) can provide additional advantages including low voltage operation and the use of fast and simple fabrication methods such as printing. The Floating Gate EGT (FGT) is a sensing derivative of the EGT that utilizes a floating gate to physically separate yet still electronically couple the active sensing area with the transistor. Previous work has shown that FGTs can provide fast and reliable detection of DNA, ricin, and gluten. The aim of this thesis is to investigate fundamental operating mechanisms of the device, improve its sensing capabilities and characterize its design space.

The first study, detailed in chapter 3, implemented well-established acid-terminated self-assembled monolayer (SAM) chemistry on the sensing area to characterize the role of interfacial charge in generating device responses. The shifts observed are further compared with Grahame's equation, derived from Guoy-Chapman double layer theory, and is found to match closely with the experimentally observed shifts. This represents the first quantification of the charge response of floating gate transistor sensors.

Chapter 4 focuses on the detection of capacitance, an important physical quantity for the detection of charge-neutral targets, which has proved to be a challenge for transistor-based sensing devices. In this study, alkylthiol chains of increasing lengths are used to alter the

capacitance of the sensing surface. A simple amplification circuit called an inverter is used to amplify the change in output when the capacitance is perturbed. The FGT platform was found to respond to the capacitive change in a manner distinguishable from the charge-based sensing. This represents the first demonstration of quasi-static capacitance detection in the FGT platform as an alternative to charge detection, a critical issue in transistor-based sensing for neutral targets or in high electrolyte concentrations.

In chapter 5, a theoretical model is derived for the device response and it is utilized to predict the performance and sensitivity of floating gate devices using well-known transistor current equations. The derivation yields 5 parameters, which are combinations of physically understood variables that can effectively tune the response of the device. To validate the model experimentally, SAMs are utilized to generate capacitive and charge-based signals, and the area of the sensing surface is systematically reduced. The model is found to match experimental performance and sensitivities well for higher sensing area capacitances (>1 nF). The model predictions are further extended across large ranges of the relevant parameters to provide general design rules for sensing using thin film organic electronic devices that can be utilized regardless of materials choice.

The overall contribution of this project is to understand quantitatively the mechanisms behind transistor-based detection, specifically charge and capacitance, and provide guidelines for device sizing and materials choice, in order to make transistor-based sensors more accessible and move closer to the overarching goal of a rapid, portable, general purpose sensor for chemical and biosensing in distributed field applications.

Table of Contents

Acknowledgements……...……...…i

Abstract……...iii

List of Figures……....vii

List of Tables……..ix

Statement of the Author's Contributions……..……...x

1. **Introduction and Background**……..……1

   1.1 Introduction to Bio/chemical Detection…….…….....1

   1.2 Transistors, EGTs, and Transistor-based Sensors……...……..4

   1.3 The FGT Platform and Research Plan.……12

2. **Materials and Methods**…….…….…….…….…….……...15

   2.1 Materials…….…….…….…….…….…….……15

   2.2 Techniques……...17

3. **Interfacial Charge Response**…….…….…….…….…….……..21

   3.1 Introduction and Motivation……....……21

   3.2 Experiments…….23

   3.3 Results and Discussion……23

   3.4 Conclusion…….…….…….…….……...30

4. **Quasi-static Capacitance Amplification**……32

   4.1 Introduction and Motivation……32

   4.2 Experiments…….33

   4.3 Results and Discussion……35

4.4 Conclusion……...42

5. **Modeling and Sensitivity Prediction..**…….…...44

5.1 Introduction and Motivation……44

5.2 Modeling……..44

5.3 Experiments…….52

5.4 Results and Discussion……53

5.5 Conclusion……...59

6. **Summary and Future Work**……...……..……..62

6.1 Summary…….…….62

6.2 Future Perspectives – Microfluidic optimization...…….…….……66

6.3 Silicon transistors, surface quality control, and pressure sensing……72

7. **Bibliography**……..…...76

8. **Appendix A**……...…89

9. **Appendix B**……...…93

10. **Appendix C**……...…98

List of Figures

Fig 1.1. Scheme of ELISA……...2

Fig 1.2. Structure of a typical thin film transistor……5

Fig 1.3. Traditional FET-based chemical sensor devices……7

Fig 1.4. Electrolyte-gated Transistors……..9

Fig 1.5. Side view schematic of FGT device with transfer curve measurements……..13

Fig 2.1. Alkylthiol SAM……16

Fig 2.2. Schematic of Aerosol Jet Printing……17

Fig 3.1. Example transfer curve……...……..……24

Fig 3.2. Example charge response……..……...25

Fig 3.3. Concentration dependence of charge signals……..…….28

Fig 3.4. Surface density dependence of charge signals……...……..29

Fig 4.1. Changes at the sensing surface…….33

Fig 4.2. Inverter and Transfer measurements……35

Fig 4.3. Capacitance sensing……..37

Fig 4.4. Charge sensing…….…….38

Fig 4.5. Comparison of capacitance and charge responses……40

Fig 5.1. Device/circuit structure and design……45

Fig 5.2. Inverter circuit simplified…….46

Fig 5.3. EGT and FGT responses……50

Fig 5.4. Gain comparison……...53

Fig 5.5. Signal subtraction (Difference curves)…….54

Fig 5.6. Charge and capacitance signal trends……55

Fig 5.7. Predicted signals……57

Fig 6.1. Microfluidic channel.……68

Fig 6.2. 5-channel design……70

Fig A.1. Acid and base Titrations…….……..…….……..89

Fig A.2. Example NRA measurement…….……..……90

Fig A.3. Titration curves for different concentrations……...……....91

Fig A.4. pK_a trends…….…...…….92

Fig B.1. Cyclic Voltammetry……..……...……93

Fig B.2. Gain vs load resistance……..…….……....….94

Fig B.3. Displacement current measurements…….……..…….95

Fig B.4. Theoretical difference curves……...97

List of Tables

Table 6.1. Detection times for new microfluidic designs……..69

Statement of the Author's Contribution

Portions of this dissertation were written in collaboration with Scott P. White (SPW), C. Daniel Frisbie (CDF) and Kevin D. Dorfman (KDD). Two chapters have appeared as articles in journals, with another in preparation for submission. I would like to point out the contributions of the different people involved here for the published work.

Chapter 3 was published as a letter: Thomas, M.S., White, S.P., Dorfman, K.D., Frisbie, C.D.; Interfacial Charge Contributions to Chemical Sensing by Electrolyte Gated Transistors with Floating Gates, Journal of Physical Chemistry Letters (2018), 9(6), 1335-1339. In this publication, we investigate the response of Floating Gate electrolyte-gated Transistor (FGT) devices to the localization of surface charge created by the deprotonation of acid-terminated self-assembled monolayers. I performed the experiments and data analysis for this publication. SPW was involved in the generation of ideas, discussion of results, and editing of the manuscript.

Chapter 4 was published as an article: Thomas, M.S., Dorfman, K.D., Frisbie, C.D.; Detection and Amplification of Capacitance and Charge-based responses by Floating Gate Electrolyte Gated Transistors, Flexible and Printed Electronics (2019), 4(4), 044001. In this paper, we demonstrate the detection of a capacitive input in the FGT device created by different lengths of alkylthiol monolayers. We further amplify the response with an inverter circuit and compare the results to charge-based inputs. I performed the experiments and data analysis for this paper.

Chapter 1. Introduction and Background

A common goal for distributed chemical sensor platforms is to provide fast, quantitative tests that are easy-to-use. One path towards this goal is through the use of printed electronics, which uses solution-based fabrication of electronically active films to create devices that can transduce binding events of specific target molecules with capture molecules. Often printed and organic transistor devices are sensitive to the sensing media, which may need to be harsh or reactive to effectively solvate the targets of interest. Complications that arise from the contact of the primary and secondary electrolyte, such as electronics degradation or solution contamination can be prevented by separation of the two compartments using a floating or extended gate arrangement. This contribution quantifies the effects of charge and capacitance on this novel device and models its response to obtain general design rules for floating gate transistor sensors.

1.1 Introduction to Bio/chemical Sensing

Detection of chemical or biologically relevant targets is a necessary step in food and environmental quality control, disease diagnosis and treatment, the monitoring and maintenance of public health as well as scientific research into these areas.[1] Rapidly increasing and aging populations and the demand for continuous monitoring of human health and the environment for applications such as personalized medicine has prompted research into sensing devices that can be implemented directly at the point of need,[2] to provide an initial screening for biomarkers,[3] pathogens,[4,5] allergens[6] or toxins.[7]

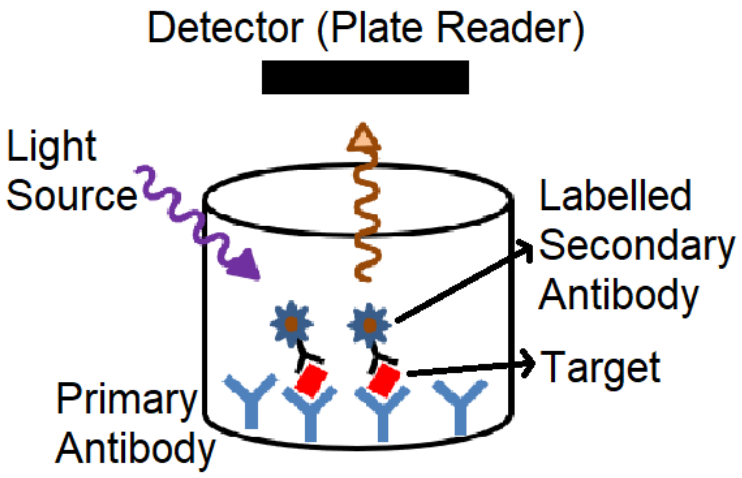

Fig 1.1. Scheme of ELISA. A cartoon depiction of the 'sandwich' portion of an ELISA is shown here. The target solution is exposed to an antibody containing well, followed by a secondary antibody binding, with rinses in between to remove unbound molecules.

Sophisticated lab-based tests are traditionally utilized to provide highly quantitative information about targets of interest, which include small molecules, proteins and cells for detection relevant to biological systems. The Enzyme-Linked Immuno-Sorbent Assay (ELISA) (depicted in Fig 1.1) and its variants[8] are the gold-standard general-purpose techniques used in hospitals and research labs for the quantification of numerous entities (pathogens,[4,9] proteins,[10] small molecule chemicals) found in the human body and the environment. Methods for detecting biological entities that are often specific to their targets include staining[11] and gel electrophoresis[12] for proteins, and cell culture[13] followed by microscopic or image-based methods[14] for bacteria or whole cells. An increasingly popular test for organisms is the PCR (Polymerase Chain Reaction) test, which amplifies the genetic material (DNA or RNA) in the sample, followed by optical quantification.[15–17]

The other most commonly utilized general purpose technique for chemical sensing is Mass Spectrometry (MS). In this method, the sample is ionized with an electron beam and accelerated to a detector with electric or magnetic fields. The mass to charge ratio of the constituent molecules or particle fragments is extracted by the detector and form distinct spectra which can identify the chemical character and masses of molecules present in the sample.[18] This is a highly quantitative and widely applied method that is often used along with a separation step such as liquid (LC-MS) or gas chromatography (GC-MS) and gel separation for protein targets.[19] An additional factor to consider in spectroscopic techniques is that all the entities present in the sample yield an output – detection of only certain targets must be obtained through additional steps or secondary data analysis. Both these techniques, serving as examples of lab-based general purpose detection methods, are ubiquitous and highly quantitative, but are often time-consuming (>2 hours for detection) due to either labeling, secondary binding or additional separation steps,[20,21] and require highly trained personnel to operate, putting them at a disadvantage for distributed applications.

In order to simplify, better analyze, and improve them, sensing or detection platforms in general are seen as consisting of two parts – a selective capture module, which enables specific binding to the target of interest, and a transducer or detector that converts the binding event to a readable signal. Transducers can be divided broadly into optical and electronic based on their mechanism of action. ELISAs, for example, rely on binding with specific labelled capture molecules (generally antibodies – hence the term immunoassay is often used to describe the ELISA and its variants), followed by optical transduction with equipment such as spectrophotometers (called plate readers for ELISAs).[22]

Electronic transducers have garnered attention over the last few decades due to their fast and direct electronic response, which can bypass the labeling step and generally bulkier optical transducer modules.[23] Indeed, the first use of the term biosensor came in reference to the Clark oxygen electrode in the 1960s[24] for the detection of the enzymatic oxidation of glucose using amperometric measurements of hydrogen peroxide reduction to oxygen. Since then, advances in materials and device fabrication have reduced the size and increased the ease of use for electrochemical glucose sensors, making them the most commercially successful chemical sensors to date.[25] Electrochemical methods are still the most commonly utilized techniques for electronic transduction due to well-characterized measurement techniques such as cyclic voltammetry, impedance spectroscopy, as well as simpler amperometric measurements for electroactive species.[7,26–29] Another promising transducer with a direct electronic response that can additionally provide in-built amplification is the transistor, which will be discussed in detail in the next section.

1.2 Transistors, EGTs and Transistor-based Sensing

Transistors are three terminal devices that consist of a semiconductor channel flanked by two conductive electrodes (called the source and the drain), with the third electrode, called the gate, coupled through a dielectric. The gate voltage can change the conductivity of the semiconductor by coupling the applied electric field through the dielectric.[30,31]

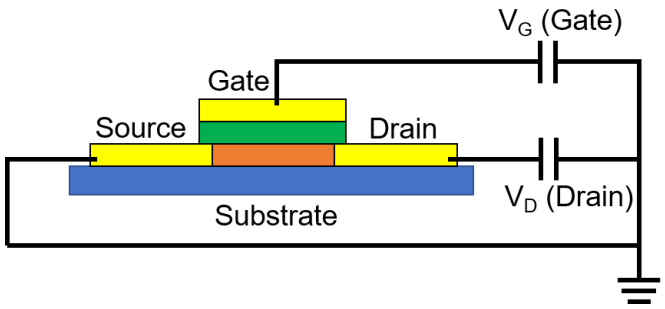

Fig 1.2. Structure of a typical thin film transistor. Yellow shows the gold electrodes, orange indicates the P3HT semiconductor, and green represents the dielectric. V_G refers to the gate voltage, V_D refers to the drain voltage. Small changes in V_G (depending on the values of V_D and V_G) can cause large changes in semiconductor conductivity and enable signal amplification.

A typical transistor structure is shown in Fig 1.2, with the gate on top of the semiconductor and dielectric, referred to as a 'top-gated' structure. Alternately, 'bottom-gated' structures place the dielectric and gate electrode below the semiconductor. Transistors are particularly attractive as transducers for sensors since small changes in the gate voltage can cause large changes in the conductivity of the semiconductor channel. This provides built-in amplification along with fast electronic transduction for small potentiometric changes caused by molecular binding events. Another advantage of transistor-based sensors are simple measurement techniques such as straightforward current or voltage measurements.

The typical measurements used to characterize transistor behavior are the transfer characteristics and output characteristics. In the former, the gate voltage is fixed, and the drain voltage is swept to increase the current until a plateau is reached for one particular gate voltage. In the latter, the drain voltage is fixed, and the gate voltage is swept from positive to negative voltages (for p-type devices). The current is measured at the drain

terminal and can be increased by several orders of magnitude as the device is switched from the off to the on state. Several important parameters govern the response of the device to these measurements. The mobility μ is the speed of charge carriers (electrons or holes) in the device per unit applied electric field and is an important metric of device performance. C_i is the specific capacitance (capacitance/area) of the semiconductor/dielectric interface. V_T refers to the threshold voltage of the device, which indicates the amount of gate voltage that needs to be applied to switch on the device. The value of V_T represents band bending and/or traps in the device that alter the available energy states for the charge carriers (holes or electrons). These states must be filled before the charge carriers can be drawn freely across the semiconductor channel, resulting in a minimum potential that must be applied to 'switch on' the device. V_T can be changed by the morphology of the semiconductor film, impurities at the semiconductor/dielectric interface, and the doping state of the semiconductor. The relationship between the current flowing through the semiconductor and the applied voltages can be derived using Ohm's law and the capacitive charge voltage relationship (Q = CV). The general equation governing the current, called the square law current equation, is

$$I_D = \frac{\mu C W}{L}\left[(V_G - V_T)V_D - \frac{{V_D}^2}{2}\right] \quad (1.1),$$

where W and L refer to the width and length of the semiconductor channel. This equation is valid for $V_G - V_T < 0$ (in case of a p-type device, as is the case in this work).

In the limit of $V_D << V_G - V_T$, the second term in Eq 1.1 can be ignored, and this limit is called the linear regime of operation (due to the linear relationship of the current with the drain voltage)

$$I_D = \frac{\mu C_i W}{L}(V_G - V_T)V_D \quad (1.2).$$

An important metric calculated for the device is the transconductance

$$\frac{dI_D}{dV_G} = \frac{\mu C_i W}{L} V_D \quad (1.3)$$

which measures the change in drain current obtained by changing V_G, a measure of how easily the device can be switched on.

When V_D is greater than V_G-V_T, or is of similar magnitude as V_G - V_T all the charges induced in the semiconductor are swept across the device by the drain voltage and the current is said to be 'saturated', and $V_D = V_G$-V_T can be substituted into Eq 1.1 to yield

$$I_D = \frac{\mu C W}{2L}(V_G - V_T)^2 \quad (1.4)$$

which is known as the saturation regime. The saturation regime yields a higher current (due to higher V_D) and is often chosen as the regime of operation for sensing purposes.

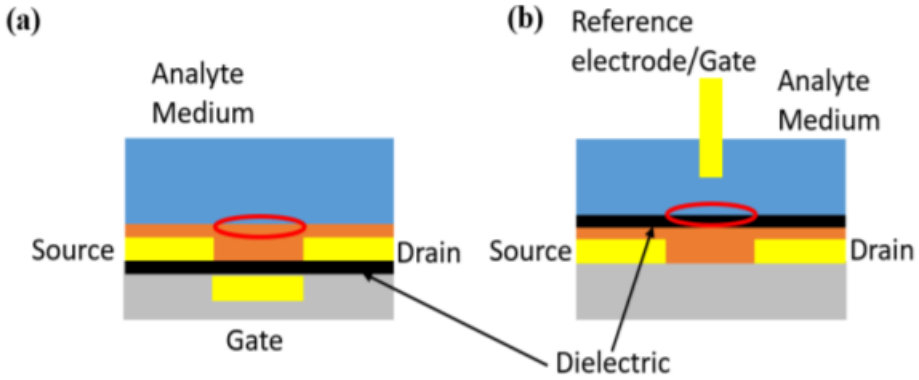

Fig 1.3. Traditional FET-based chemical sensor devices. (a) Bottom gated structure for FET-based sensors with the semiconductor in orange, dielectric in black, electrodes in yellow, and sensing medium in blue (b) Top-gated structure for a FET-sensor with a reference electrode used to apply gate voltages.

Transistors have been employed to detect numerous chemical and biochemical targets since the introduction of transistor-based sensors in the form of Ion Sensitive Field Effect Transistors (ISFETs) in 1970.[32] This device consists of a transistor with the dielectric in contact with an electrolyte solution. A reference electrode in the solution applies the gate voltage and the current is recorded at the drain terminal (Fig 1.3). The concentration of ions changes the electrochemical potential that gates the primary dielectric and hence changes the final potential felt by the semiconductor.[33] This structure can detect the concentration of ions in solution that can specifically bind to the dielectric surface. Since a simple oxygen plasma treatment can create a layer of -OH groups on traditional silicon dioxide dielectric layers, pH measurements became the most common application for this device.[34]

Numerous studies since then have shown FET-based devices with similar overall structures (Fig 1.3) to be effective transducers for molecular binding,[35–38] and specific names were even given to sensors for different classes of targets or capture agents such as Enzyme-FETs,[39] DNA-FETs,[40] Immuno-FETs,[41] Chem-FETs,[42] Cell-FETs,[43] and pH-FETs.[33] The most sensitive detection has been shown by FETs that maximize the effective area of the semiconductor, which doubles as the sensing surface. Silicon nanoribbons,[44] nanowires[45] and carbon nanotube-based sensors[46] are some examples of this class of FET sensors that provide extremely sensitive detection of single molecules. Complex and device-specific methods are often utilized for both the fabrication of the transistor and the attachment of capture agents to the semiconductor or dielectric surface.[47] While these are extremely sensitive, the proliferation and commercial application of many of these platforms can be limited by the complex and specific fabrication and surface chemistries

required to complete these devices.[48,49] Transistor-based sensors with simpler fabrication have hence been pursued as alternatives.

Solution-based methods such as printing were seen as alternatives to traditional fabrication methods with the development of organic semiconductors and printable inks. The first organic semiconductor-based devices were developed in the 1970s,[50,51] with molecules containing conjugated backbones that enabled delocalization of electrons. Suitable alkyl side chains can enhance dissolution of these molecules in organic solvents as well as their organization into ordered structures upon film formation, which can enhance charge transport.[52] The solubility of these semiconductors in organic solvents opened up many possibilities for solution-based fabrication of thin films which reduced the complexity and fabrication time needed to create transistor-based sensing devices, compared to traditional silicon-based technology. Techniques such as screen printing,[53] inkjet printing,[54,55] and aerosol jet printing[56] have been employed to create organic (and

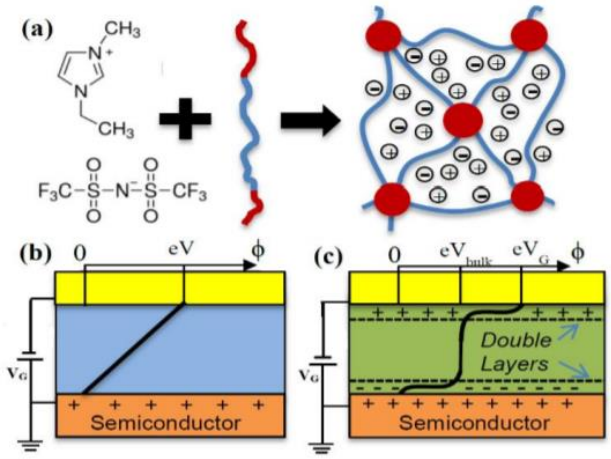

Fig 1.4. Electrolyte-gated Transistors. (a) An ionic liquid is gelled with an ABA block copolymer to form a microphase separated network termed an "ion-gel". (b) The potential drop through a conventional solid dielectric drops linearly through the film while (c) the potential drop through an electrolyte dielectric is concentrated at the interfaces due to the mobile ions.

inorganic) transistor-based devices. Many organic semiconductors, however, can show poorer charge carrier transport properties (mobility)[57] compared to inorganic materials with long range atomic order, which can result in a trade-off between device performance and fabrication speed/complexity.[58] Organic and printable materials are well suited to complement traditional silicon-based technologies for low power and/or large area applications such as sensors,[59] screens/displays with OLEDs,[60] solar cells,[61] or flexible RFID devices,[62] where the primary focus is not high speed dynamic response or the concentration of computing power into small structures. Chemical/biosensing is another example of such an application, where the rate limiting step is often mass transport of species to a surface, even when traditionally 'slower' transistors are used as transducers. Additionally, the area of the sensing surface often determines the size of the transistor channel unless the two are physically separated (as will be discussed in chapter 1.3), and making it as small as possible may not be desirable.

Apart from simpler fabrication methods, another aspect of improving the suitability of transistor-based sensors for portable applications is lowering the operating voltage to enable compatibility with compact (and possibly printed) battery power supplies. The operating gate voltage induces charge carriers in the semiconductor through the dielectric layer through capacitive charging. Required operating voltages can hence be reduced by increasing the capacitance of the dielectric layer. One option is to use 'high-k' dielectrics such as such as HfO_2 or Ta_2O_5, with the possible downside of current leakage. Replacing traditional solid dielectrics (such as SiO_2) with electrolytes can increase the capacitance to ~10 $\mu F/cm^2$, which represents a 10-fold increase in specific capacitance, even from high-k dielectrics (~100 nm thickness).[63,64] This increase is caused by the formation of electric

double layers by mobile ions at the interfaces of electrolyte compartments upon the application of an external voltage. The concentration of ions in a few nanometers thick layer creates very high thickness-independent interfacial capacitances.[65] This results in smaller voltages required to induce the same amount of charge in the semiconductor, which enables low voltage operation – a key advantage for portable applications. Another important implication is the possibility of side-gated devices, as the formation of double layers can occur even without physical alignment of the interfaces, as enabled by a bottom or top-gated structure.[66]

Many electrolytes have been utilized to gate transistors, including solid polymers with salts,[67] ionic liquids,[68] and composite materials.[69] Of these ionic liquids have been the most utilized for their wide electrochemical stability windows, negligible vapor pressure, and ease of processing into thin films using techniques such as printing, which makes them especially suitable for printed electronic sensors.[70] The ability of the electrolyte ions to permeate into the semiconductor creates two classes of electrolyte gated transistors. A lack of permeability results in EDLTs (Electric Double Layer Transistors), where the ions form a double layer at the semiconductor-dielectric interface.[71] ECTs (Electrochemical Transistors) refer to systems where the electrolyte ions permeate into the bulk of the semiconductor film.[63] This is associated with higher source-drain currents due to 3-dimensional doping of the semiconductor film, making them attractive for sensing applications. Electrolyte-gated Transistors (EGTs) have hence been utilized for sensing purposes by the attachment of capture molecules to the semiconductor[72] or the gate electrode[59] for specific quantification of chemical and biological targets. However, the performance of EGTs as sensors can be affected by the contact of the electrolyte

compartment and the sensing area, which can cause contamination of the sensing medium, and degradation of the semiconductor films, especially for organic semiconductors. Separation of these two electrolytes can be achieved by using an additional conducting separation element, which can address many of the aforementioned issues.

1.3 The FGT Platform

To overcome disadvantages associated with the contact of chemicals and the ion-gel, as well as complex and/or specific surface chemistries, the addition of an extra gate connecting the dielectric to the sensing surface called the floating gate is desirable in EGT-based sensors. This enables the separation of the transistor materials and the sensing medium and prevents the aforementioned contamination and degradation issues associated with the contact of the primary electrolyte dielectric and the sensing medium or other compounds needed for dissolution of targets or attachment of capture molecules. An additional advantage is the possibility of using simpler and well-established chemistries associated with metallic electrodes such as gold, instead of methods specific to the semiconductor or dielectric materials. Floating or 'extended-gate' FET-based devices have been utilized since 1983 for the detection of pH,[73] urea,[35,74,75] proteins,[37,76,77], DNA,[78] and cancer biomarkers.[79,80] The combination of floating gate and EGT (shown in Fig 1.5) was first reported in 2014 by White *et al*. at the University of Minnesota.[81] This device was utilized for the detection of single strand DNA from the shifts created in the transfer curve response of the EGT. Increasing concentrations of a specific sequence of DNA in the sensing medium caused increasing negative shifts in the response when it bound its complementary strand, which was immobilized at the sensing surface.[81]

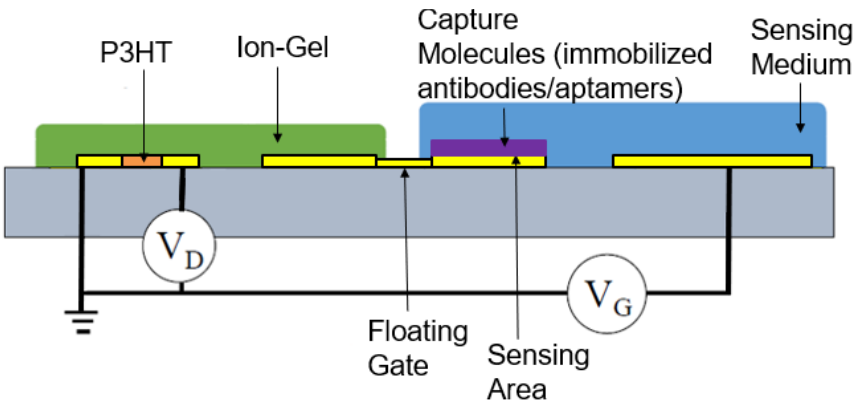

Fig 1.5. Side view schematic of the FGT device with transfer curve measurement circuit. The gate voltage is coupled from the control gate through the sensing medium (blue) to the floating gate, and then through the ion-gel (green) to the semiconductor (orange). Electronic connection with physical separation is achieved in this device structure, while also keeping the benefits of using the ion-gel dielectric.

After this first demonstration of the floating gate EGT's effectiveness, it was utilized for the detection of the toxin ricin in buffer solution and potable liquids such as milk and orange juice.[82] A novel aptamer developed previously was chosen to be the capture agent for its superior stability towards pH and temperature.[83,84] Another demonstration of the FGT's protein detection capabilities came with the detection of gliadin, a component of the food allergen gluten.[85] Multiple capture agents were utilized for the detection of gluten in a multiplexed fashion to determine the source of gluten in different types of grain. To understand the operating mechanism of the device, a study with ion-gel as both compartments was conducted with different interface areas and SAM molecule attachment, which determined that capacitive coupling and work function changes at the sensing surface contribute to changes in the device response.[86]

While these studies advanced the technological capabilities of the platform, fundamental questions remained regarding the sensing mechanism of the device. This thesis aims to study the response of the device towards two fundamental inputs, charge and capacitance, using self-assembled monolayers (SAMs) as a model system. The device response is further amplified and modeled to yield performance and sensitivity predictions that match with experimental results and thus provide guidelines for device design that improve user accessibility to these devices and put floating gate transistors on firmer footing as promising sensors for portable and distributed applications.

Chapter 2. Materials and Methods

An overview of the materials and experimental methods utilized in this work is provided here.

2.1 Materials

P-doped silicon wafers with a 300 nm silicon dioxide film were purchased from Silicon Valley microelectronics for all the studies in this thesis. Poly(3-hexyl-thiophene) or P3HT is the organic semiconductor tested in this work. It is a conjugated polymer with a thiophene backbone that enables delocalization of π-orbitals and hexyl sidechains that enable improved dissolution in organic solvents and crystallinity in the resulting films. P3HT deposited via spin coating or printing from solution creates semi-crystalline films with π-orbital stacking, which further enhances charge transport.[87] It is a well-studied organic semiconductor and has been demonstrated to provide up to 1.4 cm^2/Vs mobilities when utilized with ion-gel gate dielectrics.[88] Regio-regular P3HT (80 kg/mol) was purchased from Rieke metals for the experiments conducted for this thesis. The ion-gel gate dielectric consists of a triblock co-polymer poly(styrene-ethylacrylate-styrene) or SEAS, and the ionic liquid 1-ethyl-3-methyl-imidazolium bis(trifluoromethyl sulfonyl-imide) or EMI-TFSI. These constituents were mixed in a 1:9 ratio by mass to yield the ion-gel. The styrene end blocks are glassy and do not mix with the ionic liquid solvent.[89] This causes microphase separation and the styrene forms spherical nodes that serve as physical crosslinks connecting the ethylacrylate chains to form a network that spans the gel. The ion-gel was mixed with the solvent ethyl acetate in a 1:9 ratio by mass for printing.[64]

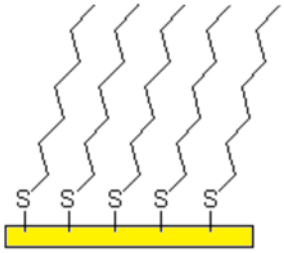

Fig 2.1. Alkylthiol SAM. An example of a C8-SH (octanethiol) self-assembled monolayer (SAM) on gold (yellow). SAMs can form ordered arrangements that can even be detected by XRD with characteristic tilt angles.

Self-assembled monolayers (SAMs) are monolayers created by molecules containing a reactive end group such as a thiol (S-H) – which spontaneously form coordinate bonds with metal surfaces at room temperature to yield an ordered layer.[90] The well-established and simple formation of SAMs has enabled their use in numerous sensing studies as the linkers between gold substrates and more complex molecules such as antibodies or other capture agents required for sensing purposes.[91] The SAM-forming molecules octanethiol, decanethiol, dodecanethiol, hexadecanethiol, and 11-mercaptoundecanoic acid (MUA), were procured from Sigma-Aldrich for use in the experiments conducted for this thesis.

The second compartment in the device is created with PDMS, in the form of a well or a microfluidic device. Poly(dimethylsiloxane) or PDMS is a versatile and commonly utilized material in the fabrication of microfluidic or lab-on-a-chip devices.[92] It consists of a liquid monomer and a crosslinker that can be mixed and heated to form a solid that can be cut by hand with blades or pierced with appropriately sized needles to form connecting

channels. The simple crosslinking allows complex and dense microchannels to be created from SU-8 molds on silicon wafers, which are in turn created by photolithography.[93]

2.2 Techniques

The gold electrodes and measurement pads needed to create FGT devices were deposited along with a chromium adhesive layer by E-beam evaporation after photolithography with a dark field mask. Lift-off processes removed the photoresist and yielded the final gold patterns.

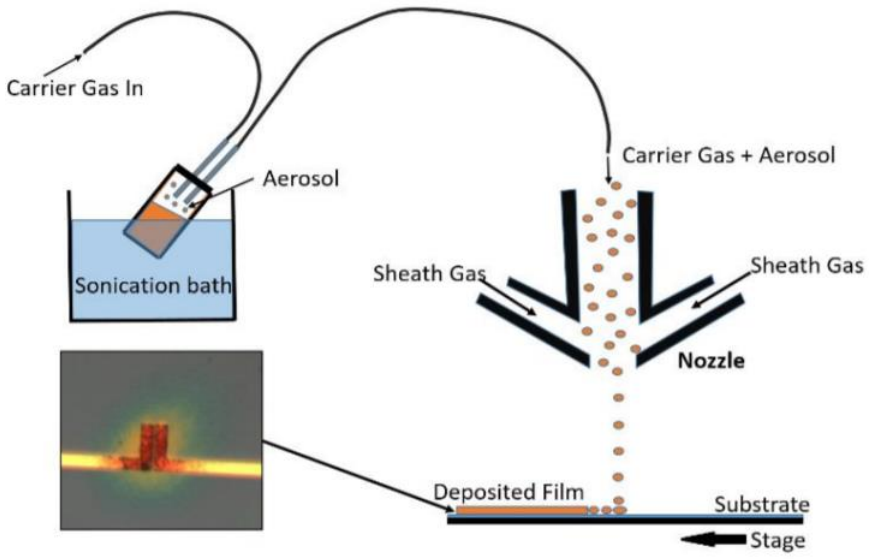

Fig 2.2. Schematic of Aerosol Jet Printing. The desired material is formulated into an ink (orange), which is sonicated to create an aerosol. Inert gases such as nitrogen carry the aerosol and deposit it onto a substrate, with a second gas stream called the sheath gas focusing the spray. The stage is heated to 60 ^{o}C for P3HT and ion-gel deposition, and an example P3HT film with gold source-drain electrodes and connecting vias is shown on the left.

EGTs were fabricated using Aerosol Jet Printing (AJP). The material to be deposited was dissolved in a suitable solvent and sonicated to produce an aerosol. Nitrogen

gas carried the aerosol through connecting tubes and sprayed it onto the substrate (which is heated to 60 ^{o}C) through a 150 μm nozzle while a second gas stream known as the sheath focused the stream of aerosol particles. The gas streams were kept close to 15 standard cubic centimeters per minute (sccm) and 55 sccm respectively but were adjusted to create a uniform and well-defined film (as seen under a microscope attached to the printer) during each printing session. The organic semiconductor P3HT and ion-gel dielectric films were created by this method to complete the EGT. AJP is an additive manufacturing technique, which implies that material is only deposited where it is needed.[56] Subtractive processes, on the other hand (such as spin coating), deposit the material on the entire substrate and remove the areas that are not needed, causing much higher material wastage and the need for extra removal steps. AJP is an extremely rapid and versatile prototyping method, which allows for the use of a wide range of ink viscosities to test the best operating conditions for the creation of thin film devices from a variety of materials. Complex patterns can be printed at speeds of up to several mm/s, depending on the material and design complexity. Printing methods are also compatible with roll-to-roll manufacturing, which promises even higher speeds and inexpensive fabrication of electronic devices[94] and is the focus of current work in several research groups.

Poly(dimethyl siloxane) or PDMS is a commonly utilized material that consists of siloxane (Si-O) backbone with methyl side chains which can be crosslinked to form a translucent material with a low glass transition temperature, and low change of elastic modulus with temperature, and low water incorporation.[95] This makes it suitable for creating fluid channels for sensor devices with aqueous targets. Commercial Sylgaard PDMS monomer and crosslinker were mixed in a 10:1 ratio and heated at 75 ^{o}C for 2 hours

to enable crosslinking. Devices with channels for fluid flow (to selectively expose smaller sensing areas which cannot be isolated by hand-cut wells) were created from SU-8 molds on silicon wafers. Individual wells were cut by hand according to the sizes required by the experiments to encompass both the sensing area and the control gate. The fluid channels and wells were reversibly bonded to the silicon wafers and removed after their use is complete.

Surface analysis to determine the density of self-assembled monolayers (which can be created using PDMS wells) on gold was carried out with Nuclear Reaction Analysis (NRA), a variant of Rutherford Backscattering Spectrometry (RBS) is utilized to obtain the monolayer surface coverage. This experiment involves bombarding the surface with a high energy (4.266 MeV) alpha particle (He^{2+}) beam and recording the energy of the backscattered alpha particles. The particles excite carbon-12 nuclei in the sample to an intermediate state, which decays immediately to yield lower energy alpha particles (1.019 MeV) and the original carbon nuclei.[96,97] It has been found that (energetically) these collisions can be treated as elastic, similar to RBS, and a count of the number of scattered alpha particles enables a count of the number of carbon atoms present at the surface.[97] This carbon count can then be utilized to determine the coverage of the monolayers.[97]

Solutions of different pH (to be utilized as the aqueous secondary electrolyte) were created with KCl (as the electrolyte), with HCl or KOH used for pH adjustment. An optical Horiba handheld pH-meter was utilized to confirm the pH of the solutions before final use. Study specific details are stated in the relevant chapters. The testing of devices is carried out using Keithley source-measure units (SMUs) to sweep gate voltages (Keithley 2400),

and measure current (Keithley 2611B) and voltage (Keithley 2612) for transfer curves and inverter curves respectively. Step-by-step details can be found in Appendix C.

Chapter 3. Role of Interfacial Charge in Chemical Sensing*

3.1 Introduction and Motivation

The FGT device shows promise as a portable, label-free multiplexable device that overcomes many disadvantages of transistor-based sensor designs. However, the generalizability of this platform is hindered by a lack of knowledge about its sensing mechanism, which would allow for optimal design of the sensing surface as well as screening of targets and enhancement of the signal based on mechanistic optimization. To obtain possible sensing mechanisms, we examine the previously detected targets, past work on other transistor-based sensors, and a circuit analysis of the device. Previous work using the FGT platform has detected single strand DNA,[81] ricin,[82] and gluten[85] – all charged molecules with a pK_a lower than the pH of the aqueous buffer used as a sensing media. The FGT platform, as well as other transistor-based sensors, show a 'shift' in the response of the device upon binding of target molecules. This implies a change in the V_T of the transistor, which in case of traditional transistor-based sensor design, is thought to be from a direct doping of the semiconductor channel by the charge on the molecule which causes a change in the effective V_T of the device.[45] Analysis of the FGT circuit under quasi-static measurement conditions (treating each of the 4 interfaces as purely capacitive) to obtain a relationship between the applied voltage V_G and the voltage at the floating gate, indicates that capacitive changes at the FG2-aqueous surface (changes in C_{FG2}) can also cause

* This chapter is reprinted (adapted) with permission from Thomas, M.S., White, S.P., Dorfman, K.D., Frisbie, C.D.; Interfacial Charge Contributions to Chemical Sensing by Electrolyte Gated Transistors with Floating Gates, Journal of Physical Chemistry Letters (2018), 9(6), 1335-1339. Copyright 2018 American Chemical Society.

changes in the device response. Previous work with OFET-based sensors has also suggested that capacitance changes could be responsible for the detection of targets, even charged molecules.[98]

In this chapter, we isolate the effect of charge and analyze it quantitatively, with a simple and controlled experiment that uses self-assembled monolayers (SAMs) of 11-mercaptoundecanoic acid (MUA) exposed to buffers of different pH to generate surface charge at FG2. The choice of this molecule is determined by both the presence of an acid group (sensitive to solution pH) and a thiol group (which enables binding to the gold FG2 surface) and the length of its carbon chain. Previous work on SAMs has shown that the capacitance of SAMs monolayer interfaces is a series capacitance of the carbon chain and the head group. Upon deprotonation, the head group capacitance increases, but depending on the carbon chain, the total monolayer capacitance can remain constant.[99] As the carbon chain increases beyond 10 carbon atoms, it has been shown that the chain capacitance is low enough that the change in head group capacitance during deprotonation does not significantly affect the monolayer capacitance.[100] This results in a pH independent interfacial capacitance for 11-MUA, which allows us to isolate the effect of increasing the surface charge density upon changing the pH of the aqueous electrolyte on the device response.[99] For a quantitative comparison, we utilize a sensitive nuclear reaction analysis (NRA) measurement (a variant of RBS – Rutherford Backscattering Spectrometry) to determine the number of MUA molecules at the surface and hence the corresponding charge density.[97] A Gouy-Chapman treatment of the electric double layer provides a well-known relationship between the charge density at the surface and the potential created by

it, which is then compared with the FGT response, in the first quantitative examination of the charge-based response of floating gate transistor sensors in the literature.

3.2 Experiments

The EGT was fabricated by photolithographic processes followed by printing, as described in chapter 2.2. A PDMS well was reversibly bonded to the device encompassing the FG2 surface. The well was filled with a 1 mM solution of MUA in ethanol and left to functionalize for 4 hours, with the well replenished every 10 minutes to prevent the solution from drying. The solution was removed from the well after 4 hours and the well was debonded manually from the wafer. Another well is attached to the wafer that encompasses the sensing area and the control gate. The well was filled with different pH solutions and transfer curve measurements are made for each solution. The well was rinsed with DI water between the addition of each new buffer.

The buffers were prepared with KCl as an electrolyte, and KOH and HCl used for pH modification. A handheld Horiba pH meter was used to confirm the pH of the buffers before measurements. The measurements were conducted with a Keithley 2611B source-measure unit for applying the drain voltage and measuring the current, and a Keithley 2400 source-measure unit utilized for applying the gate voltage.

3.3 Results and Discussion

To analyze the response of the FGT device, it is worth examining the response of a typical EGT first. The most common measurement is a transfer curve, as described in chapter 1.2.

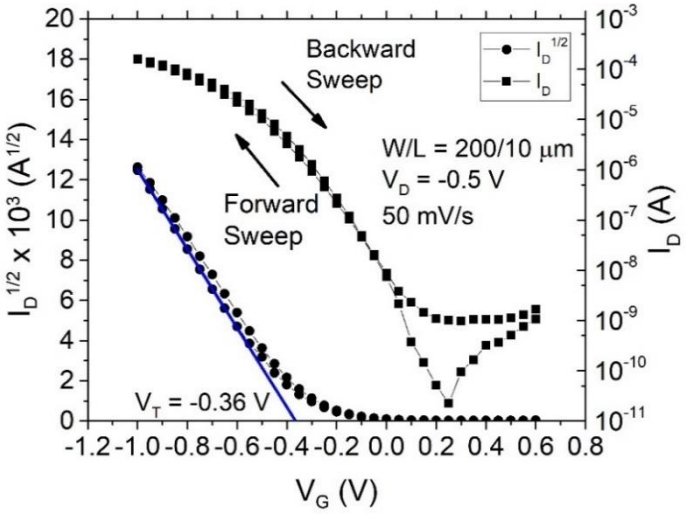

Fig 3.1. Example Transfer Curve.[101] An example of a transfer curve measurement with the channel dimensions utilized in this study. The right y-axis shows the drain current (I_D) as a function of gate voltage (V_G). The forward and reverse sweeps are measured with 50 mV/s. The on/off ratio is found to be 10^5 within a 1 V range. The left y-axis shows the square root of drain current ($I_D^{1/2}$) plotted vs V_G. A linear fit yields a threshold voltage V_T of -0.36 V, and a mobility of 0.8 cm^2/Vs. Reprinted (adapted) with permission from Thomas, M.S., White, S.P., Dorfman, K.D., Frisbie, C.D.; Interfacial Charge Contributions to Chemical Sensing by Electrolyte Gated Transistors with Floating Gates, Journal of Physical Chemistry Letters (2018), 9(6), 1335-1339. Copyright 2018 American Chemical Society.

An example EGT transfer curve measurement is shown in Fig 3.1. The source terminal is grounded, while the drain terminal is kept at -0.5 V (V_D) and the gate voltage (V_G) is swept between 0.8 V to -1 V. The off state, seen at positive voltages here, results in low drain currents of 0.1-1 nA, while the on state yields currents as high as 100 μA. For the example shown in Fig 3.1, I_D is seen to increase from 1 nA to 200 μA in the span of 1 V, which exemplifies the low voltage operation characteristics of EGT devices. The on/off current ratio is found to be more than 10^5. The value of V_D and V_G corresponds to the saturation regime operation (as described in chapter 1.2), and the saturation current

equation can be used to extract important device parameters. The square root of both sides of Eq 1.2 yields

$$I_D{}^{1/2} = \left(\frac{\mu C_i W}{2L}\right)^{1/2}(V_G - V_T) \quad (3.1),$$

where μ is the device mobility, C_i is the semiconductor/dielectric interfacial capacitance, W and L are the channel width and length respectively, and V_T is the threshold voltage of the device. A linear fit between $I_D{}^{1/2}$ and V_G is used to obtain μ and V_T, knowing the device dimensions and dielectric interfacial capacitance. The mobility calculated for 35 EGT devices in this study is 0.7 ± 0.2 cm^2/Vs, and the threshold voltage is -0.3 ± 0.2 V (mean and standard deviation is reported here). V_T shifts are utilized to assess the changes in device response caused by the accumulation of surface charge during MUA deprotonation.

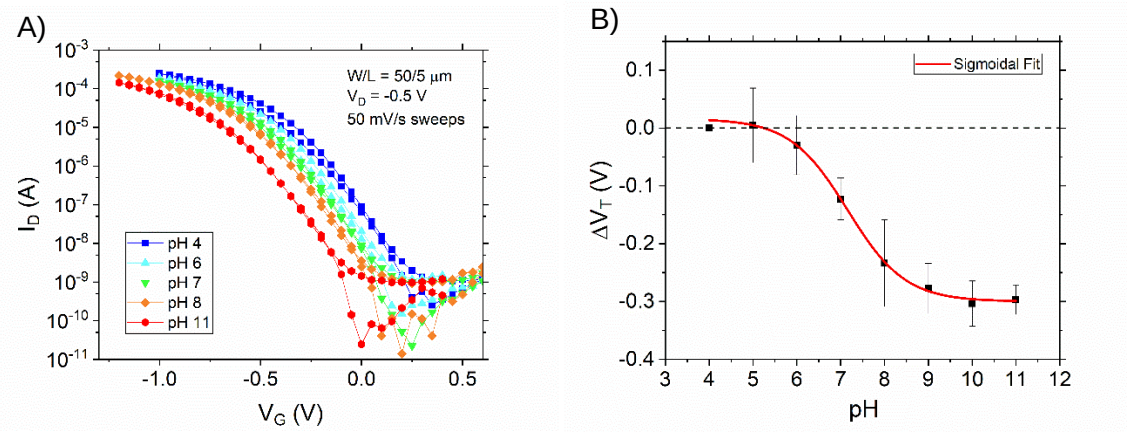

Fig 3.2. Example Charge Response.[101] (A) Transfer curves for a MUA-functionalized FGT device exposed to increasing values of pH. The curves switch on at more negative voltages as pH is increased. (B) The V_T shifts calculated with pH = 4 as reference are plotted vs pH. A sigmoidal fit yields $\Delta V_{T,max}$ ~ 300 mV and (inflection point) pK_a = 7.2. The error bars represent one standard deviation for five devices tested. Reprinted (adapted) with permission from Thomas, M.S., White, S.P., Dorfman, K.D., Frisbie, C.D.; Interfacial Charge Contributions to Chemical Sensing by Electrolyte Gated Transistors with Floating Gates, Journal of Physical Chemistry Letters (2018), 9(6), 1335-1339. Copyright 2018 American Chemical Society.

We exposed MUA functionalized FGT devices to pH 4 - 10, and recorded transfer curves at each pH value. An example device response is shown in Fig 3.2a, with increasing pH values shown in cold to hot colors (blue to red). The transfer curves are shifted negatively as pH is increased (and excess charge is localized at the sensing area), while the shape of the curves remains similar. This implies an excess potential that must be applied to the same device to switch it on. This change in the V_T (or switch-on voltage) is plotted against the pH in Fig 3.2b, and each point represents the average and standard deviation of the shift of 5 separate FGT devices. The data follows a sigmoidal curve characteristic of an acid/base titration with plateaus at low and high pH values of 0 and 300 mV respectively. A sigmoidal fit yields an inflection point of 7.2, typically associated with the pK_a for a traditional acid/base titration. This value is similar to the pK_a for MUA monolayers reported in literature, as measured by techniques such as surface plasmon resonance (7.2),[102] contact angle (7.3)[103] and electrochemical titration (7.2).[104] The titration curves for another acid and a base are shown in Fig A.1, and the extracted $pK_{1/2}$ values also match previously reported literature values.[105] Our goal is to relate the surface charge density to the potential response and the density of the monolayer is a crucial piece of information required for this task. A surface density of 3.2 mol/nm^2 is obtained using NRA measurements for monolayers assembled with the same functionalization protocol as the FGT sensing experiments. An example NRA spectrum is shown in Fig A.2. The surface density is found to be close to previous values for SAMs on gold, using backscattered alpha particles to extract a carbon count for the surface.[96,97]

The two plateaus at either end of the sigmoidal curve in Fig 3.2b represent states at which the monolayer charge is not significantly affected by changing the pH (for pH values

far enough from the pK_a), i.e., negligibly charged or fully charged. The difference between these two plateaus is hence considered to be the potential generated upon complete charging of the monolayer. The surface charge density at complete ionization can be calculated by multiplying the molecular density with the charge of a single electron, as each molecule has one acid group that can be deprotonated. This charge density can be related to the potential through a Guoy-Chapman treatment of the electric double layer at the FG2-aqueous interface. The solution of Poisson's equation for a metal-electrolyte interface yields the following relationship between the excess potential at the interface (compared to the bulk electrolyte) and the interfacial charge density:[65]

$$\phi = \frac{2kT}{e}\sinh^{-1}\left(\frac{\sigma}{\sqrt{8\varepsilon\varepsilon_0 kTN_A C_{ions}}}\right) \quad (3.2).$$

This is also known as Grahame's equation. Here, ϕ is the potential at the interface, σ is the surface charge density, e is the electronic charge, ε is the dielectric constant of the medium (water), ε_0 is the permittivity of free space, k is Boltzmann's constant, T is the temperature, N_A is Avogadro's constant, and C_{ions} is the concentration of ions in the solution bulk. Using the values of the aforementioned physical constants, the surface charge density, the temperature and the electrolyte concentration, the excess potential is found to be 290 mV, close to the 310 mV shift obtained from the transfer characteristics. This indicates that the transistor is a sensitive transducer for charge-based signals and that the shifts can be approximated by Grahame's equation, derived from well-established Guoy-Chapman double layer theory.

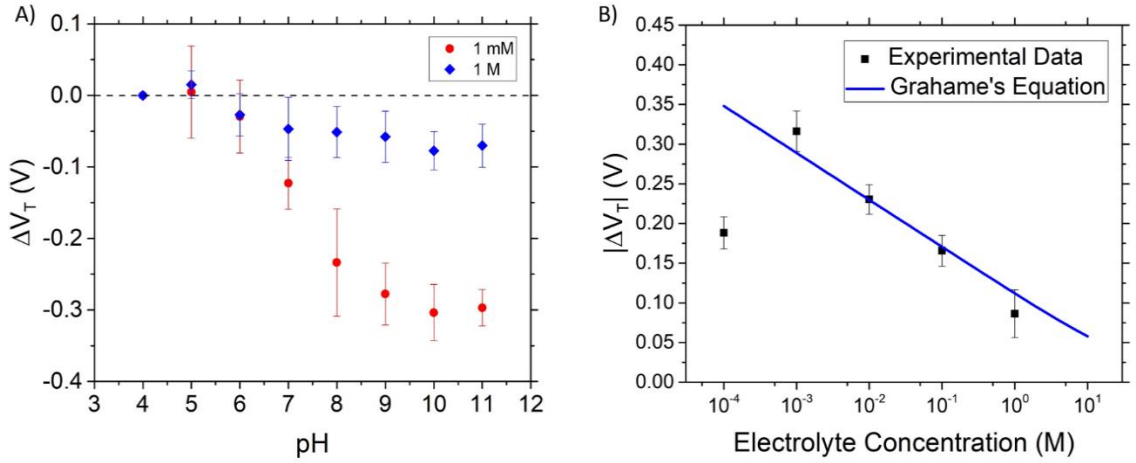

Fig 3.3. Concentration dependence of charge signals.[101] (A) 1 mM and 1 M titration curves. Signal (shift) is suppressed with increasing electrolyte concentration. (B) Maximum V_T shifts, calculated from a sigmoidal fit to V_T vs pH curves, are plotted against concentration, along with the Grahame's equation. Electrolyte concentrations of 1 mM and higher are close to the theoretical prediction, with a difference in slope. Error bars represent one standard deviation for measurements on 5 separate devices. Reprinted (adapted) with permission from Thomas, M.S., White, S.P., Dorfman, K.D., Frisbie, C.D.; Interfacial Charge Contributions to Chemical Sensing by Electrolyte Gated Transistors with Floating Gates, Journal of Physical Chemistry Letters (2018), 9(6), 1335-1339. Copyright 2018 American Chemical Society.

To further validate Grahame's equation as a predictor for the FGT response, we examine the effect of two important variables that affect the device response – the electrolyte concentration and the density of ionizable molecules at the surface. We increased the electrolyte concentration from 0.1 mM to 1 M and repeated the pH titration experiments for each value. Titration curves for 1 mM (the original experiment) and 1 M are shown in Fig 3.3a, with the remaining curves shown in Fig A.3. It can be seen that the higher concentration dampens the response of the device, which is consistent with charge screening of the deprotonated monolayer, which reduces the excess potential created by it. This also changes the pK_a value for the monolayer, and the obtained trends are shown in Fig A.4 in appendix A. Fig 3.3b shows the experimentally calculated total shifts (difference

between the plateaus) in black, and the prediction of Grahame's equation in blue. The prediction matches experiments closely from 1 mM to 1 M electrolyte concentrations, with a moderate difference in the slope – the experimental slope is -75 mV/decade, while the predicted slope is -59 mV/decade. This is attributed to the effects of ion-ion interactions, which are not accounted for by traditional double-layer theories, and could also be caused by electric field driven desorption, or dimerization of MUA molecules due to hydrogen bonding.[106] The experimental measurement at 0.1 mM deviates from the predicted value, and this is believed to be the result of inadequate surface concentration of ions needed to completely deprotonate the monolayer at low bulk electrolyte concentrations.

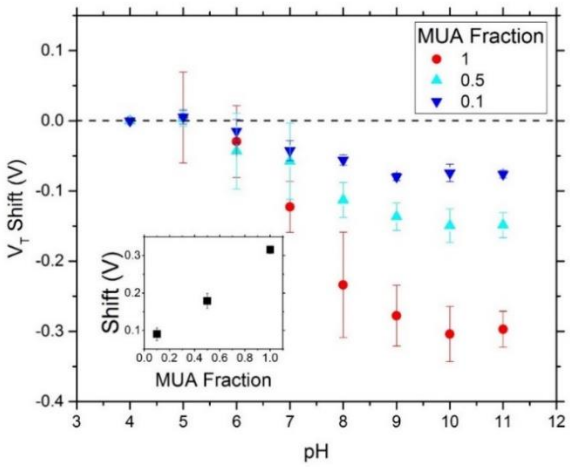

Fig 3.4. Surface Density Dependence of Charge Signals.[101] Titration curves with different MUA/Octanethiol fractions are shown here. Red shows 100% MUA, light blue shows 50%/50% MUA/Octanethiol, and dark blue 10%/90% MUA/Octanethiol. The inset shows the maximum shifts vs the MUA fraction and confirms the increasing trend of signals with MUA fraction and hence surface charge density (at maximum ionization). Error bars represent one standard deviation for 5 separate devices. Reprinted (adapted) with permission from Thomas, M.S., White, S.P., Dorfman, K.D., Frisbie, C.D.; Interfacial Charge Contributions to Chemical Sensing by Electrolyte Gated Transistors with Floating Gates, Journal of Physical Chemistry Letters (2018), 9(6), 1335-1339. Copyright 2018 American Chemical Society.

The second important variable that is changed is the surface charge density. We prepared mixed monolayers of MUA and octanethiol for this experiment. This consists of mixing different molar ratios of MUA and octanethiol with ethanol (with the same total concentration of 1 mM) and functionalizing the sensing area with these solutions for 4 hours. The result is a mixed monolayer of MUA and octanethiol.[107–109] The higher the fraction of MUA in the solution, the more MUA molecules are present in the final monolayer.[100] Octanethiol does not have any ionizable group, and hence does not contribute to the charge density when the solution pH is increased. This provides a simple method to control the number of MUA molecules, and hence the number of acid groups at the surface. Titration curves for MUA fractions of 0.1, 0.5 and 1 (the original experiment) are presented in Fig 3.4, with the electrolyte concentration fixed at 1 mM. The FGT response is diminished as the fraction of MUA is reduced, which is reducing the surface charge density. The inset provides a plot of the maximum shift against the MUA fraction and this shows the positive trend obtained by increasing the density of pH-responsive molecules at the surface.

3.4 Conclusion

The FGT device has been utilized for the detection of proteins and DNA in liquids, but the mechanistic understanding of its sensing capabilities was lacking, which hindered the screening of possible targets and further optimization of the platform. In this study, 11-mercaptoundecanoic acid (MUA) monolayers were bound to the surface of the sensing area, and deprotonated by exposure to solutions of increasing pH, to examine the effect of surface charge density on the device response. Transfer curves measured for each pH value

show that increasing the pH, and hence the charge density, produces shifts in the response, with the device switching on at progressively more negative voltages. The shifts plotted against the pH of the solution yield titration curves similar to acid/base reactions, with the calculated pK_a close to previously reported values. A surface analysis with NRA experiments shows a density of 3.2 MUA molecules/nm^2, and the maximum shift is predicted quite closely by Grahame's equation, a product of Gouy-Chapman electric double layer theory. Further validation of this theory is provided by changing the electrolyte concentration and repeating the experimental measurements. The transistor response is lowered due to increased screening of charges at higher concentrations. Grahame's equation is found to predict the transfer curve shifts well from electrolyte concentrations of 1 mM to 1 M, with a small difference in the predicted slope. In separate experiments, mixed monolayers of MUA and octanethiol are utilized to decrease the number of ionizable molecules in the monolayer, and hence decrease the surface charge density. This causes the maximum shift to decrease as the surface charge density at maximum ionization is lowered due to the incorporation of octanethiol (a molecule with no ionizable group) at the surface.

This work demonstrates the first quantitative sensing and theoretical comparison of charge-based inputs using a floating gate transistor platform and puts floating gate transistor devices on a firmer footing for chemical detection in the context of charge-based sensing, which is an important mechanism for the detection of biologically relevant targets in aqueous media.

Chapter 4. Capacitance Detection and Signal Amplification*

4.1 Introduction and Motivation

A significant push for chemical sensing in recent years has come from the need to continuously monitor chemicals associated with the human body, to extend functionalities associated with wearable electronics. This requires the fast and quantitative detection of hormones, food components and even small molecule drugs in fluids such as sweat, urine or blood.[59,110–112] A challenge in this regard for transistor-based sensors is the lack of charge on many of these targets at pH ~7, as well as charge screening in bodily fluids with high ionic strengths. One common solution is to detect changes in double layer capacitance upon the binding of these molecules to different targets with methods such as electrochemical impedance spectroscopy (EIS). EGT-based devices, however, are often not suitable for dynamic measurement techniques such as EIS. This is due to the lower mobility of the ions that comprise the ion-gel gate dielectric, that can cause artifacts such as voltage spikes and lagging responses as the ions are not able to respond fast enough to high frequencies, and the performance of EGTs begins to lag between 1-10 kHz.[113] Recently, artifact-free dynamic EGT performance has been demonstrated for frequencies up to 1 MHz. However, this method adds several more steps and complexity to the device fabrication, which can negate one of the main advantages of EGT-based devices for sensing – simple and fast fabrication.[114]

* This chapter is based on Thomas, M.S., Dorfman, K.D., Frisbie, C.D.; Detection and Amplification of Capacitance and Charge-based responses by Floating Gate Electrolyte Gated Transistors, Flexible and Printed Electronics (2019), 4(4), 044001, first published on November 1st, 2019. DOI: https://doi.org/10.1088/2058-8585/ab4dcf.

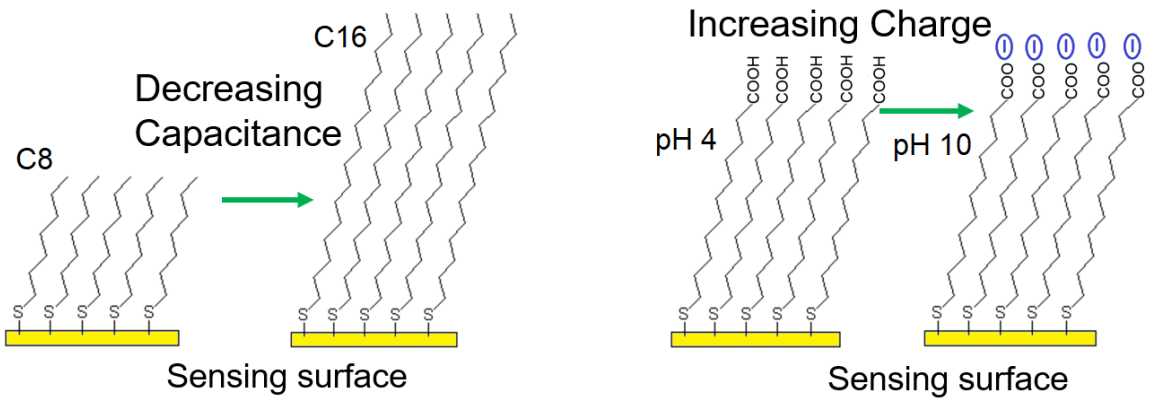

Fig 4.1. Changes at the sensing surface.[115] C8 to C16 alkylthiol monolayers are bound to FG2 (sensing area) to decrease the capacitance. MUA monolayers are bound to FG2 and exposed to pH 4 and pH 10 to generate surface charge to compare with the response to the capacitive inputs.

While the trade-off between fabrication complexity and high frequency operation for EGT-based sensing must be considered separately for each application, the detection of capacitance in a manner that avoids dynamic measurements is highly desirable and undemonstrated in the literature so far for floating gate devices.

In this study, we systematically change the capacitance of the FG2-aqueous interface with alkyl thiol self-assembled monolayers and amplify the responses with a simple inverter circuit. We compare these responses to that of charge-based inputs with MUA monolayers exposed to different pH values and identify distinct signal characteristics that can be utilized to distinguish between the two responses (Fig 4.1).

4.2 Experiments

EGT devices were fabricated on Si/SiO_2 wafers as detailed in chapter 2. Ethanolic solutions of C8-, C10-, C12-, and C16-thiols were exposed to the sensing area (FG2) for 4

hours using a PDMS well. The PDMS well was removed and replaced with another one that encompassed both the sensing area and the control gate for measurements. This well was filled with an aqueous 10 mM KCl solution as an electrolyte. Transfer curves were measured with Keithley SMUs applying and measuring voltage as described in Chapter 3, controlled by a LabView code. Inverter curves were measured as follows – Keithley 2400 applying gate voltages, Keithley 2611B applying the supply voltage, Keithley 2612 measuring the output voltage. For comparison with charge-based measurements, a similar device fabrication and functionalization protocol was followed, but with MUA SAMs. The measurement was completed with pH 4 to pH 10 solutions, that were prepared with 10 mM KCl as electrolyte and HCl or KOH added to change the pH appropriately. The pH of the aqueous secondary electrolyte solutions was checked with a commercial handheld pH meter before use, similar to chapter 3.

Cyclic Voltammetry was conducted to obtain the capacitance of the alkylthiol monolayers independently for sensitivity calculation. The measurements are shown in Fig B.1 in appendix B. A commercial Ag/AgCl reference electrode, Pt counter electrode, and a gold working electrode on Si/SiO_2 wafer was utilized for the measurement, and a potentiostat applied and measured the voltage and current respectively. Monolayers prepared using the same protocol as that for FGT sensing area functionalization were tested at different sweep rates and their specific capacitance was calculated from the resulting I-V curves.

4.3 Results and Discussion

The first part of the discussion focuses on the understanding of the inverter circuit response and its relationship to the transfer characteristics of the device.

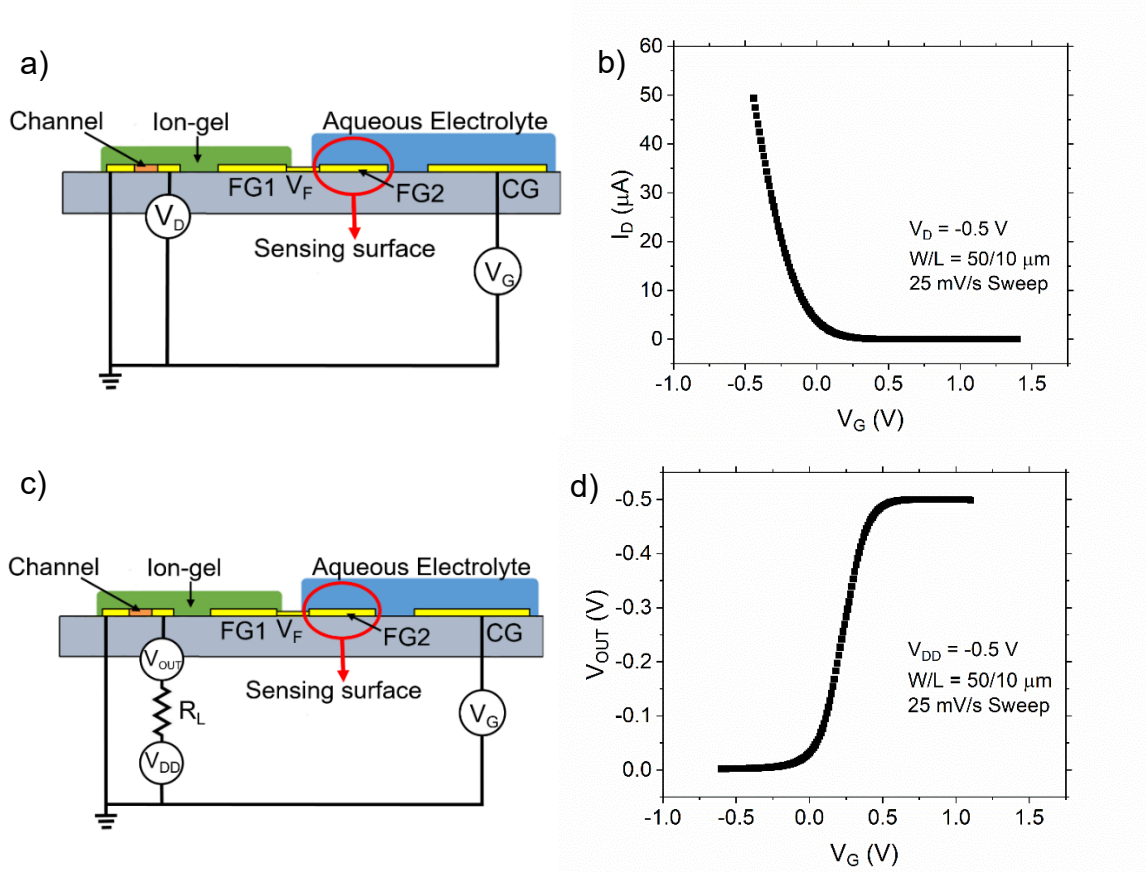

Fig 4.2. Inverter and Transfer Measurements.[115] (a) FGT device diagram with the transfer (I_D-V_G) curve circuit. V_G is coupled through the aqueous electrolyte to the floating gate, and further through the ion-gel to the channel, while V_D is applied across the source-drain terminals. The channel material (orange) is P3HT, while green represents the ion-gel. (b) An example transfer (I_D-V_G) curve for a FGT. W and L are the width and length of the semiconductor channel. (c) Schematic of a FGT-based, resistor-loaded inverter. V_G is applied at CG, supply voltage (V_{DD}) is applied across both FGT and the load resistor, and V_{OUT} is measured between the channel and the load resistor (R_L). (d) A typical inverter output curve. This figure is taken from Thomas, M.S., Dorfman, K.D., Frisbie, C.D.; Detection and Amplification of Capacitance and Charge-based responses by Floating Gate Electrolyte Gated Transistors, Flexible and Printed Electronics (2019), 4(4), 044001, first published on November 1st, 2019. DOI: https://doi.org/10.1088/2058-8585/ab4dcf. © IOP Publishing. Reproduced with permission. All rights reserved.

Fig 4.2a and Fig 4.2b shows the circuit and transfer response of an FGT and Fig 4.2b and Fig 4.2d shows the corresponding inverter circuit and response for the same device with a 1 MΩ load resistor. The inverter works by adding a load resistor in series with the transistor device and measuring the voltage between these two elements instead of the current at the drain terminal.[66,116,117] The output voltage moves between the two fixed values at either end of the series circuit – the ground (0 V) and the supply voltage V_{DD}, kept at -0.5 V here. The transition between the two voltages is responsible for the amplification provided by the device.

When a reference and sample inverter are subtracted, the transition segments yield a signal peak (similar to the subtraction of two sigmoids), which is larger than the shift between the two curves. The signal peak (for a lateral shift) is amplified by the device Gain (defined as $-dV_{OUT}/dV_G$), which is the negative slope of the aforementioned transition. It follows that a larger value of gain provides better amplification. Another advantage of the inverter curve is that it provides fixed reference points (ground and V_{DD}) to compare inverter curves between two different devices. EGT transfer curves can have currents differ by up to an order of magnitude between two devices measured with the same voltage range (due to differences in V_T), as evidenced by on/off current ratios ranging between 10^4-10^6 between printed devices with the same channel dimensions and materials.[81,88] This makes a simple subtraction-based signal for transfer curves hard to compare for separate devices.

The first experiment compares a C12-monolayer functionalized device to a control device with no monolayer. The sensing area of the device was functionalized with a C12 monolayer and an inverter curve is measured with V_G applied at CG and directly at FG2.

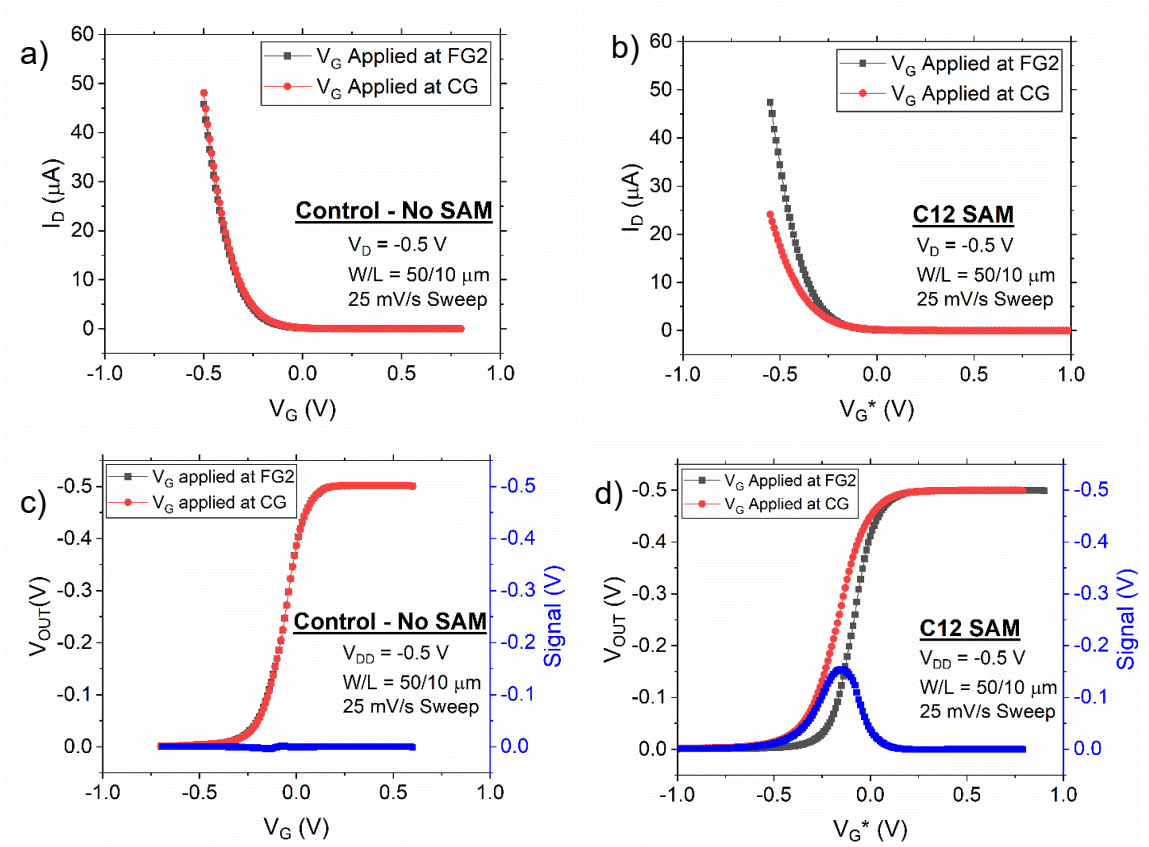

Fig 4.3. **Capacitance sensing.**[115] (a) Transfer curves for a control device with no SAM, with V_G applied at either CG or FG2. (b) I_D-V_G for a sample device with a C_{12}-SH SAM on FG2. The red curve is shifted so that its I_D crosses 1 μA at the same V_G as the black curve. The x-axis is consequently labeled V_G*. The slope of the red trace is clearly lower than the black trace. (c) Inverter measurements for the control device with no SAM. The subtracted signal between the two curves is shown in blue, which refers to the right-hand y-axis. Because the red and black curves overlap, the difference signal in blue is negligible. (d) The inverter curve for the sample device with a C_{12}-SH SAM. The red curve measured at CG is shifted so that the V_G at which V_{OUT} crosses -0.49 V is the same for both curves, hence again the x-axis is labeled V_G*. The gain (max slope) of this curve is reduced due to the presence of the SAM, which reduces the capacitive coupling. The blue difference signal thus exhibits a pronounced peak. This figure is taken from Thomas, M.S., Dorfman, K.D., Frisbie, C.D.; Detection and Amplification of Capacitance and Charge-based responses by Floating Gate Electrolyte Gated Transistors, Flexible and Printed Electronics (2019), 4(4), 044001, first published on November 1st, 2019. DOI: https://doi.org/10.1088/2058-8585/ab4dcf.

The two measurements provide a comparison of the circuit that includes the FG2 surface and the transistor alone. For the negative control device in Fig 4.3a, the two measurements

are nearly identical, which affirms the lack of potential drop across the FG2 circuit when it is included in the circuit.

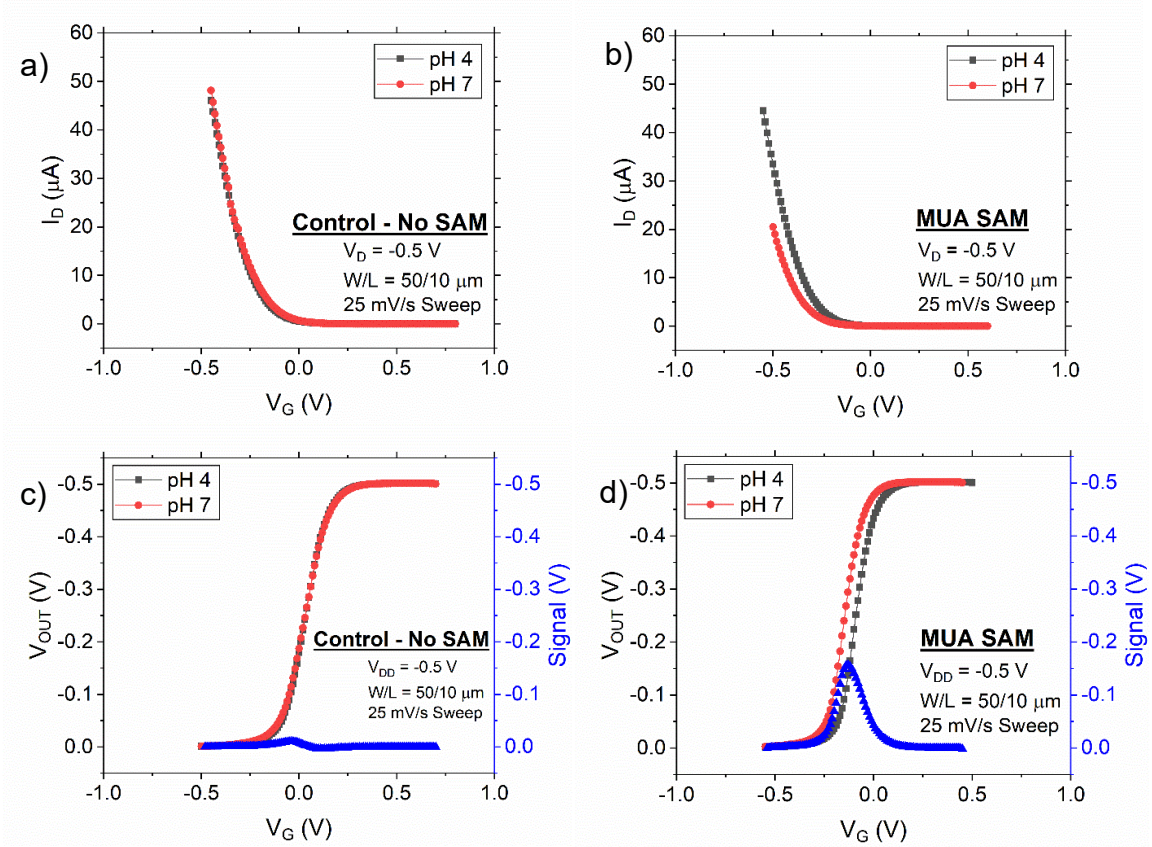

Fig 4.4. Charge Sensing.[115] (a) Transfer curves for a control device with no SAM at FG2. The curves with pH 4 and pH 7 overlap, indicating no difference in response to the solution pH. (b) Transfer curves for an example device with a MUA SAM at FG2. The pH 7 solution yields a shifted transfer curve due to the deprotonation of the MUA layer and the consequent charge accumulation at the FG2 surface. (c) Inverter measurements for the control device with no SAM. The difference signal between the two curves is shown in blue, with the corresponding scale on the blue right-hand y-axis. The two inverter curves overlap, and the signal peak is negligible. (d) The corresponding inverter curve for the MUA-coated device, with the difference signal shown in blue. The pH 7 curve is shifted negatively compared to the pH 4 curve, and the difference signal generated upon subtracting the two curves is symmetrical around its 160 mV peak. This figure is taken from Thomas, M.S., Dorfman, K.D., Frisbie, C.D.; Detection and Amplification of Capacitance and Charge-based responses by Floating Gate Electrolyte Gated Transistors, Flexible and Printed Electronics (2019), 4(4), 044001, first published on November 1st, 2019. DOI: https://doi.org/10.1088/2058-8585/ab4dcf.

In comparison to this control, when the FG2 surface with a C12 monolayer is included in the circuit, as shown in Fig 4.3b, the slope of the curve is lowered, which results in the final current being reduced by 50% compared to the measurement of the transistor alone. This is caused by the reduction of capacitance due to the presence of the monolayer at the FG2 surface. Fig 4.3c shows the corresponding inverter curve for the control device. The two curves measured for the control device are close to each other resulting in a signal peak of about 10 mV. In contrast, the inverter curves for the sample device in Fig 4.3d with a C12 monolayer at the surface, show a considerable difference. The slope of the transition from V_{DD} to ground is smaller, and larger voltages are required to obtain $V_{OUT} = 0$ V. This results in a signal peak that is skewed negatively and the peak itself is found to be 160 mV, which can be clearly differentiated from the control signal peak of 10 mV obtained for a device with no monolayer at the surface.

To compare the capacitive signals with charge-based signals, another experiment was conducted where MUA monolayers are attached to the FG2 surface and exposed to pH 4 and pH 7. As the pK_a of MUA is close to 7,[103,104] the partial deprotonation of MUA should cause interfacial charge creation at FG2. The corresponding negative control device in Fig 4.4a has a bare gold FG2, which yields transfer curves that are nearly identical when exposed to pH 4 and pH 7, with small differences which could be caused by preferential adsorption of ions to the FG2 surface.[118] The sample device with MUA-functionalized FG2 is exposed to pH 4 and pH 7, causing a shift between the two transfer curves as shown in Fig 4.4b, similar to previous studies.[101]

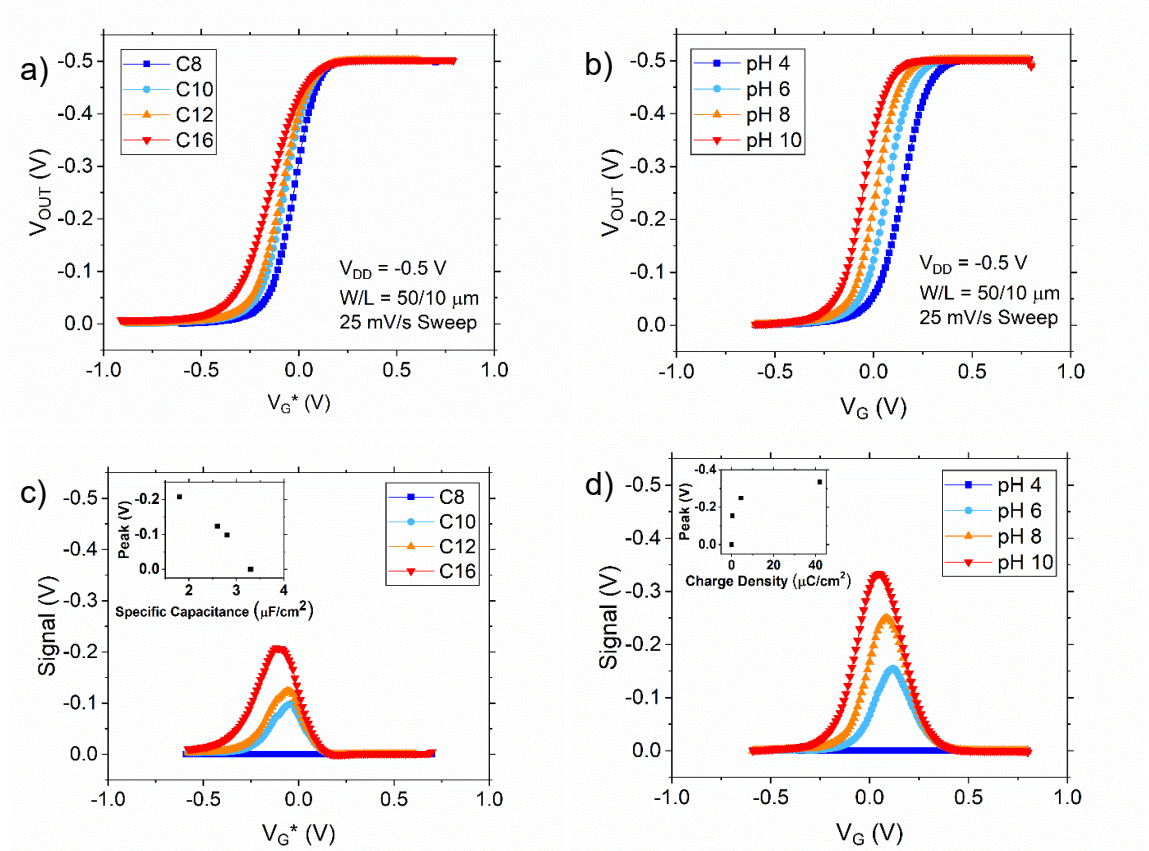

Fig 4.5. Comparison of capacitance and charge responses.[115] (a) Inverter curves for devices with C_8-, C_{10}-, C_{12}-, and C_{16}-SH SAMs. The curves are shifted so that V_{OUT} = -0.49 V occurs at the same V_G for all the curves. Gain decreases with the length of the molecules in the SAM at the FG2 surface, as expected. (b) Inverter curves for an example device with a MUA SAM exposed to solutions with pH = 4 - 10. As pH increases, the curves shift negatively due to a larger negative surface charge density at FG2. (c) Difference signals generated by subtracting the inverter curves in (a), with the C_8-SH curve serving as the reference. The difference curves are skewed negatively, and the peak and skew are larger for thicker SAMs. The inset shows signal peaks plotted against the specific capacitance of the FG2-aqueous electrolyte interface. (d) Difference signals from the shifted inverter curves for the sample device with a MUA SAM. Inset shows signal peak vs charge density at the FG2 surface. This figure is taken from Thomas, M.S., Dorfman, K.D., Frisbie, C.D.; Detection and Amplification of Capacitance and Charge-based responses by Floating Gate Electrolyte Gated Transistors, Flexible and Printed Electronics (2019), 4(4), 044001, first published on November 1st, 2019. DOI: https://doi.org/10.1088/2058-8585/ab4dcf.

The corresponding inverter curves also reflect this difference and upon subtraction, create the difference curve shown in Fig 4.4d which is found to be symmetric about the

peak. This differs from the capacitive difference curve in shape, as the capacitive curve skews negatively. The peak of the charge-based signal is found to be 160 mV, while the corresponding control device yields a difference curve with a peak close to 10 mV, which is an order of magnitude smaller than that obtained for the sample device. This measurement, along with the previously described capacitance-based signal, provide an indication that both charge and capacitance-based signals could be detected by the device. Additionally, the change in slope observed in capacitive signals and the lack of slope change observed in charge-based signals could provide a method of distinguishing between the origin of signals for different analytes based on signals alone.

The two responses are compared more thoroughly using a series of experiments with both alkylthiol and acid-terminated thiols. Devices with C8-, C10-, C12-, and C16-thiol monolayers are measured to obtain the cascading set of measurements in Fig 4.5a. With C8 as a reference, the other inverters are subtracted to yield difference curves that are increasingly skewed as the length of the molecule and consequently the thickness of the monolayer is increased and hence the capacitance is decreased. The lower capacitive coupling at FG2 requires more negative voltages to switch on the devices. The signal peaks shown in Fig 4.5c increase with increasing monolayer capacitance, as the difference between the monolayer and the reference C8 monolayer increases. A capacitance sensitivity of 70 mV/(μF/cm^2) is calculated FG2/channel area = 1000.

For charge sensing, a FGT device with MUA-functionalized FG2 surface was exposed sequentially to pH 4, 6, 8, and 10 solutions to increase the charge density and record the device sensitivity towards charge. The inverter curves measured at different pH

are shifted laterally, as shown in Fig 4.5b, as observed in the previous study on the role of interfacial charge. The laterally shifted responses yield the symmetric difference curves depicted in Fig 4.5d, unlike the curves observed for capacitance-based inputs. Signal peaks of up to 300 mV are observed for 10 mM electrolyte concentration, and the surface charge density obtained during previous work with MUA monolayers is utilized to calculate a charge sensitivity for FG2/channel area = 1000. The response is non-linear, as can be expected from our understanding of the relationship between surface charge and the potential (hyperbolic sine) it creates across the double layer. The average slope between each consecutive point yields a charge sensitivity of 40 mV/(μC/cm^2).

4.4 Conclusion

To demonstrate the utility of EGT-based sensors in the detection of neutral molecules – an important class of targets for the monitoring of human health and the environment, alkylthiol SAM was bound to the sensing surface and the device response was recorded, with a bare gold FG2 surface as a negative control. Inverter curves were utilized to amplify the responses and yielded a skewed difference curve upon subtraction from a reference EGT measurement. A decrease in capacitive coupling was observed upon the presence of the monolayer, with the control yielding a negligible signal. To further validate the capacitance sensing characteristics of the FGT device, SAMs of increasing lengths (C8 to C16) were bound to the sensing surface and increasing the lengths of the molecules resulted in increasingly skewed difference curves. Difference curve peaks ranging from 50 mV to 200 mV were utilized to calculate a capacitance sensitivity of 70 mV/(μF/cm^2). To contrast this response with the previously studied charge response,

MUA-functionalized devices were exposed to solutions of pH 4 to 10. The measured inverter curves were shifted laterally, and yielded symmetric difference curves upon reference subtraction, and control device of bare gold sensing areas yielding flat difference curves. The peaks were used to calculate a sensitivity of 40 mV/(μC/cm^2).

This work demonstrates the possibility of EGT-based capacitance detection at quasi-static measurement modes and provides distinguishable characteristics between the charge and capacitance based responses of the device. Additionally, it also addresses the issue of chemical detection without the use of charge-based inputs or high frequency measurements, an important problem for the broad application of transistor-based sensors.

Chapter 5. Modeling and Sensitivity Predictions

5.1 Introduction and Motivation

The previous studies focused on understanding the charge and capacitance sensing capabilities of the FGT device for a fixed device design (throughout each study). In this chapter, the device design is changed and its impact on sensitivity is investigated. A model for the device response is developed by adapting existing transistor equations to the FGT inverter, which can be fit well to EGT responses. The model predictions are compared with experimental values of inverter gain, capacitance sensitivity, and charge sensitivity. Important variables and variable groups that can reliably predict the device response are identified for better understanding and optimization of the device. These include a parameter that includes material performance and load resistor value, a factor that accounts for the capacitive coupling of applied gate voltage in the device, and the intrinsic threshold voltage of the semiconductor. Finally, a set of recommendations is provided for charge and capacitance sensing which are generally applicable to all floating gate transistor devices, not just EGTs.

5.2 Modeling

We begin by deriving a model for predicting V_{OUT} vs V_G. This can be divided into two sections – deriving a model for V_{OUT} vs V_{IN} (the potential in the ion-gel gate dielectric), and then deriving a relationship between V_{IN} and V_G.

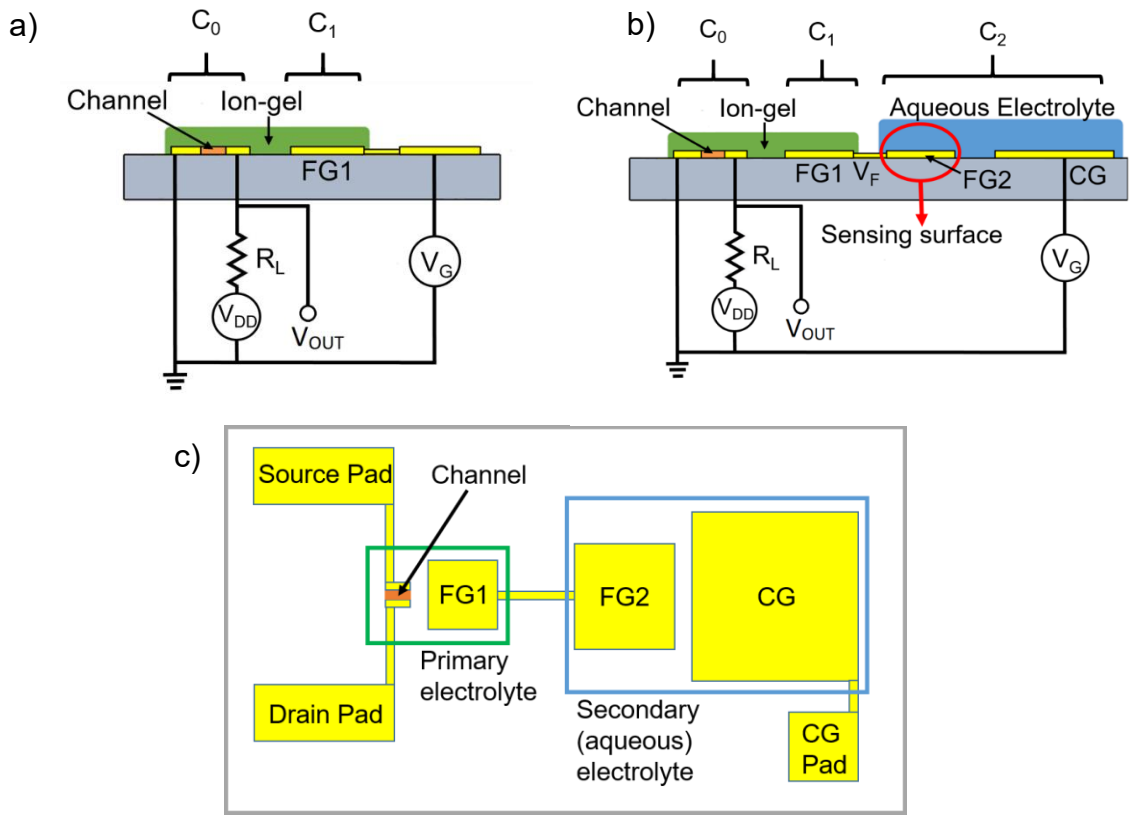

Fig 5.1. Device/Circuit Structure and Design. (a) Side-gated EGT device structure and inverter measurement circuit. V_G is applied at the gate pad, supply voltage (V_{DD}) is applied across both EGT and the load resistor (R_L), and V_{OUT} is measured between the channel and the load resistor. The semiconductor channel (orange) consists of P3HT. (b) The corresponding FGT device with the inverter circuit used for measurement. Key interfacial capacitances C_0, C_1, C_2 are labelled; C_2 is a lumped capacitance for CG and FG2 surfaces, but C_2 effectively tracks the capacitance of the FG2-aqueous electrolyte interface because the area of the control gate (CG) is kept at least 10x larger than the area of FG2. (c) Top-view scheme of the FGT device in (b) showing the different components such as the channel, FG1, FG2, CG and the electrolytes contacting them, along with the source, drain and CG pads for measurement. The diagram shows the cascading areas of CG, FG2, FG1, and channel. To show all relevant details, the figure is not to scale.

Fig 5.1 reiterates the FGT device and inverter circuit used for this work. The potential is dropped across the transistor and the load resistor based on the dynamic resistance of the transistor, which is altered by V_{IN}.

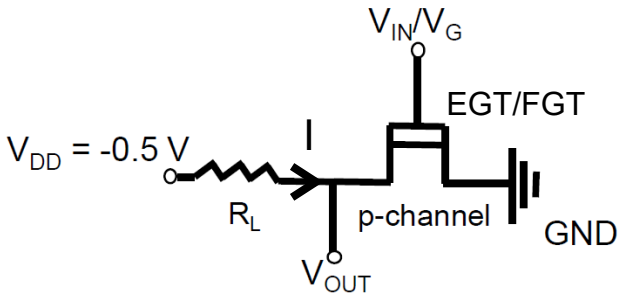

Fig 5.2. Inverter Circuit Simplified. The EGT or FGT is connected in series with a resistor and V_{OUT} is measured between the two. The supply voltage V_{DD} is kept at -0.5 V, and the source terminal of the transistor is grounded. The current flowing through the circuit is marked as I, which has a negative sign according to the convention (flowing from supply to ground terminal).

A proxy for this dynamic resistance is the current flowing through the source drain channel, similar to Eq. 1.1

$$I_D = -\frac{\mu C_i W}{L}\left[(V_G - V_T)V_D - \frac{(V_G - V_T)^2}{2}\right] \tag{5.1}$$

where μ is the device mobility, C_i is the semiconductor/dielectric specific capacitance, W and L are the width and length of the channel, and V_T is the threshold voltage of the device.

The formula for I_D shown here is called the square law equation. The negative value results from the assumption of current direction, from supply to ground in the circuit as a whole. This equation yields the two regimes (saturation and linear) in Eq 1.2 and Eq 1.3, based on the voltage at the dielectric and the voltage at the drain terminal, assuming the source is grounded. Here the voltage at the dielectric is V_{IN}, and the drain terminal is the voltage V_{OUT}. As V_{OUT} depends on V_{IN}, the regime of I_D also changes as V_{IN} is changed during a single sweep. This is a key difference between the inverter operation and traditional transfer curve measurement.

The circuit shown in Fig 5.2 (with V_{DD} = -0.5 V) yields the equation

$$V_{DD} - IR_L = V_{OUT} \tag{5.2}.$$

Substituting I_D as the series current I into this equation gives us

$$V_0(V_{DD} - V_{OUT}) = -\left[(V_{IN} - V_T)V_{OUT} - \frac{{V_{OUT}}^2}{2}\right] \tag{5.4}.$$

This can then be solved to obtain the value of V_{OUT} as a function of V_{IN}. The quadratic equation yields two solutions, and the negative one is selected (as $V_{DD} < V_{OUT} < 0$)

$$V_{OUT} = (V_{IN} - V_T - V_0) + [(V_{IN} - V_T - V_0)^2 + 2V_0V_{DD}]^{1/2} \tag{5.5}.$$

We can now check for the limits of validity for this equation. We have already imposed $V_{OUT} < 0$ by selecting the negative root, and as V_{OUT} must always be real in a quasi-static measurement, an additional criterion that V_{OUT} must be real is imposed. Consequently, the discriminant of the quadratic equation in Eq 5.4 must be positive. This gives us the limit

$$V_{IN} - V_T < V^* \tag{5.6},$$

with

$$V^* = -\sqrt{-2V_0V_{DD}} + V_0 \tag{5.7}$$

serving as the transition point between the full square law region, and the saturation current region.

For V_{IN} - V_T values greater than V*, this implies that we need to make reasonable assumptions to change Eq 5.5 to a physically realistic formula. From chapter 1.2, we know that when the source-drain potential is high enough, all the charge carriers generated in the

semiconductor are swept across by the voltage, and the effective drain voltage remains the same, upon further increase of the applied drain voltage. This results in the saturation regime operation described previously in chapter 1.2. The right-hand side in Eq. 5.4 is substituted as V_{IN} - V_T to yield a new equation for V_{OUT} that is valid for V_{IN} - V_T > V*

$$V_{OUT} = V_{DD} + \frac{(V_{IN} - V_T)^2}{2V_0} \tag{5.8}.$$

The summary of the relationship between V_{OUT} and V_{IN} can hence be summarized as

$$V_{OUT} = \begin{cases} V_{DD} \\ V_{DD} + (V_{IN} - V_T)^2/2V_0 \\ (V_{IN} - V_T - V_0) + [(V_{IN} - V_T - V_0)^2 + 2V_0 V_{DD}]^{1/2} \end{cases} \quad \begin{matrix} V_{IN} - V_T < 0 \\ \text{for } 0 > V_{IN} - V_T > V^* \\ V_{IN} - V_T < V^* \end{matrix} \tag{5.9}.$$

The next step is to obtain a relationship between V_{IN} and V_G, which is made significantly easier by the quasi-static measurement mode, which allows the treatment of all four interfaces in the device as purely capacitive. The capacitance of the FG2 and CG surfaces is lumped to form C_2, and the channel and FG1 capacitances are named C_0 and C_1 respectively. A series sum of these capacitances yields $V_{IN} = \kappa V_G$, where

$$\kappa = \frac{C_1 C_2}{C_1 C_2 + C_1 C_0 + C_0 C_2} \tag{5.10}.$$

The variable κ can be further split into $\kappa_{EGT} \times \kappa_{CG}$, for

$$\kappa_{EGT} = \frac{C_1}{(C_1 + C_0)} \tag{5.11},$$

and

$$\kappa_{CG} = \frac{(C_1+C_0)C_2}{C_1C_2+ C_1C_0+C_0C_2} \quad (5.12).$$

This splitting provides a convenient way to represent the capacitive losses at each interface or group of interfaces. The relationship between V_G and V_{IN} is substituted into Eq. 5.9 to yield the relationship between V_G and V_{OUT}

$$V_{OUT} = \begin{cases} V_{DD} \\ V_{DD} + (\kappa V_G - V_T)^2/2V_0 \\ (\kappa V_G - V_T - V_0) + [(\kappa V_G - V_T - V_0)^2 + 2V_0V_{DD}]^{1/2} \end{cases} \quad \begin{matrix} \kappa V_G - V_T < 0 \\ \text{for } 0 < \kappa V_G - V_T < V^* \\ \kappa V_G - V_T > V^* \end{matrix} \quad (5.13).$$

An additional element must be added to this analysis to account for potential shifts at FG2. If we assume that the potential drop at CG is negligible, and the potential in the sensing medium is uniformly V_G, the potential shift can simply be added to V_G, resulting in a potential of $V_G - \phi$ that must be coupled capacitively to the channel. This is consistent with the understanding of the charge response described in chapter 3. ϕ can be expanded as Grahame's equation, which results in a term nonlinearly dependent on electrolyte concentration and surface charge density, as described in chapter 3. With the added assumption that ϕ is during a measurement, we obtain the final form of the equation

$$V_{OUT} = \begin{cases} V_{DD} \\ V_{DD} + (\kappa V_G - V_T - \kappa\phi)^2/2V_0 \\ (\kappa V_G - V_T - \kappa\phi - V_0) + [(\kappa V_G - V_T - \kappa\phi - V_0)^2 + 2V_0V_{DD}]^{1/2} \end{cases} \quad \begin{matrix} \kappa V_G - V_T - \kappa\phi < 0 \\ \text{for } 0 < \kappa V_G - V_T - \kappa\phi < V^* \\ \kappa V_G - V_T - \kappa\phi > V^* \end{matrix} \quad (5.14).$$

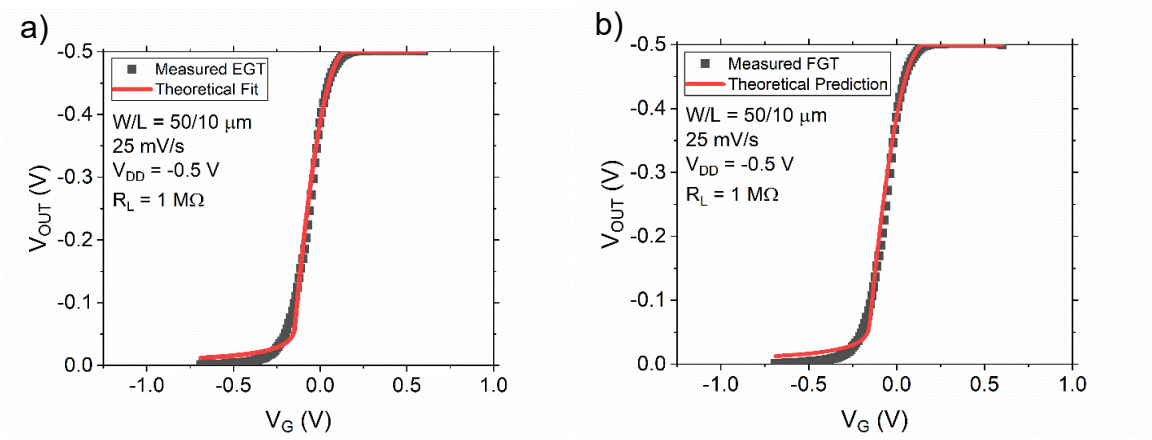

Fig 5.3. EGT and FGT responses.[115] (a) The measured inverter curve for the EGT (black) along with the model fit to the data, shown in red. W and L are the width and length of the semiconductor channel respectively. The RMSE for the three-parameter fit is found to be 12 mV (see text). (d) The measured FGT inverter output is shown in black, and the *prediction* for the FGT device, based on parameters extracted from the EGT inverter fit, is shown in red. The RMSE is found to be 13 mV. The FG2 area is kept large (10,000x the semiconductor channel area), and the resulting curve is similar to the EGT due to negligible potential drop across FG2 and CG.

This representation now allows us to identify the five parameters that can affect the response of the device: V_T, V_0, κ, V_{DD}, and ϕ. V_T is the intrinsic threshold voltage of the semiconductor and V_0 can be thought of as the transconductance (dI/dV_{IN}) of the device normalized by V_{OUT} and multiplied by the load resistance R_L. κ is the capacitive coupling constant, V_{DD} is the supply voltage, and ϕ represents excess potentials introduced at the sensing area (FG2). Of these, κ can be modified continuously by changing the area of the FG1, FG2, and CG surfaces. V_0 can also be altered by changing the channel dimensions, or the load resistance value, as well as by using different semiconductor or dielectric materials. The effect of load resistance is depicted in Fig B.2. V_T is generally not modified easily independently in a controlled fashion, and ϕ usually corresponds with an input which is being detected. This suggests that V_0 and κ are the parameters that can be tuned by

changing the geometry of the device, once the materials, and consequently, the operating parameter limits (V_{DD} and R_L) are known.

To test the validity of the model against a known inverter, we use a previously measured EGT inverter curve as a reference. Since the model is derived more generally for a FGT, it can be adapted easily for an EGT. κ_{CG} is set to 1 (which means $\kappa = \kappa_{EGT}$) and ϕ is set to 0 V to obtain the EGT model. This simplified model is fit to the inverter response for the EGT shown in Fig 5.3a with V_{DD} = -0.5 V (this is the supply voltage used in experiments), and the minimum RMSE fit (RMSE = 12 mV) yields V_T = 0.03 V, V_0 = 4 mV, κ = 0.2. V_T has been reported as -0.30 $\pm$ 0.05 V for P3HT EGT devices measured in nitrogen environments, but values close to 0 V are plausible for high air doping of the P3HT film, since all fabrication and testing is carried out in air. The fit is closer in the saturation regime, and deviates from the experimental curve at more negative V_G, when the device is switched on. This is believed to be due to higher source-drain currents, which result in lower transistor resistance. This implies that the transistor resistance is no longer the major contributor to the series resistance, and the assumption that the circuit current can be approximated by the transistor drain current equation may no longer be valid.

To further obtain the total capacitance of the EGT (the series capacitance of C_0 and C_1), a displacement current measurement is carried out as shown in Fig B.3. (Appendix B), which, along with the C_0/C_1 ratio of 4, yields C_0 = 28 nF, and C_1 = 7 nF. This measurement consists of fixing the source-drain bias at 0 V and sweeping the gate voltage at increasing sweep rates while recording the gate current. A linear fit to the current vs sweep rate curves yields the capacitance of the device. The obtained values of C_0 and C_1 can then be used to

calculate κ_{CG} for different values of C_2 (calculated using FG2 and CG areas, and assuming the specific capacitance of water-gold interface to be 10 μF/cm^2). This allows us to predict the behavior of an FGT from the corresponding EGT measurement. The prediction of the model is compared to the experimental inverter curve for the control device in Fig 5.3b (previously shown in Fig 4.3a) and is found to match it closely (RMSE = 13 mV). We can now use the extracted reference values of the parameters to predict the FGT gain, capacitance sensitivity, and charge sensitivity for a range of FG2 areas, both to assess the validity of the model and to investigate trends for these outputs with sensing area size.

5.3 Experiments

FGT devices were fabricated with channel dimensions W/L = 50/10 μm, FG1 = 150x the channel area, and CG = 20000x the channel area. FG2 areas were changed from 50x the channel area to 10000x (50x, 100x, 500x, 1000x, 5000x and 10000x) the channel area (all pads are square except the source and drain). The experimental protocols for printing and PDMS well preparation were similar to those described in chapter 2. The required gold pads were fabricated using lithographic techniques onto Si/SiO_2 wafers, and printing is employed to complete these devices. The FG2 surface was functionalized by exposing it using PDMS wells to solutions of acid-terminated thiols (11-MUA) or alkylthiols (C8- and C16-thiols) for charge and capacitance sensing respectively. Inverter curves were measured with 10 mM aqueous KCl at pH 7 as the secondary electrolyte for alkylthiol monolayers and pH 4 and pH 10 solutions (altered by the addition of HCl or KOH) for the acid-terminated monolayers. For gain measurements, ion-gel was printed over FG2 and CG as well, and inverter curves were measured in a similar manner as in

chapter 4, using a Keithley 2611B to apply V_{DD}, a Keithley 2400 to apply V_G, and a Keithley 2612 instrument to measure V_{OUT} – all controlled by a LabView code.

5.4 Results and Discussion

The FGT gain is an important measure of the amplification capabilities of the device and is calculated as $-(dV_{OUT}/dV_G)$. For experimental curves, it is calculated as the slope at $V_{DD}/2$ and can be compared to the model with a derivation from the model.

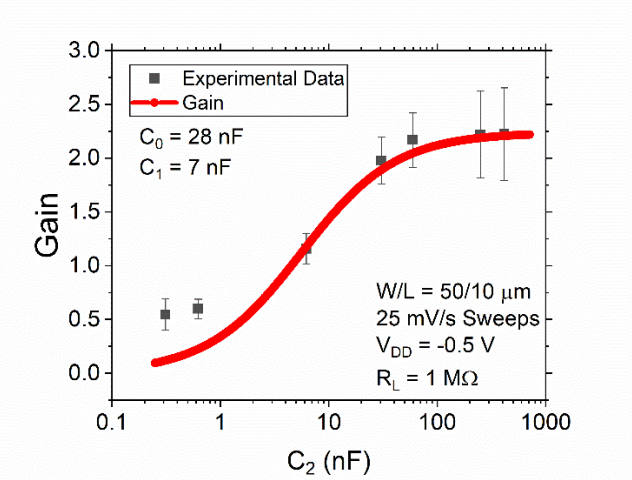

Fig 5.4. Gain Comparison. Gain vs C_2 (FG2 and CG capacitance in series). The gain is calculated by taking the slope of the inverter curve (Fig. 5.3b) at the center ($V_{OUT} = V_{DD}/2$). C_2 is varied by changing the area of FG2 (bare gold in contact with ion-gel). The prediction of the model is shown in red, which matches well with the experimental data in black. Lower capacitive coupling (i.e., greater potential drops) at FG2 causes the gain to drop as C_2 approaches, and eventually becomes lower than C_0 and C_1. The data points represent the mean and standard deviation of at least 3 separate devices at each point.

This results in the formula for gain

$$\text{Gain} = \kappa\sqrt{\frac{-V_{DD}}{V_0}} \tag{5.15}$$

From this prediction, we see that higher gain is obtained with higher capacitive coupling (κ), higher supply voltage V_{DD}, and lower V_0 (corresponding to higher EGT transconductance). V_0 obtained from the EGT fit, κ (as calculated from C_0, C_1, and C_2), and the V_{DD} (= -0.5 V) are used to predict gain as a function of C_2.

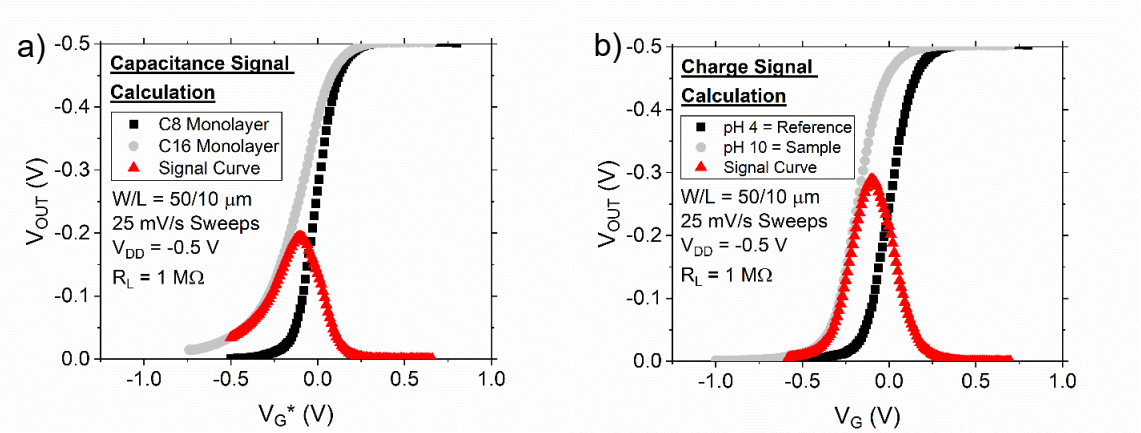

Fig 5.5. Signal subtraction (difference curves). (a) Examples of experimentally measured inverter curves for C8 and C16 monolayer functionalized FGT devices, shown in black and gray respectively. The C16 curve is shifted so that V_{OUT} crosses 99% of the negative plateau at the same V_G as the C8 curve.[115] The x-axis is consequently labeled V_G*. The difference curve in red is calculated by subtracting the black curve from the gray curve. (b) Example measured inverter curves for a MUA-functionalized FGT device exposed to pH 4 and pH 10 are shown in black and gray respectively. The corresponding difference curve is shown in red.

C_2 is determined from the specific capacitance of the ion-gel-gold interface reported previously and FG2 areas, and the experimentally derived gain is plotted against it along with the theoretical prediction in Fig 5.4. Gain increases as C_2 is increased and plateaus at large values of C_2 (> 100 nF). The model follows the experiments closely for C_2 > 1 nF. The model assumes that the capacitance remains constant throughout the range of C_2, but lower values of FG2 area result in larger potential drops at FG2, causing increases in the specific capacitance. The deviation at lower C_2 can hence be explained by the voltage

dependence of capacitance due to excess ions being squeezed into the double layer by the applied voltage.[65] This phenomenon is seen in ionic liquids with residual moisture as well,[119] which is the expected state of the ion-gel for the experiments in this study, as the preparation, storage and printing of ion-gel occurs in air. Another possible explanation for the deviation at lower FG2 areas is electrochemical breakdown of this water that could occur at higher potential drops, that could pin the voltage at the floating gate and cause higher than expected inverter slopes.

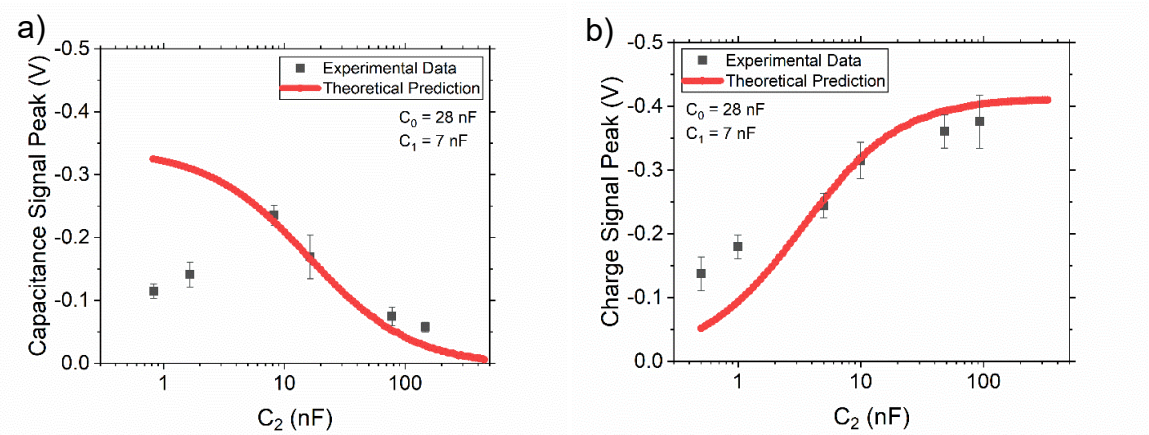

Fig 5.6. Charge and capacitance signal trends. The experimental data are in black, while the model predictions are in red. (a) Signal peaks between C16 and C8 monolayers calculated by subtracting the two inverter curves. Each data point represents an average of at least three FGT devices at a specific areal size for FG2 coated with a C16 SAM; different points correspond to different FG2 areas. Peaks increase until C_2 = 10 nF, after which the experimental data deviate from the model. (c) Signal peaks calculated between a MUA monolayer at pH 4 and pH 10, calculated by subtracting the two inverter curves. Each data point represents an average of three FGT devices at a specific areal size for FG2 coated with MUA and exposed to pH 10; different points correspond to different FG2 sizes. The peaks follow the model, with some deviations at lower values of C_2. The data points represent the mean and standard deviation of at least 3 separate devices at each point.

We further calculate the capacitance and charge sensitivity using both experimental data and the model. Devices with C8- and C16- monolayers are measured for each FG2

area, and the curves are subtracted to obtain a difference curve in Fig 5.5a, whose peak is taken as the final signal. To isolate capacitance effects and remove differences created by device-to-device V_T variation, the C16 curve is shifted so that the switch on V_G (V_{OUT} = $0.99V_{DD}$) matches that of the C8 curve. To predict the capacitance signals with the model, V_0 = 4 mV, V_T = 0.03 V are fixed, and the previously calculated values of C_0 = 28 nF and C_1 = 7 nF, specific capacitance values for C8 and C16 monolayers obtained from cyclic voltammetry measurements, and FG2 area are utilized. Inverter curves are calculated, shifted so that they switch on at the same V_G (to match the experimental data), and subtracted, with the peaks of the resulting difference curves taken as the signals. The comparison of theoretical and experimental signals for capacitance and charge is shown in Fig B.4.

The model prediction is plotted in red along with the experimentally obtained data in black in Fig 5.6a. The signal decreases as C_2 is increased beyond 10 nF and the model matches the experimental data closely. However, the experimental signals peak at C_2 = 10 nF and reduce for smaller C_2, while the model predicts that signals continue to increase and plateau for smaller C_2. The discrepancy is likely due to higher capacitances at the FG2 surface caused by higher applied potential, as opposed to the constant capacitance assumed during model derivation. As the capacitance increases with potential, the smaller capacitance (C16) is increased to a greater degree than the larger one (C8) due to correspondingly larger potential drops at the C16 monolayer. This renders the actual difference in the capacitances much smaller than what is assumed by the model, and hence results in correspondingly smaller signals than the model prediction.

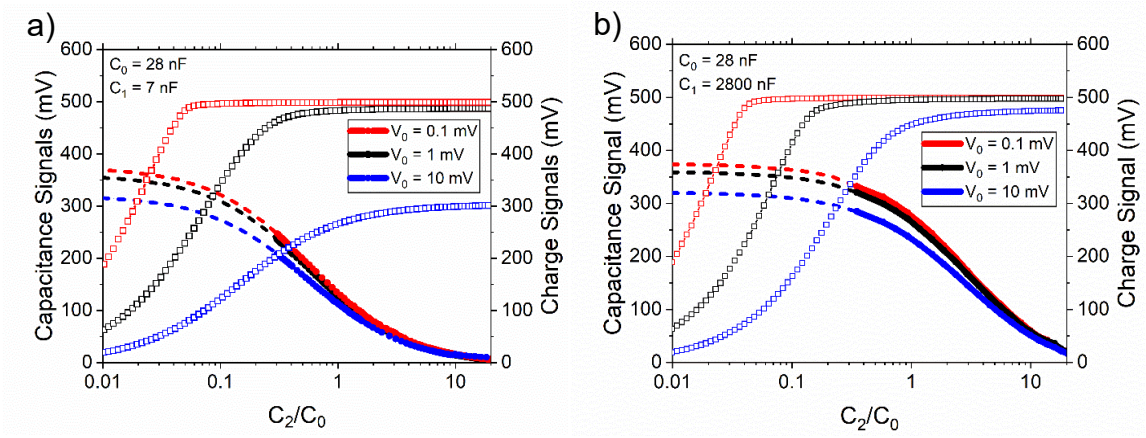

Fig 5.7. Predicted signals. (a) Capacitance (left y-axis) and charge signals (right y-axis) are plotted across four orders of magnitude of C_2/C_0, and three values of V_0. For specific values of V_0 and C_0, calculated using available material parameters and channel dimensions, the optimum value of C_2 can be obtained from this prediction and the required area of the floating gate can be calculated. Here, C_0 = 28 nF, and C_1 = 7 nF. The region at small C_2/C_0 where the predicted capacitance signals deviate from the experimental values is dashed. (b) The figure from (a) is replotted, but with C_1 = 100 x C_0, to investigate the effects of an optimal C_1/C_0 ratio. The charge signals for higher V_0 are increased while the higher V_0 curves remain the same. The capacitance signal plateaus extend to higher values of C_2/C_0 and could be achieved for larger sensing area capacitances.

The corresponding charge signals for the same areas are predicted by calculating inverter curves with V_0 = 4 mV, V_T = 0.03 V, the previously calculated values of C_0 and C_1, and C_2 calculated from reported values of MUA-gold specific capacitance and FG2 area. ϕ is fixed at 0 V for pH = 4, and 0.2 V for pH = 10, and the two curves are subtracted to give a difference curve, and its peak is taken as the signal for the model prediction. Fig 5.6b shows the comparison of the experimental data (calculated by subtracting the measured inverters for pH = 4 and pH = 10 solutions for the same FGT device) and the model for charge signals. The signals increase as C_2 is increased and plateau for C_2>100 nF, following the same pattern as the gain. The model follows the experimental signals closely from C_2>1 nF, but deviates from it for smaller FG2 sizes. This arises from the

incorrect assumption in the model that the capacitance of the FG2-water interface remains constant, when it actually increases as potential drops at the FG2 surface increase as FG2 area is reduced.

The thorough comparison of the model with experiments now allows us to use it more confidently to predict the impacts of other surfaces in the device, as well as to explore material properties and operating conditions that would enhance the signals. Fig 5.7a shows the capacitance and charge signals plotted against C_2/C_0 for 3 different values of V_0. CG is assumed to be much larger than any of the other 3 pads, ensuring that minimal potential is dropped the CG surface. The capacitance signals increase as C_2/C_0 is lowered due to larger potential drops at the sensing area, making it more sensitive to capacitive changes. As the capacitance signals are found to deviate from the model below $C_2/C_0 = 0.3$, the curves are represented as dashed lines for this region. The charge signals follow a similar trend as the gain, increasing with C_2/C_0, and plateauing at higher sensing areas. We can see that increasing V_0 improves both capacitance and charge signals, implying that higher mobility and dielectric specific capacitance is favorable for sensing applications – which makes sense. This also implies that higher load resistances should offer higher sensitivity, as long as the underlying assumption regarding the circuit current and potential drops remain accurate. The plateaus for the charge signals occur due to the limit of $V_{DD} = -0.5$ V. The subtracted signal cannot be higher than this value, and any further increases require increases in V_{DD}, which in this case, causes more rapid performance degradation. In general, V_{DD} should be kept as high as material and stability limits allow. It must be noted that the assumptions that go into deriving this model could limit its generality with regard to some semiconductor materials. This includes assumptions behind the use of the square

law equation such as the assumption of non-hopping transport (drift or diffusion), which may not be valid if the material, especially at the lower range of its mobility, does not lie in this regime.

We now turn to C_0 and C_1 – the capacitances representing the channel and FG1 (the first arm of the floating gate). A smaller C_0 value allows for larger ranges of C_1/C_0 to account for different inputs the device might detect. On the other hand, larger dielectric specific capacitances (which result in larger C_0 values) ensure low voltage operation, one of the key advantages of the platform. This can be addressed by keeping the channel area as small as fabrication limits allow. In this study, $C_0/C_1 = 4$ and the device works well for both charge and capacitance sensing. However, increasing C_1 can have positive effects on the device performance and sensitivity, and this is shown in Fig 5.7b, where $C_0/C_1 = 1/100$. While larger C_1 did not have a substantial effect for charge signals with smaller V_0, it can significantly improve the sensitivity for higher V_0 (lower device performance). The plateau values for charge signals remain the same, as the maximum possible signal is already reached for $V_{DD} = -0.5$ V. The plateaus for capacitance signals are observed at higher C_2/C_0 values with the signals observed to be higher than those with $C_0/C_1 = 4$ throughout the curve. This indicates that a combination of smaller channel areas and comparatively larger FG1 areas (so that $C_1 > C_0$ at least) optimizes the sensing capabilities of this platform.

5.4 Conclusion

This study builds upon the previously described charge sensing, capacitance sensing and signal amplification experiments. In this work, we have developed a model that predicts the response of floating gate EGTs and validated it against experiments.

Previously understood transfer curve equations are adapted to the floating gate inverter and a piecewise model is derived to predict the output. The model yields several parameters that control device response, including a parameter that quantifies capacitive coupling, one that accounts for the transconductance of the transistor, and another parameter that represents the threshold voltage of the semiconductor. The model is fit to a previously measured control EGT, and the extracted values of parameters are used to predict the FGT response. The prediction is found to be accurate and these extracted values are then used to predict charge and capacitance signals across a wide range of sensing areas. Self-assembled monolayers (SAMs) are utilized to introduce controlled perturbations at the sensing area, with alkylthiol and acid-terminated molecules implemented respectively. The capacitance signals decrease with increasing sensing area size and are well-predicted by the model for larger areas. The charge signals increase as the sensing pad is enlarged, and is also matched closely by the model, except for smaller areas. The discrepancies can be explained by capacitance increases at low sensing area sizes due to larger potential drops at the sensing surface, which are not accounted for by the model.

The model is further used to predict signals for different values of the controllable parameters, to characterize device response for different materials and operating parameters. Higher semiconductor mobility and dielectric specific capacitance always appear to yield larger signals, along with higher supply voltages, and load resistances – as long as device stability and material breakdown are accounted for. The sensing area should be maximized for charge sensing, while optimum capacitance sensing is achieved when its capacitance is the same as that of the channel. The control gate and the first arm of the floating gate (FG1) should be kept as large as possible to minimize potential drops at these

surfaces and enhance both performance and sensitivity of the device as a whole. The results shown in this study are generally applicable to floating gate transistors, regardless of materials choice. This implies that once the material properties of the transistor and the interfaces are known, device design can be implemented with simple rules that can be adapted to multiple sensing platforms that utilize floating gate transistors.

Chapter 6. Summary and Future Work

6.1 Summary

Floating gate transistors are promising sensing devices that overcome several drawbacks of previous transistor-based chemical sensor designs. The floating gate separates the transistor and sensing sections, allowing for independent optimization of these sections and the use of well-characterized functionalization techniques for sensor preparation. Device degradation and cross-contamination between sensing and transistor compartments is also avoided with the use of a floating gate. The use of an electrolyte dielectric provides additional advantages such as sub 1 V operation and the possibility of fabrication with fast and simple techniques such as printing, and possible future integration into roll-to-roll manufacturing. The combination of these two elements results in the Floating Gate electrolyte-gated Transistor (FGT), which was invented at the University of Minnesota. The FGT platform has been successfully employed for the detection of DNA,[81] ricin,[82] and gluten[85] in liquid media. However, the generalizability of the platform and the underlying mechanism remained unclear. The complex structure of the device, consisting of 4 interfaces and several adjustable parameters required optimization and further understanding to enable widespread usage in chemical sensing applications. This work employs self-assembled monolayers (SAMs) to alter the interfacial properties of the sensing area in a controlled fashion to elucidate and quantify its sensing mechanisms and optimize the device for use against different targets.

In the first study, 11-mercaptoundecanoic acid (MUA) SAMs are bound to the sensing surface and exposed to solutions of increasing pH to deprotonate the acid groups

and create a layer of surface-bound charge. Transfer curve measurements carried out at each pH value show shifts in the device response, which show sigmoidal behavior typical of acid-base reactions. The calculated pK_a is close to values reported in the literature. A RBS measurement is carried out to obtain a count of the molecular density and hence the surface charge density at complete ionization. This value is used to predict the potential created due to the surface charge with Grahame's equation, a result derived from Guoy-Chapman double layer theory. The potential calculated from transfer curve shifts and Grahame's equation yield similar values, indicating the equation's efficacy in predicting charge responses in the device. The electrolyte concentration is altered, and the experiments repeated to further asses the efficacy of traditional double layer theories in this device. The potential shifts are found to decrease with increasing concentrations above 1 mM, consistent with increased charge screening, and the slope is found to be close to that predicted by Grahame's equation. Additionally, the surface charge density is reduced by creating mixed monolayers at the sensing surface, which reduces the signals obtained from the device. This work is the first quantification of charge-based inputs and direct comparison with established double layer theory for transistor-based sensors.

While charge-based inputs represent the majority of transistor signals (both for the FGT and for other transistor-based platforms), an important class of targets are chemicals found in the human body such as food components and hormones. These targets can be hard to detect due to a lack of ionizable groups and high electrolyte concentrations found in bodily fluids such as sweat, urine, and blood.[110,111,120] This represents significant challenges for transistor-based detection and especially for many EGTs, as traditional dynamic measurements are not feasible for these devices due to lower ionic mobility. The

second study focuses on the detection of capacitive inputs and the amplification of signals produced by the FGT device. Alkylthiol SAMs with 8, 10, 12 and 16 carbon chains are bound to the surface of the sensing device, and inverter curves are employed to measure the responses. The inverters are found to become wider and the gain (slope) decreases as the length of the molecules are increased, and the capacitance is decreased. Difference curves calculated from a reference are found to be negatively skewed. A comparison with MUA-functionalized devices exposed to low and high pH results in potential shifts consistent with the previous study. In contrast to the capacitive signals, the charge-based signals result in higher and symmetric peaks when referenced from the lowest pH evaluated. The second study represents the first demonstration of capacitive transistor-based detection with a quasi-static technique. for the detection of charge and capacitance signals – inputs that encompass a wide range of target molecules.

Chapter 5 deals with the development of a model that predicts the inverter output as a function of applied voltages for the FGT, and the subsequent optimization of the device geometry and operating conditions for charge and capacitance-based sensing. The square law transfer curve equation is utilized along with the inverter circuit to yield a piecewise model for the inverter. The model yields 5 parameters that can influence the inverter output and include parameters that consist of variables concerning the material properties (V_0), capacitive coupling (kappa), and operating conditions (V_{DD}, V_0). A fit to a measured control EGT device provides reference values for these parameters. These values are used to predict the gain, charge sensitivity and capacitance sensitivity for a range of sensing area sizes for FGT devices with the same EGT design. The gain is found to increase as the sensing area is increased, culminating in a plateau. Alkylthiol SAMs are employed to

generate capacitance signals while MUA is used to generate charge signals, similar to the previous study. The charge signals increase with increasing sensing area size and plateau in a similar manner as the gain, while the capacitive signals peak for sensing area capacitances close to the channel capacitance and decrease for both larger and smaller sensing areas. The model is found to predict these outputs accurately except at sensing area capacitances lower than the channel capacitance, which is attributed to capacitance increases at lower sensing areas due to increased potential drops at the sensing surface.

The model predictions are then plotted for different values of V_0 to provide insights about the influence of material properties and operating conditions on the sensing capabilities of the device. It is reinforced that higher mobility semiconductors and high specific capacitance dielectrics are preferred for sensing applications, and it is found that higher supply voltages and load resistances provide increased amplification for the device. The control gate of the device and the floating gate pad connected to the channel by the dielectric (called FG1 in our notation) should be kept as large as possible for both charge and capacitance sensing. For charge sensing, the larger sensing areas are preferred, while capacitance sensing is optimized at sensing area capacitances close to the channel capacitance. The final study provides concrete and simple design rules for floating gate transistors regardless of materials choice that can enable widespread use of this platform for a large range of targets.

Overall, this work elucidated the sensing mechanisms of a promising transistor-based chemical sensing platform, the FGT, with the use of SAMs, quantifying its response to charge-based inputs and demonstrating its utility for quasi-static capacitance detection.

A model was produced to describe its behavior and was found to match experiments for a range of sensing area sizes. The understanding of the device operation and sensing mechanisms further allows the formulation of straightforward design principles generalizable to various floating gate devices under investigation (not just EGTs). This work provides quantitative understanding and mechanistic optimization of floating gate transistors which are promising candidates for use as rapid, sensitive, general purpose and easily fabricated chemical sensing devices for portable and distributed applications.

6.2 Future Perspectives – Microfluidic Optimization

The focus of this work has been the understanding and optimization of the platform from an electronics and transduction perspective. Further optimization of the sample delivery is hence a natural avenue for future work. The pads (other than source and drain), have all been kept square. The aspect ratio of the sensing area and the dimensions of the microfluidic channel can be optimized for faster sample delivery and lower detection times. An example calculation to estimate the magnitude of detection time changes with examples of changes is shown here, following nomenclature from a comprehensive analysis in Squires *et al.*[121]

In the FGT device, we assume the sensing area (FG2) has a length L along the direction of flow, and width W. A fluid delivery channel of height H and width $W_{channel}$ encompasses FG2. The target molecule in the fluid is at a uniform bulk concentration of C_0, and the average fluid velocity in the channel is U. The capture molecule is bound to FG2 at a surface density of s, assuming each molecule acts a single receptor for the target. From device and operation details provided for the detection of ricin by the FGT platform,[82]

we can obtain the values of these variables as $W_{channel}$ = 600 μm and H = 100 μm. Further, Q = 10 μL/min = $1.67x10^{-10}$ m^3/s, diffusivity D = ~10^{-10} m^2/s (for the ricin B chain or a similar sized protein in aqueous media – with M_W ~ 30 kg/mol), U = $Q/HW_{channel}$ = $2.80x10^{-3}$ m/s. So, we can calculate the Peclet number (ratio of convective to diffusive mass transfer rate) with respect to channel height $Pe_H = Q/DW_{channel}$ = 278, the shear Peclet number $Pe_S = 6\lambda^2 Pe_H$ = 375003 and λ = L/H = (1.5/0.1 mm) = 15. For Pe_H and Pe_S >> 1 and a very thin depletion region, the diffusive flux F in the depletion region ≈ $0.81Pe_S^{1/3}$ + $0.71Pe_S^{-1/6}$ – $0.2Pe_S^{-1/3}$ = 58.

We can now examine the effect of a simple decrease in $W_{channel}$ from 600 μm to 300 μm, for example. This change in value is chosen so it allows the sensing area to be kept of similar size, while still allowing for manual alignment of the microfluidics with the gold pads. The FG2 pad itself will have to be elongated to keep its area the same, assuming that optimum area has been determined from design principles in Chapter 5. For the new device, L = 3 mm, and W = 0.25 mm. Using a maximum aspect ratio of 10 for $W_{channel}/H$ for microfluidic devices, the channel height can go as low as 30 μm, and keeping other device dimensions and flowrate constant, we get Pe_H = 556, λ = L/H = (3/0.03 mm) = 100, Pe_S = $3.33x10^7$. F ≈ 261 for these new dimensions.

This simple calculation implies the flux increases by 4.6 times when these dimension changes are implemented. It is worth noting that if manual alignment is utilized, it will need to be quite precise, with only 50 μm difference in widths between the FG2 pad and the microfluidics.

Assuming the transduction of the binding event by the transistor is near instantaneous, the observed detection time can be treated as the total time from when the target has travelled through the microfluidic channel by convection, reached the surface by diffusion, has bound to the aptamer/antibody, and is in equilibrium.

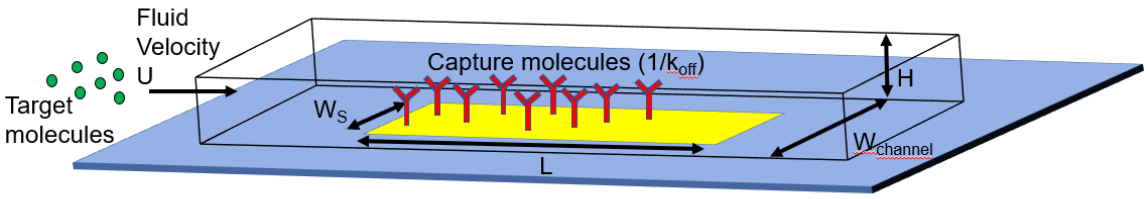

Fig 6.1. Microfluidic channel.[121] Schematic of a microfluidic channel encompassing a sensor pad (FG2 for the FGT) with the sample fluid bringing target molecules that can bind to the capture molecules at the surface. The figure is not to scale, and it is adapted from Squires *et al.*[121]

For the diffusion limited case, this time can be approximated by the residence time in the depletion region $\tau_D \approx \frac{k_{on}sL}{DF(k_{off}+k_{on}c_0)} = Da\tau_R$, where k_{on} and k_{off} refer to the rate constants for binding and removal of the target to the capture agent, c_0 is the bulk concentration of target, s is the density of capture molecules (or binding sites, more generally) on the surface, Da is the Damkohler number (the ratio of mass transfer or diffusion time to the reaction/binding time), and τ_R is the characteristic reaction time, roughly equal to $1/k_{off}$.

For Da>>1, (diffusion limited case) the formula above holds, otherwise, $\tau_D \approx \tau_R$, for the reaction limited case. The goal using the microfluidics is to ensure that the process is as free of mass transfer limitations as possible. The equilibrium time, and hence the

detection time, will reduce by 4.6 with the implementation of the new design if the process is mass transfer limited. The diffusion limited case is likely only true for lower concentrations, as high concentrations will probably ensure that the process is in the reaction limited regime. For ricin and other similar-sized proteins, it is possible that detecting concentrations near the LOD will be mass transfer limited even with high fluxes, as low c_0 will ensure that the Damkohler number Da, and hence the equilibrium time will always be very high. This is where the device improvements should most prominently enhance detection times.

Table 6.1 Detection times for new microfluidic designs. Calculated detection time scales for ricin with the Squires model[121] and previously reported device designs are shown here, assuming a mass transfer limited surface binding process in all cases. A pre-factor of 1/3 yields results similar to those observed in previous work.[82] Additionally, estimated times for a new single and multiple channel design are shown as well.

c_0 (g/ml)	Detection Time DT (min)	DT – 1/3 prefactor (min)	DT – New Single Channel (min)	DT – Multiple Channels (min)
1.00^{-9}	169.91	56.64	38.13	2.55
1.00^{-8}	161.26	53.75	36.18	2.40
1.00^{-7}	106.83	35.61	23.97	1.59
1.00^{-6}	24.42	8.14	5.49	0.36
1.00^{-5}	2.80	0.93	0.63	0.03

For this new design, the characteristic residence time in the depletion zone $\tau_\delta \sim \delta^2/D = (Pe_s^{-1/3}L)^2/D = 1.45$ min > 0.63 min (the lowest detection time), while it is smaller than detection times for lower concentrations, as listed in Table 6.1. This implies that for

high concentrations the model prediction may not be valid as the quasi-steady state approximation is not accurate anymore. The depletion zone takes a longer time to form than the predicted 'steady' time for equilibrium.

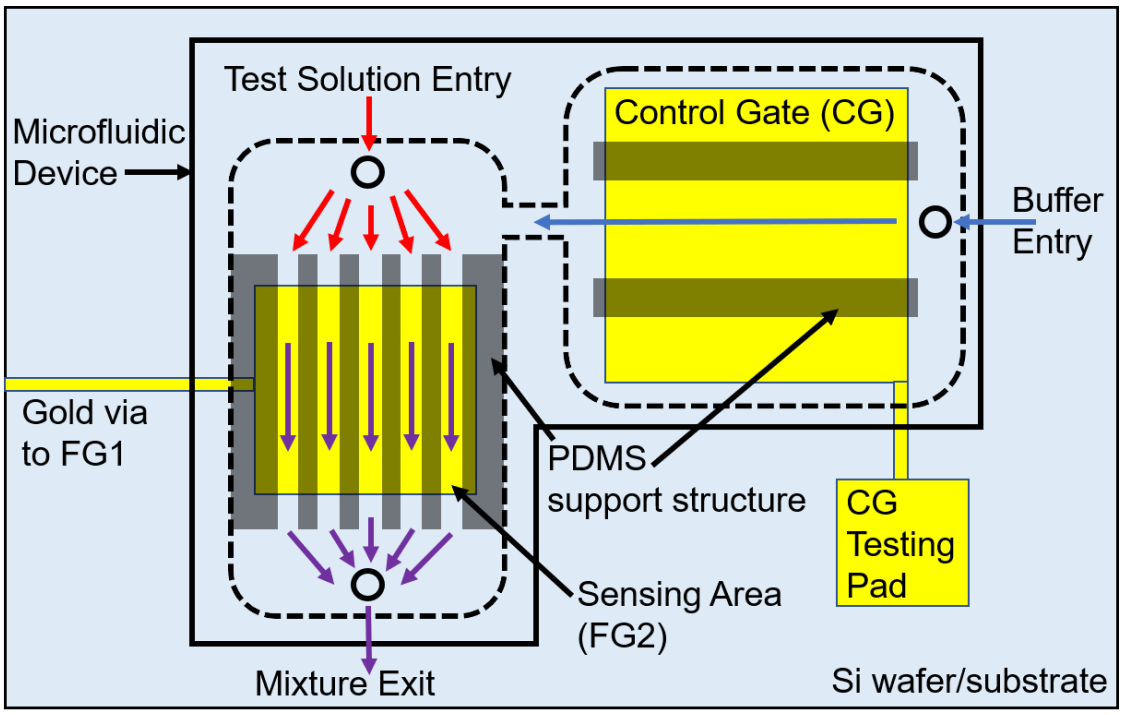

Fig 6.2. 5-Channel design. A possible design for a 5-channel microfluidic device is shown here. The sample or test solution mixes with a control buffer solution that enables electrolyte connection between CG and FG2. The resulting mixture is split between 5 channels which creates higher fluid velocities and better mass transfer to the sensor surface. Each channel Support structures within the device enable better mechanical robustness. The figure is not to scale.

Another possible design is to have 5 (as an example) parallel channels of 10 μm width with 50 μm wide PDMS (as an example) between each of them for support, as shown in Fig 6.2. Each channel hence has $W_{channel}$ = 10 μm and H = 2 μm for this design. For the

flow rate $Q = 3.33x10^{-11}$ m^3/s, we get $Pe_H = Q/DW_{channel} = 3.33x10^4$, $Pe_S = 6\lambda^2 Pe_H = 1.13x10^{11}$ and $\lambda = L/H = (1.5/0.002 \text{ mm}) = 750$. For Pe_H and $Pe_S >> 1$, with a very thin depletion region, flux F in the depletion region $\approx 0.81Pe_S^{1/3} + 0.71Pe_S^{-1/6} - 0.2Pe_S^{-1/3} = 3910$. This implies one would get a 67x increase in the flux, and corresponding reduction in the equilibrium time compared to the current design.

Some other engineering issues with this design and consequently some possible solutions for them are listed here:

1. Nonspecific adsorption to PDMS due to high surface area – the use of a blocking agent such as BSA may be required.
2. Reduction of FG2 area by about 5-6 times due to PDMS support structures – this can be compensated by increasing the sensing pad area appropriately.
3. Tougher to fabricate – multi level channels are required (this may be the case for the single channel design too).
4. Buffer solution contact with the sample solution could be an issue – gaps between PDMS support structures would be needed.
5. Increased pressure and resistance may cause containment issues and may require readjustment of flow rates.

For the multiple channel design, $\tau_\delta \sim \delta^2/D = (Pe_s^{-1/3}L)^2/D = 0.097 \text{ s} > 0.01 \text{ s}$. Similar to the earlier design, for high concentrations the model prediction may not be valid as the quasi-steady state approximation does not hold.

Table 6.1 shows that one could cut down on detection time significantly by changing the microfluidic design, especially for lower concentrations close to the limit of

detection. There could be additional differences from this prediction in the actual experiment due to non-uniform surface coverage, extremely high local velocities and possible manual alignment errors. A suitable set of target and capture molecules with well-established binding kinetics such as biotin and streptavidin[122,123] must be chosen for this testing, that allow a clear demonstration of the improvements provided by changes in microfluidic design. The pH sensing experiments described in Chapter 3 cannot be utilized effectively here as the diffusivity of protons in water is much higher than that of proteins or even small molecule targets.[124,125] Both optimal and sub-optimal microfluidic designs would hence result in binding/reaction limited processes and the experiments would be unable to distinguish between them. These are merely two examples of microfluidic designs for improved sensing in FGT devices, with many other possible designs such as herringbone structures for mixing.[126] or parallel devices for multiplexing.[127]

6.3 Silicon transistors, surface quality control, and pressure sensing

The focus of this work has been to understand and optimize or enhance the signal produced by the printed FGT device. Strategies to reduce device-to-device variation while maintaining the enhanced signals in the device must be a primary focus of work going forward. The current performance of the device is adequate for Yes-or-No or even more quantitative tests for many targets and sensing media of relevance to food safety[82,85] and environmental quality control applications.[128] Reduction of device-to-device variation will enable further reduction in limits of detection that can allow the FGT device to be used to quantify targets in bodily fluids and make the device competitive for biomedical and

possibly wearable applications – although many engineering solutions may be needed for eventual commercialization.

The work so far has imposed a constraint of utilizing printing to create the transistor device in order fully explore the capabilities of printed electronics in the chemical sensing space and to keep it compatible with roll-to-roll manufacturing in the future. However, it is possible that variation in printed semiconductor film thickness and morphology or change of threshold voltages due to material degradation or air doping of the organic semiconductor film causes device-to-device variation in the device response, increasing the standard deviation of the signal when measured over several hours. While this is not as much of an issue in the controlled, relatively fast (<20 min) and simple experiments carried out in this research, it can create issues for more complex sensing experiments, especially for biological targets, which often need long surface preparation times (>24 hours) and multiple functionalization steps. One strategy to avoid this variation could be to utilize a commercial silicon transistor, separately attached to a sensing surface (created in-house on Si/SiO_2 wafers) with a wire (thus 'extending' the gate) and compare the performance with previous results (for printed FGTs) for a molecule such as ricin or gluten.[81,85]

Another major source of variation could be the device-to-device density variation of probes or capture molecules. Characterization of complex sensing surfaces with methods such as X-ray Photoelectron Spectroscopy (XPS)/Angle-resolved X-ray Photoelectron Spectroscopy (ARXPS)[129] or optical microscopy before signal measurement can help in the removal of devices with lower probe density, and result in smaller measured signal variation (and perhaps smaller overall device yield as well). This is helpful for biosensing

applications (with more complex surfaces than the SAM-only surfaces utilized here) – where multiple steps may be required to attach capture molecules such as antibodies. However, the addition of microfluidic structures on the sensing surface for functionalization solution delivery can make this step difficult. One option to overcome this limitation is to utilize glass wafers for possible optical characterization from the other side with microscopy. A post–sensing characterization can also be utilized to confirm the probe density for complicated interfaces with capture molecules.

A more long-term research direction for the device could be to create a parallel combination of the FGT device with an optical sensing or characterization module. The FGT can detect the quantity of the target, and a surface-based optical detection method such as SERS (Surface Enhanced Raman Spectroscopy)[130] can be utilized for secondary quantification or confirmation of the target's chemical character.[131] This would enable the combined device to detect both larger biomolecules, which may not be well identified with SERS, due to sizes beyond the range of the surface plasmon-based signal enhancement/transduction,[130] as well as small and neutral molecules, which can be hard for the FGT device to quantify.[115] Microfluidic channels and flow splitters can be utilized to transport the solution to both surfaces simultaneously. The inherent bulkiness and complexity of the resulting device or the addition of extra characterization steps (described in the previous paragraph) could both restrict its use for only lab-based analytical tests.

Finally, a completely novel avenue for the FGT device would be the detection of fundamentally different physical quantities such as pressure or strain. Ferroelectric polymers such as PVDF-TrFE[132] can be printed on FG2 (the sensing area) for the

transduction of pressure by the FGT device. The floating gate can enable the use of semiconductor and dielectric materials with different mechanical properties than the pressure transducing element. A pressure sensing pad would hence consist of a floating gate with multiple FG2 pads and a single FG1 pad connected to a printed transistor, all on a flexible substrate. The deposition of printed films for PVDF[133] with techniques such as inkjet or aerosol jet printing can enable roll-to-roll manufacturing of large area pressure sensing pads which could be useful for health monitoring[134] or robotics applications.[135,136]

Bibliography

(1) Ahmed, A.; Rushworth, J. V.; Hirst, N. A.; Millner, P. A. Biosensors for Whole-Cell Bacterial Detection. *Clin. Microbiol. Rev.* **2014**, *27* (3), 631–646. https://doi.org/10.1128/CMR.00120-13.

(2) Turner, A. P. F. Biosensors: Sense and Sensibility. *Chem. Soc. Rev.* **2013**, *42* (8), 3184–3196. https://doi.org/10.1039/C3CS35528D.

(3) Nimse, S. B.; Sonawane, M. D.; Song, K. S.; Kim, T. Biomarker Detection Technologies and Future Directions. *Analyst* **2016**, *141* (3), 740–755. https://doi.org/10.1039/c5an01790d.

(4) Lazcka, O.; Campo, F. J. Del; Muñoz, F. X. Pathogen Detection: A Perspective of Traditional Methods and Biosensors. *Biosens. Bioelectron.* **2007**, *22* (7), 1205–1217. https://doi.org/10.1016/j.bios.2006.06.036.

(5) Alahi, M. E. E.; Mukhopadhyay, S. C. Detection Methodologies for Pathogen and Toxins: A Review. *Sensors (Switzerland)* **2017**, *17* (8), 1–20. https://doi.org/10.3390/s17081885.

(6) Neethirajan, S.; Weng, X.; Tah, A.; Cordero, J. O.; Ragavan, K. V. Nano-Biosensor Platforms for Detecting Food Allergens – New Trends. *Sens. Bio-Sensing Res.* **2018**, *18* (February), 13–30. https://doi.org/10.1016/j.sbsr.2018.02.005.

(7) Reverté, L.; Prieto-Simón, B.; Campàs, M. New Advances in Electrochemical Biosensors for the Detection of Toxins: Nanomaterials, Magnetic Beads and Microfluidics Systems. A Review. *Anal. Chim. Acta* **2016**, *908*, 8–21. https://doi.org/10.1016/j.aca.2015.11.050.

(8) Crowther, J. R. *The ELISA Guidebook*; 2001; Vol. 149. https://doi.org/10.1017/CBO9781107415324.004.

(9) Liu, Z.; Gurlo, T.; von Grafenstein, H. Cell-ELISA Using Beta-Galactosidase Conjugated Antibodies. *J. Immunol. Methods* **2000**, *234* (1–2), P153–P167. https://doi.org/10.1016/S0022-1759(99)00216-1.

(10) Albright, V. C.; Hellmich, R. L.; Coats, J. R. A Review of Cry Protein Detection with Enzyme-Linked Immunosorbent Assays. *J. Agric. Food Chem.* **2016**, *64* (11), 2175–2189. https://doi.org/10.1021/acs.jafc.5b03766.

(11) Westermeier, R.; Marouga, R. Protein Detection Methods in Proteomics Research. *Biosci. Rep.* **2005**, *25* (1–2), 19–32. https://doi.org/10.1007/s10540-005-2845-1.

(12) Jiang, L.; He, L.; Fountoulakis, M. Comparison of Protein Precipitation Methods for Sample Preparation Prior to Proteomic Analysis. *J. Chromatogr. A* **2004**, *1023* (2), 317–320. https://doi.org/10.1016/j.chroma.2003.10.029.

(13) Martinoia, S.; Rosso, N.; Grattarola, M.; Lorenzelli, L.; Margesin, B.; Zen, M. Development of ISFET Array-Based Microsystems for Bioelectrochemical

Measurements of Cell Populations. *Biosens. Bioelectron.* **2001**, *16* (9–12), 1043–1050. https://doi.org/10.1016/S0956-5663(01)00202-0.

(14) van Teeffelen, S.; Shaevitz, J. W.; Gitai, Z. Image Analysis in Fluorescence Microscopy: Bacterial Dynamics as a Case Study. *BioEssays* **2012**, *34* (5), 427–436. https://doi.org/10.1002/bies.201100148.

(15) Bej, A. K.; Mahbubani, M. H.; Dicesare, J. L.; Atlas, R. M. Polymerase Chain Reaction-Gene Probe Detection of Microorganisms by Using Filter-Concentrated Samples. *Appl. Environ. Microbiol.* **1991**, *57* (12), 3529–3534.

(16) Tsai, Y.; Palmer, C. J.; Sangermano, L. R. Detection of Escherichia Coli in Sewage and Sludge by Polymerase Chain Reaction. *Appl. Environ. Microbiol.* **1993**, *59* (2), 353–357.

(17) Lee, Y. J.; Han, S. R.; Maeng, J. S.; Cho, Y. J.; Lee, S. W. In Vitro Selection of Escherichia Coli O157:H7-Specific RNA Aptamer. *Biochem. Biophys. Res. Commun.* **2012**, *417* (1), 414–420. https://doi.org/10.1016/j.bbrc.2011.11.130.

(18) Glish, G. L.; Vachet, R. W. The Basics of Mass Spectrometry in the Twenty-First Century. *Nat. Rev. Drug Discov.* **2003**, *2* (2), 140–150. https://doi.org/10.1038/nrd1011.

(19) Han, X.; Aslanian, A.; Yates III, J. R. Mass Spectrometry for Proteomics. *Proteomics* **2001**, *12* (5), 483–490. https://doi.org/10.1016/j.cbpa.2008.07.024.Mass.

(20) Xiao, Y.; Isaacs, S. N. Enzyme-Linked Immunosorbent Assay (ELISA) and Blocking with Bovine Serum Albumin (BSA)-Not All BSAs Are Alike. *J. Immunol. Methods* **2012**, *384* (1–2), 148–151. https://doi.org/10.1016/j.jim.2012.06.009.

(21) Frankfurt, O. S.; Krishan, A. Enzyme-Linked Immunosorbent Assay (ELISA) for the Specific Detection of Apoptotic Cells and Its Application to Rapid Drug Screening. *J. Immunol. Methods* **2001**, *253*, 133–144. https://doi.org/10.1016/S0022-1759(01)00387-8.

(22) Hornbeck, P.; Winston, S. E.; Fuller, S. a. Enzyme-Linked Immunosorbent Assays (ELISA). *Curr. Protoc. Mol. Biol.* **2001**, *Chapter 11* (1991), Unit11.2. https://doi.org/10.1002/0471142727.mb1102s15.

(23) Liedberg, B.; Nylander, C.; Lunström, I. Surface Plasmon Resonance for Gas Detection and Biosensing. *Sensors and Actuators* **1983**, *4* (C), 299–304. https://doi.org/10.1016/0250-6874(83)85036-7.

(24) Clark, L. C.; Lyons, C. Electrode Systems for Continuous Monitoring in Cardiovascular Surgery. *Ann. N. Y. Acad. Sci.* **1962**, *102* (1), 29–45. https://doi.org/10.1111/j.1749-6632.1962.tb13623.x.

(25) Newman, J. D.; Turner, A. P. F. Home Blood Glucose Biosensors: A Commercial Perspective. *Biosens. Bioelectron.* **2005**, *20* (12), 2435–2453. https://doi.org/10.1016/j.bios.2004.11.012.

(26) Thévenot, D. R.; Toth, K.; Durst, R. A.; Wilson, G. S. ELECTROCHEMICAL BIOSENSORS: RECOMMENDED DEFINITIONS AND CLASSIFICATION *. *Anal. Lett.* **2001**, *34* (5), 635–659. https://doi.org/10.1081/AL-100103209.

(27) Dulay, S. B.; Gransee, R.; Julich, S.; Tomaso, H.; O'Sullivan, C. K. Automated Microfluidically Controlled Electrochemical Biosensor for the Rapid and Highly Sensitive Detection of Francisella Tularensis. *Biosens. Bioelectron.* **2014**, *59*, 342–349. https://doi.org/10.1016/j.bios.2014.03.024.

(28) Kim, S.-E.; Su, W.; Cho, M.; Lee, Y.; Choe, W.-S. Harnessing Aptamers for Electrochemical Detection of Endotoxin. *Anal. Biochem.* **2012**, *424* (1), 12–20. https://doi.org/http://dx.doi.org/10.1016/j.ab.2012.02.016.

(29) Zayats, M.; Huang, Y.; Gill, R.; Ma, C. A.; Willner, I. Label-Free and Reagentless Aptamer-Based Sensors for Small Molecules. *J. Am. Chem. Soc.* **2006**, *128* (42), 13666–13667. https://doi.org/10.1021/ja0651456.

(30) Newman, C. R.; Frisbie, D.; Da, D. A.; Filho, S.; Brédas, J.-L.; Ewbank, P. C.; Mann, K. R. Introduction to Organic Thin Film Transistors and Design of N-Channel Organic Semiconductors. *Chem. Mater.* **2004**, *16*, 2236–4451. https://doi.org/10.1021/cm049391x.

(31) Liao, C.; Yan, F. Organic Semiconductors in Organic Thin-Film Transistor-Based Chemical and Biological Sensors. *Polym. Rev.* **2013**, *53* (3), 352–406. https://doi.org/10.1080/15583724.2013.808665.

(32) Bergveld, P. Development of an Ion-Sensitive Solid-State Device for Neurophysiological Measurements. *IEEE Trans. Biomed. Eng.* **1970**, *BME-17* (1), 70–71. https://doi.org/10.1109/TBME.1970.4502688.

(33) Schöning, M. J.; Poghossian, A. Recent Advances in Biologically Sensitive Field-Effect Transistors (BioFETs). *Analyst* **2002**, *127* (9), 1137–1151. https://doi.org/10.1039/b204444g.

(34) Bergveld, P. Thirty Years of ISFETOLOGY. *Sensors Actuators B Chem.* **2002**, *88* (1), 1–20. https://doi.org/10.1016/s0925-4005(02)00301-5.

(35) Guan, W.; Duan, X.; Reed, M. A. Highly Specific and Sensitive Non-Enzymatic Determination of Uric Acid in Serum and Urine by Extended Gate Field Effect Transistor Sensors. *Biosens. Bioelectron.* **2014**, *51*, 225–231. https://doi.org/10.1016/j.bios.2013.07.061.

(36) Zafar, S.; Lu, M.; Jagtiani, A. Comparison between Field Effect Transistors and Bipolar Junction Transistors as Transducers in Electrochemical Sensors. *Sci. Rep.* **2017**, *7* (September 2016), 1–10. https://doi.org/10.1038/srep41430.

(37) Lee, J.; Dak, P.; Lee, Y.; Park, H.; Choi, W.; Alam, M. A.; Kim, S. Two-Dimensional Layered MoS(2) Biosensors Enable Highly Sensitive Detection of Biomolecules. *Sci. Rep.* **2014**, *4*, 7352. https://doi.org/10.1038/srep07352.

(38) Kwon, J.; Lee, B. H.; Kim, S. Y.; Park, J. Y.; Bae, H.; Choi, Y. K.; Ahn, J. H.

Nanoscale FET-Based Transduction toward Sensitive Extended-Gate Biosensors. *ACS Sensors* **2019**, *4*, 1724–1729. https://doi.org/10.1021/acssensors.9b00731.

(39) Bandiello, E.; Sessolo, M.; Bolink, H. J. Aqueous Electrolyte-Gated ZnO Transistors for Environmental and Biological Sensing. *J. Mater. Chem. C* **2014**, *2* (48), 10277–10281. https://doi.org/10.1039/C4TC02075H.

(40) Souteyrand, E.; Cloarec, J. P.; Martin, J. R.; Wilson, C.; Lawrence, I.; Mikkelsen, S.; Lawrence, M. F. Direct Detection of the Hybridization of Synthetic Homo-Oligomer DNA Sequences by Field Effect. *J. Phys. Chem. B* **1997**, *101* (15), 2980–2985. https://doi.org/10.1021/jp963056h.

(41) Yang, W.; Hamers, R. J. Fabrication and Characterization of a Biologically Sensitive Field-Effect Transistor Using a Nanocrystalline Diamond Thin Film. *Appl. Phys. Lett.* **2004**, *85* (16), 3626–3628. https://doi.org/10.1063/1.1808885.

(42) Barbaro, A.; Colapicchioni, C.; Davini, E.; Mazzamurro, G.; Piotto, A.; Porcelli, F. CHEMFET Devices for Biomedical and Environmental Applications. *Adv. Mater.* **1992**, *4* (6), 402–408. https://doi.org/10.1002/adma.19920040605.

(43) Xiaojie Duan, Ruixuan Gao, Ping Xie, Tzahi Cohen-Karni, Quan Qing, H. S.; Choe, Bozhi Tian, Xiaocheng Jiang, and C. M. L. Intracellular Recordings of Action Potentials by an Extracellular Nanoscale Field-Effect Transistor. *Nat. Nanotechnol.* **2012**, *7* (3), 174–179. https://doi.org/10.1038/nnano.2011.223.Intracellular.

(44) Rajan, N. K.; Duan, X.; Reed, M. A. Performance Limitations for Nanowire/Nanoribbon Biosensors. *Wiley Interdiscip. Rev. Nanomedicine Nanobiotechnology* **2013**, *5* (6), 629–645. https://doi.org/10.1002/wnan.1235.

(45) Chen, M.-C.; Chen, H.-Y.; Lin, C.-Y.; Chien, C.-H.; Hsieh, T.-F.; Horng, J.-T.; Qiu, J.-T.; Huang, C.-C.; Ho, C.-H.; Yang, F.-L. A CMOS-Compatible Poly-Si Nanowire Device with Hybrid Sensor/Memory Characteristics for System-on-Chip Applications. *Sensors (Basel, Switzerland)*. 2012, pp 3952–3963. https://doi.org/10.3390/s120403952.

(46) Zelada-Guillen, G. A.; Riu, J.; Düzgün, A.; Rius, F. X. Immediate Detection of Living Bacteria at Ultralow Concentrations Using a Carbon Nanotube Based Potentiometrie Aptasensor. *Angew. Chemie - Int. Ed.* **2009**, *48* (40), 7334–7337. https://doi.org/10.1002/anie.200902090.

(47) Sang, S.; Wang, Y.; Feng, Q.; Wei, Y.; Ji, J.; Zhang, W. Progress of New Label-Free Techniques for Biosensors: A Review. *Crit. Rev. Biotechnol.* **2015**, *00* (00), 1–17. https://doi.org/10.3109/07388551.2014.991270.

(48) Poghossian, A.; Schçning, M. J. Label-Free Sensing of Biomolecules with Field-Effect Devices for Clinical Applications. **2014**, 1197–1213. https://doi.org/10.1002/elan.201400073.

(49) Grubisha, D. S.; Lipert, R. J.; Park, H. Y.; Driskell, J.; Porter, M. D. Femtomolar Detection of Prostate-Specific Antigen: An Immunoassay Based on Surface-

Enhanced Raman Scattering and Immunogold Labels. *Anal. Chem.* **2003**, *75* (21), 5936–5943. https://doi.org/10.1021/ac034356f.

(50) Shirakawa, H.; Louis, E. J.; MacDiarmid, A. G.; Chiang, C. K.; Heeger, A. J. Synthesis of Electrically Conducting Organic Polymers: Halogen Derivatives of Polyacetylene, (CH)X. *J. Chem. Soc. Chem. Commun.* **1977**, No. 16, 578–580. https://doi.org/10.1039/C39770000578.

(51) McGinness, J.; Corry, P.; Proctor, P. Amorphous Semiconductor Switching in Melanins. *Science (80-.).* **1974**, *183* (4127), 853–855. https://doi.org/10.1126/science.183.4127.853.

(52) Coropceanu, V.; Cornil, J.; Silva, D.; A, D.; Olivier, Y.; Silbey, R.; Bredas, J. L.; da Silva Filho, D. A.; Brédas, J.-L. J.-L.; Olivier, Y.; Silbey, R.; Brédas, J.-L. J.-L. Charge Transport in Organic Semiconductors. *Chem. Rev.* **2007**, *107* (4), 926–952. https://doi.org/10.1007/128_2011_218.

(53) Krebs, F. C. Polymer Solar Cell Modules Prepared Using Roll-to-Roll Methods: Knife-over-Edge Coating, Slot-Die Coating and Screen Printing. *Sol. Energy Mater. Sol. Cells* **2009**, *93* (4), 465–475. https://doi.org/10.1016/j.solmat.2008.12.012.

(54) Teichler, A.; Perelaer, J.; Schubert, U. S. Inkjet Printing of Organic Electronics – Comparison of Deposition Techniques and State-of-the-Art Developments. *J. Mater. Chem. C* **2013**, *1* (10), 1910. https://doi.org/10.1039/c2tc00255h.

(55) Cummins, G.; Desmulliez, M. P. Y. Inkjet Printing of Conductive Materials: A Review. *Circuit World* **2012**, *38* (4), 193–213. https://doi.org/10.1108/03056121211280413.

(56) Mahajan, A.; Frisbie, C. D.; Francis, L. F. Optimization of Aerosol Jet Printing for High Resolution, High Aspect Ratio Silver Lines. *ACS Appl. Mater. Interfaces* **2013**, *5* (11), 4856–4864. https://doi.org/10.1021/am400606y.

(57) Salomon, A.; Cahen, D.; Lindsay, S.; Tomfohr, J.; Engelkes, V. B.; Frisbie, C. D. Comparison of Electronic Transport Measurements on Organic Molecules. *Adv. Mater.* **2003**, *15* (22), 1881–1890. https://doi.org/10.1002/adma.200306091.

(58) Chang, J.; Ge, T.; Sanchez-Sinencio, E. Challenges of Printed Electronics on Flexible Substrates. *Midwest Symp. Circuits Syst.* **2012**, 582–585. https://doi.org/10.1109/MWSCAS.2012.6292087.

(59) Shim, N. Y.; Bernards, D. A.; Macaya, D. J.; DeFranco, J. A.; Nikolou, M.; Owens, R. M.; Malliaras, G. G. All-Plastic Electrochemical Transistor for Glucose Sensing Using a Ferrocene Mediator. *Sensors* **2009**, *9* (12), 9896–9902. https://doi.org/10.3390/s91209896.

(60) Zou, S. J.; Shen, Y.; Xie, F. M.; Chen, J. De; Li, Y. Q.; Tang, J. X. Recent Advances in Organic Light-Emitting Diodes: Toward Smart Lighting and Displays. *Mater. Chem. Front.* **2020**, *4* (3), 788–820. https://doi.org/10.1039/c9qm00716d.

(61) Günes, S.; Neugebauer, H.; Sariciftci, N. S. Conjugated Polymer-Based Organic

Solar Cells. *Chem. Rev.* **2007**, *107* (4), 1324–1338. https://doi.org/10.1021/cr050149z.

(62) Cantatore, E.; Geuns, T. C. T.; Gelinck, G. H.; Van Veenendaal, E.; Gruijthuijsen, A. F. A.; Schrijnemakers, L.; Drews, S.; De Leeuw, D. M. A 13.56-MHz RFID System Based on Organic Transponders. *IEEE J. Solid-State Circuits* **2007**, *42* (1), 84–92. https://doi.org/10.1109/JSSC.2006.886556.

(63) Kim, S. H.; Hong, K.; Xie, W.; Lee, K. H.; Zhang, S.; Lodge, T. P.; Frisbie, C. D. Electrolyte-Gated Transistors for Organic and Printed Electronics. *Adv. Mater.* **2013**, *25* (13), 1822–1846. https://doi.org/10.1002/adma.201202790.

(64) Cho, J. H.; Lee, J.; Xia, Y.; Kim, B.; He, Y.; Renn, M. J.; Lodge, T. P.; Daniel Frisbie, C. Printable Ion-Gel Gate Dielectrics for Low-Voltage Polymer Thin-Film Transistors on Plastic. *Nat. Mater.* **2008**, *7* (11), 900–906. https://doi.org/10.1038/nmat2291.

(65) Bard, A. J.; Faulkner, L. R. Electrochemical Methods: Fundamentals and Applications. **2000**, 87–136.

(66) Ha, M.; Seo, J. W. T.; Prabhumirashi, P. L.; Zhang, W.; Geier, M. L.; Renn, M. J.; Kim, C. H.; Hersam, M. C.; Frisbie, C. D. Aerosol Jet Printed, Low Voltage, Electrolyte Gated Carbon Nanotube Ring Oscillators with Sub-5 Ms Stage Delays. *Nano Lett.* **2013**, *13* (3), 954–960. https://doi.org/10.1021/nl3038773.

(67) Marques, G. C.; Von Seggern, F.; Dehm, S.; Breitung, B.; Hahn, H.; Dasgupta, S.; Tahoori, M. B.; Aghassi-Hagmann, J. Influence of Humidity on the Performance of Composite Polymer Electrolyte-Gated Field-Effect Transistors and Circuits. *IEEE Trans. Electron Devices* **2019**, *66* (5), 2202–2207. https://doi.org/10.1109/TED.2019.2903456.

(68) Lodge, T. P.; Ueki, T. Mechanically Tunable, Readily Processable Ion Gels by Self-Assembly of Block Copolymers in Ionic Liquids. *Acc. Chem. Res.* **2016**, *49* (10), 2107–2114. https://doi.org/10.1021/acs.accounts.6b00308.

(69) Hashmi, S. A.; Latham, R. J.; Linford, R. G.; Schlindwein, W. S. Polymer Electrolyte Based Solid State Redox Supercapacitors with Poly (3-Methyl Thiophene) and Polypyrrole Conducting Polymer Electrodes. *Ionics (Kiel).* **1997**, *3* (3–4), 177–183. https://doi.org/10.1007/BF02375614.

(70) Lei, Z.; Chen, B.; Koo, Y. M.; Macfarlane, D. R. Introduction: Ionic Liquids. *Chem. Rev.* **2017**, *117* (10), 6633–6635. https://doi.org/10.1021/acs.chemrev.7b00246.

(71) Xie, W.; Frisbie, C. D. Organic Electrical Double Layer Transistors Based on Rubrene Single Crystals: Examining Transport at High Surface Charge Densities above 10 13 Cm –2. *J. Phys. Chem. C* **2011**, *115* (29), 14360–14368. https://doi.org/10.1021/jp204152y.

(72) Sailapu, S. K.; Macchia, E.; Merino-Jimenez, I.; Esquivel, J. P.; Sarcina, L.; Scamarcio, G.; Minteer, S. D.; Torsi, L.; Sabaté, N. Standalone Operation of an

EGOFET for Ultra-Sensitive Detection of HIV. *Biosens. Bioelectron.* **2020**, *156*, 112103. https://doi.org/https://doi.org/10.1016/j.bios.2020.112103.

(73) Batista, P. D.; Mulato, M. ZnO Extended-Gate Field-Effect Transistors as PH Sensors. *Appl. Phys. Lett.* **2005**, *87* (14), 1–3. https://doi.org/10.1063/1.2084319.

(74) Chen, J.; Chou, J.; Sun, T.; Hsiung, S. Portable Urea Biosensor Based on the Extended-Gate Field Effect Transistor. **2003**, *91*, 180–186. https://doi.org/10.1016/S0925-4005(03)00161-8.

(75) Pijanowska, D. G.; Torbicz, W. PH-ISFET Based Urea Biosensor. *Sensors Actuators, B Chem.* **1997**, *44* (1–3), 370–376. https://doi.org/10.1016/S0925-4005(97)00194-9.

(76) Minamiki, T.; Minami, T.; Sasaki, Y.; Wakida, S.; Kurita, R.; Niwa, O.; Tokito, S. Label-Free Detection of Human Glycoprotein (CgA) Using an Extended-Gated Organic Transistor-Based Immunosensor. *Sensors* . 2016. https://doi.org/10.3390/s16122033.

(77) Song, J.; Dailey, J.; Li, H.; Jang, H. J.; Zhang, P.; Wang, J. T. H.; Everett, A. D.; Katz, H. E. Extended Solution Gate OFET-Based Biosensor for Label-Free Glial Fibrillary Acidic Protein Detection with Polyethylene Glycol-Containing Bioreceptor Layer. *Adv. Funct. Mater.* **2017**, *27* (20). https://doi.org/10.1002/adfm.201606506.

(78) Chen, C. P.; Ganguly, A.; Lu, C. Y.; Chen, T. Y.; Kuo, C. C.; Chen, R. S.; Tu, W. H.; Fischer, W. B.; Chen, K. H.; Chen, L. C. Ultrasensitive in Situ Label-Free DNA Detection Using a GaN Nanowire-Based Extended-Gate Field-Effect-Transistor Sensor. *Anal. Chem.* **2011**, *83* (6), 1938–1943. https://doi.org/10.1021/ac102489y.

(79) Wang, L.; Estrela, P.; Huq, E.; Li, P.; Thomas, S.; Ferrigno, P. K.; Paul, D.; Adkin, P.; Migliorato, P. Fabrication of BioFET Linear Array for Detection of Protein Interactions. *Microelectron. Eng.* **2010**, *87* (5–8), 753–755. https://doi.org/10.1016/j.mee.2009.11.148.

(80) Cheng, S.; Hotani, K.; Hideshima, S.; Kuroiwa, S.; Nakanishi, T.; Hashimoto, M.; Mori, Y.; Osaka, T. Field Effect Transistor Biosensor Using Antigen Binding Fragment for Detecting Tumor Marker in Human Serum. *Materials (Basel).* **2014**, *7* (4), 2490–2500. https://doi.org/10.3390/ma7042490.

(81) White, S. P.; Dorfman, K. D.; Frisbie, C. D. Label-Free DNA Sensing Platform with Low-Voltage Electrolyte-Gated Transistors. *Anal. Chem.* **2015**, *87* (3), 1861–1866. https://doi.org/10.1021/ac503914x.

(82) White, S. P.; Sreevatsan, S.; Frisbie, C. D.; Dorfman, K. D. Rapid, Selective, Label-OrFree Aptameric Capture and Detection of Ricin in Potable Liquids Using a Printed Floating Gate Transistor. *ACS Sensors* **2016**, acssensors.6b00481. https://doi.org/10.1021/acssensors.6b00481.

(83) Lamont, E. A.; He, L.; Warriner, K.; Labuza, T. P.; Sreevatsan, S. A Single DNA

Aptamer Functions as a Biosensor for Ricin. *Analyst* **2011**, *136* (19), 3884–3895. https://doi.org/10.1039/C1AN15352H.

(84) Joshi, R.; Janagama, H.; Dwivedi, H. P.; Senthil Kumar, T. M. A.; Jaykus, L. A.; Schefers, J.; Sreevatsan, S. Selection, Characterization, and Application of DNA Aptamers for the Capture and Detection of Salmonella Enterica Serovars. *Mol. Cell. Probes* **2009**, *23* (1), 20–28. https://doi.org/10.1016/j.mcp.2008.10.006.

(85) White, S. P.; Frisbie, C. D.; Dorfman, K. D. Detection and Sourcing of Gluten in Grain with Multiple Floating-Gate Transistor Biosensors. *ACS Sensors* **2018**, *3* (2), 395–402. https://doi.org/10.1021/acssensors.7b00810.

(86) White, S. P.; Dorfman, K. D.; Frisbie, C. D. Operating and Sensing Mechanism of Electrolyte-Gated Transistors with Floating Gates: Building a Platform for Amplified Biodetection. *J. Phys. Chem. C* **2016**, *120* (1), 108–117. https://doi.org/10.1021/acs.jpcc.5b10694.

(87) Duong, D. T.; Ho, V.; Shang, Z.; Mollinger, S.; Mannsfeld, S. C. B.; Dacuña, J.; Toney, M. F.; Segalman, R.; Salleo, A. Mechanism of Crystallization and Implications for Charge Transport in Poly(3-Ethylhexylthiophene) Thin Films. *Adv. Funct. Mater.* **2014**, *24* (28), 4515–4521. https://doi.org/10.1002/adfm.201304247.

(88) Kim, S. H.; Hong, K.; Lee, K. H.; Frisbie, C. D. Performance and Stability of Aerosol-Jet-Printed Electrolyte-Gated Transistors Based on Poly(3-Hexylthiophene). *ACS Appl. Mater. Interfaces* **2013**, *5* (14), 6580–6585. https://doi.org/10.1021/am401200y.

(89) Tang, B.; White, S. P.; Frisbie, C. D.; Lodge, T. P. Synergistic Increase in Ionic Conductivity and Modulus of Triblock Copolymer Ion Gels. *Macromolecules* **2015**, *48* (14), 4942–4950. https://doi.org/10.1021/acs.macromol.5b00882.

(90) Vericat, C.; Vela, M. E.; Corthey, G.; Pensa, E.; Cortés, E.; Fonticelli, M. H.; Ibañez, F.; Benitez, G. E.; Carro, P.; Salvarezza, R. C. Self-Assembled Monolayers of Thiolates on Metals: A Review Article on Sulfur-Metal Chemistry and Surface Structures. *RSC Adv.* **2014**, *4* (53), 27730–27754. https://doi.org/10.1039/c4ra04659e.

(91) Miyahara, T. S. and S. M. and Y. N. and Y. Potential Behavior of Biochemically Modified Gold Electrode for Extended-Gate Field-Effect Transistor. *Jpn. J. Appl. Phys.* **2005**, *44* (4S), 2860.

(92) Gravesen, P.; Branebjerg, J.; Jensen, O. S. Microfluidics-a Review. *J. Micromechanics Microengineering* **1993**, *3* (4), 168.

(93) Gale, B. K.; Jafek, A. R.; Lambert, C. J.; Goenner, B. L.; Moghimifam, H.; Nze, U. C.; Kamarapu, S. K. A Review of Current Methods in Microfluidic Device Fabrication and Future Commercialization Prospects. *Inventions* **2018**, *3* (3). https://doi.org/10.3390/inventions3030060.

(94) Khan, S.; Lorenzelli, L.; Dahiya, R. S. Technologies for Printing Sensors and

Electronics over Large Flexible Substrates: A Review. *IEEE Sens. J.* **2015**, *15* (6), 3164–3185. https://doi.org/10.1109/JSEN.2014.2375203.

(95) Seethapathy, S.; Górecki, T. Applications of Polydimethylsiloxane in Analytical Chemistry: A Review. *Anal. Chim. Acta* **2012**, *750*, 48–62. https://doi.org/10.1016/j.aca.2012.05.004.

(96) Demissie, A. T.; Haugstad, G.; Frisbie, C. D. Growth of Thin, Anisotropic, π-Conjugated Molecular Films by Stepwise "Click" Assembly of Molecular Building Blocks: Characterizing Reaction Yield, Surface Coverage, and Film Thickness versus Addition Step Number. *J. Am. Chem. Soc.* **2015**, *137* (27), 8819–8828. https://doi.org/10.1021/jacs.5b04512.

(97) Demissie, A. T.; Haugstad, G.; Frisbie, C. D. Quantitative Surface Coverage Measurements of Self-Assembled Monolayers by Nuclear Reaction Analysis of Carbon-12. *J. Phys. Chem. Lett.* **2016**, *7* (17), 3477–3481. https://doi.org/10.1021/acs.jpclett.6b01363.

(98) Palazzo, G.; De Tullio, D.; Magliulo, M.; Mallardi, A.; Intranuovo, F.; Mulla, M. Y.; Favia, P.; Vikholm-Lundin, I.; Torsi, L. Detection beyond Debye's Length with an Electrolyte-Gated Organic Field-Effect Transistor. *Adv. Mater.* **2015**, *27* (5), 911–916. https://doi.org/10.1002/adma.201403541.

(99) Kakiuchi, T.; Iida, M.; Imabayashi, S.; Niki, K. Double-Layer-Capacitance Titration of Self-Assembled Monolayers of ω -Functionalized Alkanethiols on Au (111) Surface. *Langmuir* **2000**, No. 111, 5397–5401.

(100) Nelson, K. E.; Gamble, L.; Jung, L. S.; Boeckl, M. S.; Naeemi, E.; Golledge, S. L.; Sasaki, T.; Castner, D. G.; Campbell, C. T.; Stayton, P. S. Surface Characterization of Mixed Self-Assembled Monolayers Designed for Streptavidin Immobilization. *Langmuir* **2001**, *17* (9), 2807–2816. https://doi.org/10.1021/la001111e.

(101) Thomas, M. S.; White, S. P.; Dorfman, K. D.; Frisbie, C. D. Interfacial Charge Contributions to Chemical Sensing by Electrolyte-Gated Transistors with Floating Gates. *J. Phys. Chem. Lett.* **2018**, *9* (6), 1335–1339. https://doi.org/10.1021/acs.jpclett.8b00285.

(102) Fears, Kenan P., Creager, Stephen E. , Latour, R. A. Determination of the Surface PK of Carboxylic- and AmineTerminated Alkanethiols Using Surface Plasmon Resonance Spectroscopy. *Langmuir* **2008**, *24* (3), 837–843. https://doi.org/10.1021/la701760s.Determination.

(103) Bain, C. D.; Whitesides, G. M. A Study by Contact Angle of the Acid-Base Behavior of Monolayers Containing .Omega.-Mercaptocarboxylic Acids Adsorbed on Gold: An Example of Reactive Spreading. *Langmuir* **1989**, *5* (6), 1370–1378. https://doi.org/10.1021/la00090a019.

(104) Zhao, J.; Luo, L.; Yang, X.; Wang, E.; Dong, S. *Determination of Surface PKa of SAM Using an Electrochemical Titration Method*; 1999; Vol. 11. https://doi.org/10.1002/(SICI)1521-4109(199911)11:15<1108::AID-

ELAN1108>3.0.CO;2-Z.

(105) Zhang, B.; Wang, X.; Liu, F.; Cheng, Y.; Shi, D. Effective Reduction of Nonspecific Binding by Surface Engineering of Quantum Dots with Bovine Serum Albumin for Cell-Targeted Imaging. *Langmuir* **2012**, *28* (48), 16605–16613. https://doi.org/10.1021/la302758g.

(106) Xue, Y.; Li, X.; Li, H.; Zhang, W. Quantifying Thiol–Gold Interactions towards the Efficient Strength Control. **2014**, *5*, 4348.

(107) Sanders, W. C. Examining the Effects of Applied Potential on the Surface Charge of Functionalized Monolayers for Site-Directed Ionic Self Assembly, 2008.

(108) Ramírez, P.; Andreu, R.; Cuesta, Á.; Calzado, C. J.; Calvente, J. J. Determination of the Potential of Zero Charge of Au(111) Modified with Thiol Monolayers. *Anal. Chem.* **2007**, *79* (17), 6473–6479. https://doi.org/10.1021/ac071341z.

(109) Maduen, R.; Sevilla, J. M.; Bla, M.; Pineda, T. Formation of Mixed Monolayers from 11-Mercaptoundecanoic Acid and Octanethiol on Au(111) Single Crystal Electrode under Electrochemical Control. **2013**, No. 111. https://doi.org/10.1021/jp406229f.

(110) Bandodkar, A. J.; Wang, J. Non-Invasive Wearable Electrochemical Sensors: A Review. *Trends Biotechnol.* **2014**, *32* (7), 363–371. https://doi.org/10.1016/j.tibtech.2014.04.005.

(111) Bao, C.; Kaur, M.; Kim, W. S. Toward a Highly Selective Artificial Saliva Sensor Using Printed Hybrid Field Effect Transistors. *Sensors Actuators, B Chem.* **2019**, *285* (November 2018), 186–192. https://doi.org/10.1016/j.snb.2019.01.062.

(112) Kimura, J. A Novel Blood Glucose Monitoring Method an ISFET Biosensor Applied to Transcutaneous Effusion Fluid. *J. Electrochem. Soc.* **2006**, *136* (6), 1744. https://doi.org/10.1149/1.2097003.

(113) Zare Bidoky, F.; Frisbie, C. D. Parasitic Capacitance Effect on Dynamic Performance of Aerosol-Jet-Printed Sub 2 v Poly(3-Hexylthiophene) Electrolyte-Gated Transistors. *ACS Appl. Mater. Interfaces* **2016**, *8* (40), 27012–27017. https://doi.org/10.1021/acsami.6b08396.

(114) Zare Bidoky, F.; Tang, B.; Ma, R.; Jochem, K. S.; Hyun, W. J.; Song, D.; Koester, S. J.; Lodge, T. P.; Frisbie, C. D. Sub-3 V ZnO Electrolyte-Gated Transistors and Circuits with Screen-Printed and Photo-Crosslinked Ion Gel Gate Dielectrics: New Routes to Improved Performance. *Adv. Funct. Mater.* **2020**, *30* (20), 1–9. https://doi.org/10.1002/adfm.201902028.

(115) Thomas, M. S.; Dorfman, K. D.; Frisbie, C. D. Detection and Amplification of Capacitance- and Charge-Based Signals Using Printed Electrolyte Gated Transistors with Floating Gates. *Flex. Print. Electron.* **2019**, *4* (4), 44001. https://doi.org/10.1088/2058-8585/ab4dcf.

(116) Bisdounis, L.; Nikolaidis, S.; Koufopavlou, O.; Goutis, C. Switching Response

Modeling of the CMOS Inverter for Sub-Micron Devices. *Proc. -Design, Autom. Test Eur. DATE* **1998**, 729–735. https://doi.org/10.1109/DATE.1998.655939.

(117) Hong, K.; Kim, S. H.; Lee, K. H.; Frisbie, C. D. Printed, Sub-2V ZnO Electrolyte Gated Transistors and Inverters on Plastic. *Adv. Mater.* **2013**, *25* (25), 3413–3418. https://doi.org/10.1002/adma.201300211.

(118) Horányi, G.; Rizmayer, E. M.; Joó, P. Radiotracer Study of the Adsorption of Cl− and HSO4− Ions on a Porous Gold Electrode and on Underpotential Deposited Metals on Gold. *J. Electroanal. Chem. Interfacial Electrochem.* **1983**, *152* (1), 211–222. https://doi.org/https://doi.org/10.1016/S0022-0728(83)80045-X.

(119) Reid, J. E. S. J.; Walker, A. J.; Shimizu, S. Residual Water in Ionic Liquids: Clustered or Dissociated? *Phys. Chem. Chem. Phys.* **2015**, *17* (22), 14710–14718. https://doi.org/10.1039/c5cp01854d.

(120) Minami, T.; Sasaki, Y.; Minamiki, T.; Wakida, S. ichi; Kurita, R.; Niwa, O.; Tokito, S. Selective Nitrate Detection by an Enzymatic Sensor Based on an Extended-Gate Type Organic Field-Effect Transistor. *Biosens. Bioelectron.* **2016**, *81*, 87–91. https://doi.org/10.1016/j.bios.2016.02.036.

(121) Squires, T. M.; Messinger, R. J.; Manalis, S. R. Making It Stick: Convection, Reaction and Diffusion in Surface-Based Biosensors. *Nat. Biotechnol.* **2008**, *26*, 417.

(122) Piran, U.; Riordan, W. J. Dissociation Rate Constant of the Biotin-Streptavidin Complex. *J. Immunol. Methods* **1990**, *133* (1), 141–143. https://doi.org/10.1016/0022-1759(90)90328-S.

(123) Caswell, K. K.; Wilson, J. N.; Bunz, U. H. F.; Murphy, C. J. Preferential End-to-End Assembly of Gold Nanorods by Biotin-Streptavidin Connectors. *J. Am. Chem. Soc.* **2003**, *125* (46), 13914–13915. https://doi.org/10.1021/ja037969i.

(124) Boero, M.; Ikeshoji, T.; Terakura, K. Density and Temperature Dependence of Proton Diffusion in Water: A First-Principles Molecular Dynamics Study. *ChemPhysChem* **2005**, *6* (9), 1775–1779. https://doi.org/10.1002/cphc.200400572.

(125) Upadrashta, S. M.; Häglund, B. O.; Sundelöf, L. -O. Diffusion and Concentration Profiles of Drugs in Gels. *J. Pharm. Sci.* **1993**, *82* (11), 1094–1098. https://doi.org/10.1002/jps.2600821106.

(126) Dorfman, K. D.; Adrahtas, D. Z.; Thomas, M. S.; Frisbie, C. D. Microfluidic Opportunities in Printed Electrolyte-Gated Transistor Biosensors. *Biomicrofluidics* **2020**, *14* (1). https://doi.org/10.1063/1.5131365.

(127) Haeberle, S.; Zengerle, R. Microfluidic Platforms for Lab-on-a-Chip Applications. *Lab Chip* **2007**, *7* (9), 1094–1110. https://doi.org/10.1039/b706364b.

(128) Nerozzi, C.; Recuero, S.; Galeati, G.; Bucci, D.; Spinaci, M.; Yeste, M. Effects of Roundup and Its Main Component, Glyphosate, upon Mammalian Sperm Function and Survival. *Sci. Rep.* **2020**, *10* (1), 1–9. https://doi.org/10.1038/s41598-020-

67538-w.

(129) Aarnink, W. A. M. Angle-Resolved X-Ray Photoelectron Spectroscopy (ARXPS) and a Modified Levenberg-Marquardt Fit Procedure. *Appl. Surf. Sci.* **1990**, *45*, 37–48.

(130) Moskovits, M. Surface-Enhanced Raman Spectroscopy: A Brief Retrospective. *J. Raman Spectrosc.* **2005**, *36* (6–7), 485–496. https://doi.org/10.1002/jrs.1362.

(131) Szlag, V. M.; Rodriguez, R. S.; Jung, S.; Bourgeois, M. R.; Bryson, S.; Purchel, A.; Schatz, G. C.; Haynes, C. L.; Reineke, T. M. Optimizing Linear Polymer Affinity Agent Properties for Surface-Enhanced Raman Scattering Detection of Aflatoxin B1. *Mol. Syst. Des. Eng.* **2019**, *4* (5), 1019–1031. https://doi.org/10.1039/c9me00032a.

(132) Martins, P.; Lopes, A. C.; Lanceros-Mendez, S. Electroactive Phases of Poly(Vinylidene Fluoride): Determination, Processing and Applications. *Prog. Polym. Sci.* **2014**, *39* (4), 683–706. https://doi.org/10.1016/j.progpolymsci.2013.07.006.

(133) Stadlober, B.; Zirkl, M.; Irimia-Vladu, M. Route towards Sustainable Smart Sensors: Ferroelectric Polyvinylidene Fluoride-Based Materials and Their Integration in Flexible Electronics. *Chem. Soc. Rev.* **2019**, *48* (6), 1787–1825. https://doi.org/10.1039/c8cs00928g.

(134) Saenz-Cogollo, J. F.; Pau, M.; Fraboni, B.; Bonfiglio, A. Pressure Mapping Mat for Tele-Home Care Applications. *Sensors (Switzerland)* **2016**, *16* (3), 1–18. https://doi.org/10.3390/s16030365.

(135) Ang, B. W. K.; Yeow, C. H. Print-It-Yourself (PIY) Glove: A Fully 3D Printed Soft Robotic Hand Rehabilitative and Assistive Exoskeleton for Stroke Patients. *IEEE Int. Conf. Intell. Robot. Syst.* **2017**, *2017-Septe*, 1219–1223. https://doi.org/10.1109/IROS.2017.8202295.

(136) Yang, J. C.; Mun, J.; Kwon, S. Y.; Park, S.; Bao, Z.; Park, S. Electronic Skin : Recent Progress and Future Prospects for Skin-Attachable Devices for Health Monitoring , Robotics , and Prosthetics. **2019**, *1904765*, 1–50. https://doi.org/10.1002/adma.201904765.

(137) Yu, H.; Xia, N.; Liu, Z. SERS Titration of 4-Mercaptopyridine Self-Assembled Monolayers at Aqueous Buffer / Gold Interfaces. **2006**, *71* (7), 1354–1358.

(138) Borkovec, M. Origin of 1-PK and 2-PK Models for Ionizable Water−Solid Interfaces. *Langmuir* **1997**, *13* (10), 2608–2613. https://doi.org/10.1021/la9621325.

Appendix A – Charge Response

This appendix is for chapter 3 and includes titration curves for different electrolyte concentrations, the variation of pK_a with electrolyte concentration, an example NRA measurement for obtaining surface density of MUA, and example titration curves for 3-mercaptopropanoic acid and 4-aminothiphenol.

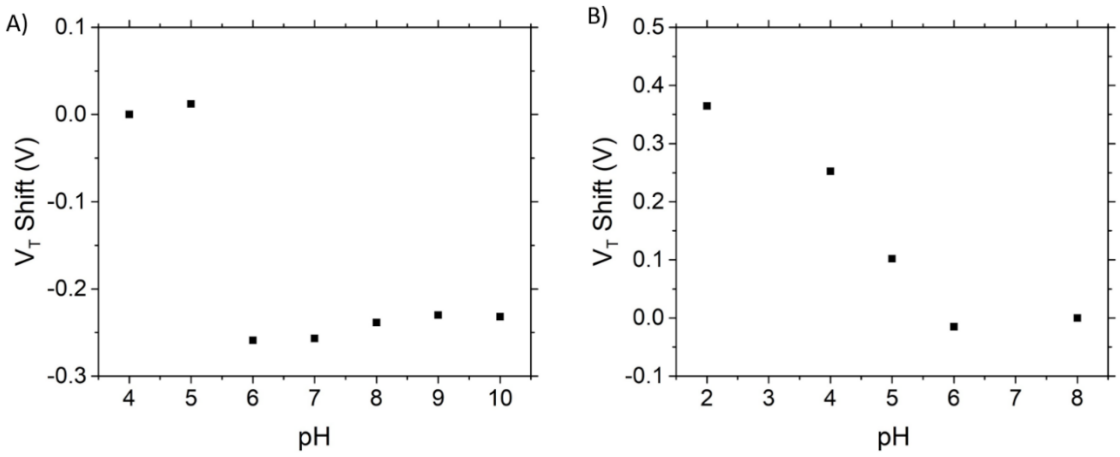

Figure A.1. Acid and Base Titrations.[101] (A) 3-mercaptopropionic acid (MPA) titration curve. (B) 4-mercaptopyridine (a base) titration curve. One device is shown for each case. Reprinted (adapted) with permission from Thomas, M.S., White, S.P., Dorfman, K.D., Frisbie, C.D.; Interfacial Charge Contributions to Chemical Sensing by Electrolyte Gated Transistors with Floating Gates, Journal of Physical Chemistry Letters (2018), 9(6), 1335-1339. Copyright 2018 American Chemical Society.

Since the claims made in the study are general in nature, it is prudent to test another acid-terminated molecule and a base-terminated one as well. Both trends are found to be the same, as the acid becomes negatively charged as pH is increased, and the base goes from positive to neutral. The reference curve for the base is taken to be the highest pH (8), as

this is where it is assumed to be uncharged. Both the acid and base $pK_{1/2}$ values are close to those reported in the literature.[104,137]

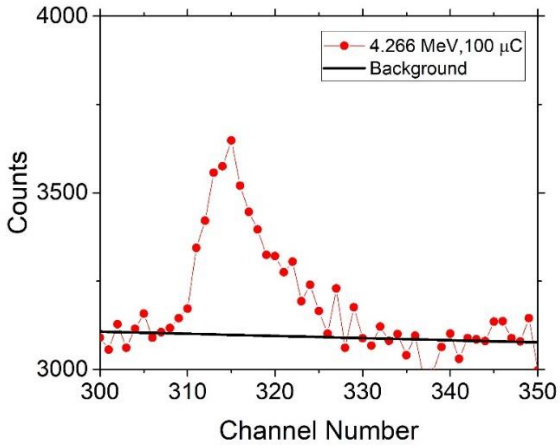

Fig A.2. Example NRA measurement.[101] The carbon signal peak for a MUA on gold/Si-SiO_2 wafer after 4 hours of functionalization. The beam energy is 4.266 MeV and the total charge is 100 μC. A linear fit is utilized to eliminate the background. Reprinted (adapted) with permission from Thomas, M.S., White, S.P., Dorfman, K.D., Frisbie, C.D.; Interfacial Charge Contributions to Chemical Sensing by Electrolyte Gated Transistors with Floating Gates, Journal of Physical Chemistry Letters (2018), 9(6), 1335-1339. Copyright 2018 American Chemical Society.

NRA (Nuclear reaction Analysis) is a variant of RBS (Rutherford Backscattering Spectrometry) utilized for the detection of light elements such as carbon. NRA experiments were conducted by Greg Haugstad, at the Characterization facility, University of Minnesota. The data analysis was conducted using previously reported methods.[97]

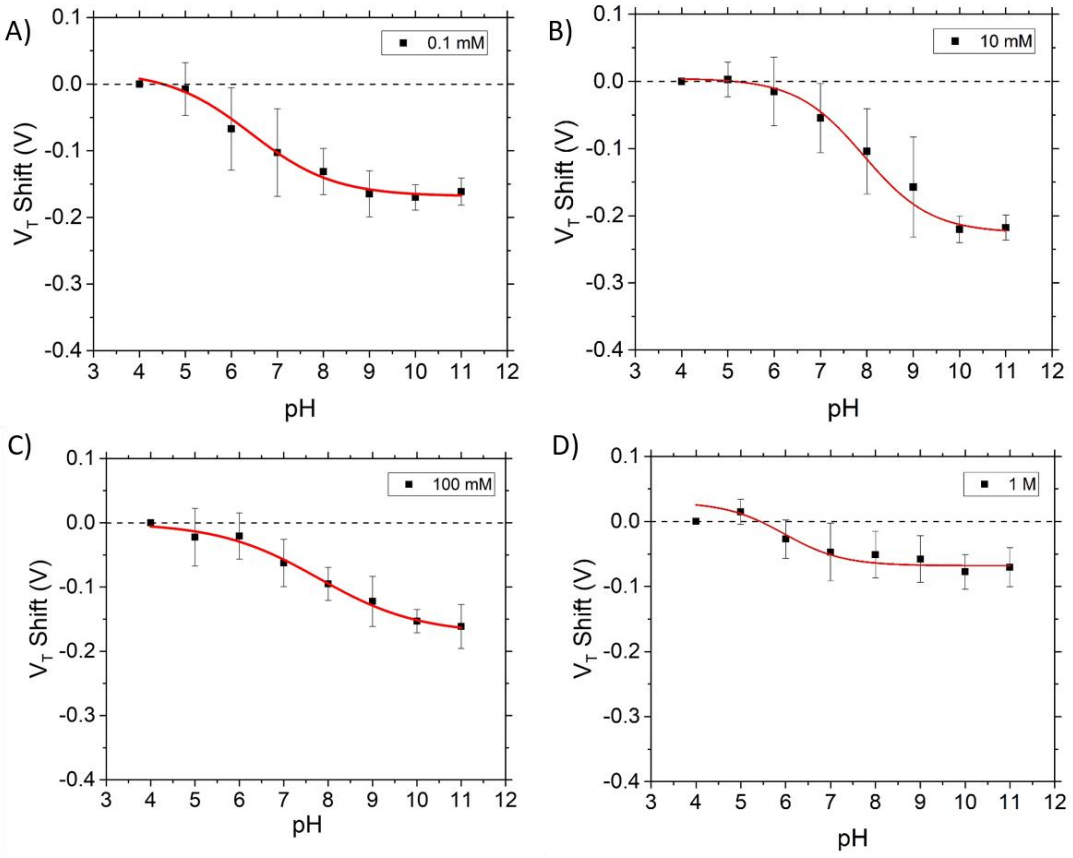

Fig A.3. Titration curves for different concentrations.[101] Titration curves for concentrations other than 1 mM. The maximum shift decreases from 10 mM to 1 M. The error bars represent 1 standard deviation for 5 devices each. The pK_a is calculated as the inflection point of the sigmoidal fit. Reprinted (adapted) with permission from Thomas, M.S., White, S.P., Dorfman, K.D., Frisbie, C.D.; Interfacial Charge Contributions to Chemical Sensing by Electrolyte Gated Transistors with Floating Gates, Journal of Physical Chemistry Letters (2018), 9(6), 1335-1339. Copyright 2018 American Chemical Society.

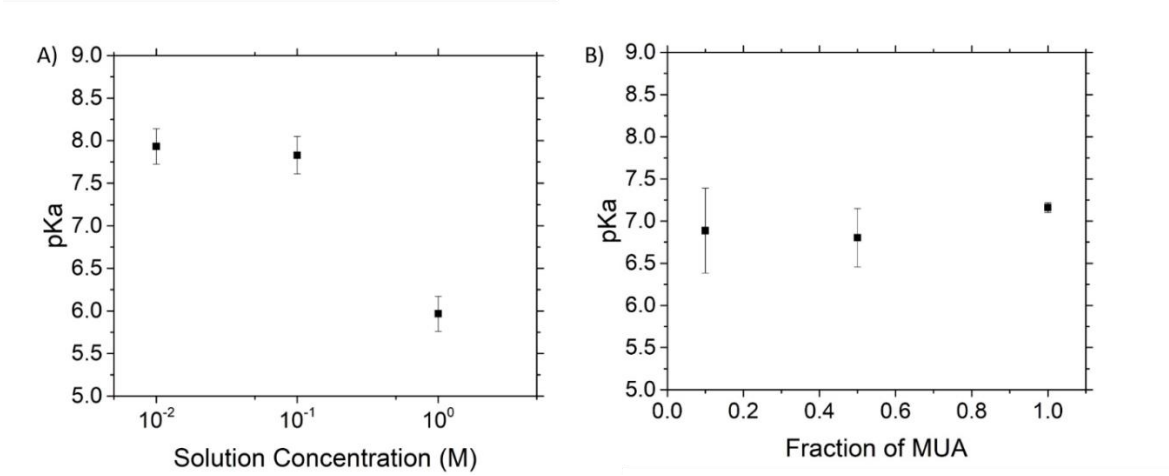

Fig A.4. pK_a trends.[101] (A) pK_a values extracted from sigmoidal fits for higher electrolyte concentrations. (B) pK_a values plotted against solution MUA fraction. Reprinted (adapted) with permission from Thomas, M.S., White, S.P., Dorfman, K.D., Frisbie, C.D.; Interfacial Charge Contributions to Chemical Sensing by Electrolyte Gated Transistors with Floating Gates, Journal of Physical Chemistry Letters (2018), 9(6), 1335-1339. Copyright 2018 American Chemical Society.

The findings from the experiments indicate that the pK_a of MUA decreases as the electrolyte concentration is increased. As the charges generated by deprotonation are screened more effectively, the deprotonated state becomes more energetically favorable, and the 1-pK model[138] for charged monolayers provides additional theoretical backing for this phenomenon. A similar argument can be made for decreasing surface charge density, as the repulsion felt by individual molecules with increasing deprotonation is reduced.[109]

Appendix B – Modeling and Optimization

Supporting information for chapter 5 is provided here. Signals calculated from the example devices in Fig 5.5 are shown below, along with theoretical counterparts. The peak heights are similar, but the shapes are different, especially for the capacitive signal.

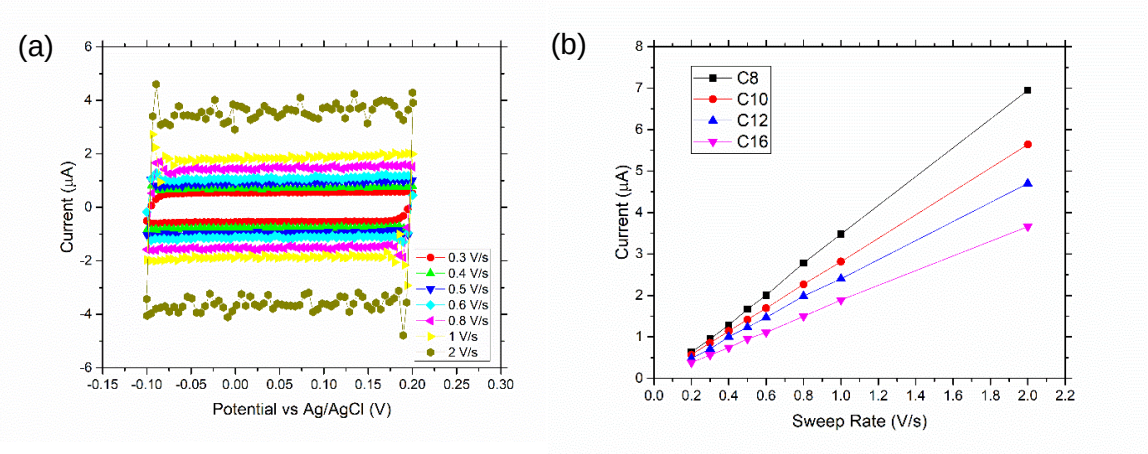

Fig B.1. Cyclic Voltammetry. (a) Example cyclic voltammetry measurements for a C16 monolayer on gold electrodes. A potentiostat swept working electrode potentials and recorded currents, with a platinum counter electrode and Ag/AgCl reference electrode immersed in a 0.1 M KCl solution. The voltage is swept at increasing rates vs Ag/AgCl with current measurement at each sweep rate. (b) Average plateau current vs Sweep rate plots yield linear relationships, and the slopes are used to calculate the capacitance of C8-C16 monolayers.

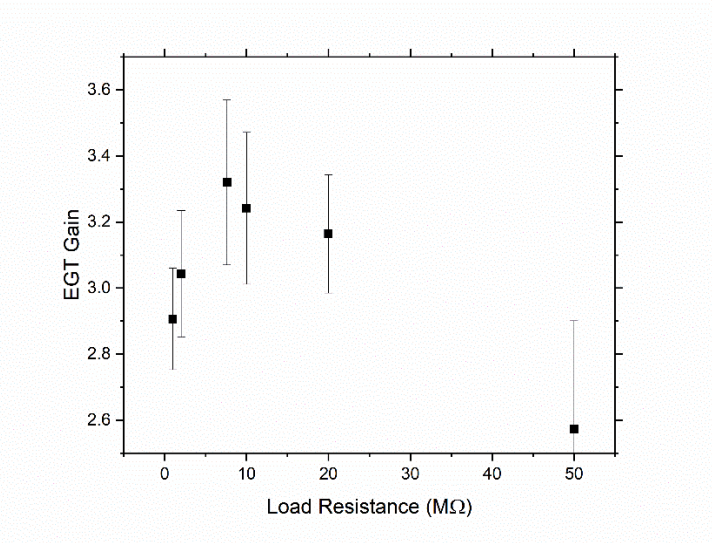

Fig B.2. Gain vs Load resistance. The gain measured for a set of EGT devices just after printing, with C_1 = 7 nF, and C_0 = 28 nF is plotted against different values of the load resistance. It increases until 10 MΩ, after which it decreases, as the current is not able to increase to change the potential drop as the resistance is too high. The data show large variation between devices, possibly due to poor connections made by replacing R_L frequently in the circuit. The data points represent the mean and standard deviation of at least 3 separate devices at each point.

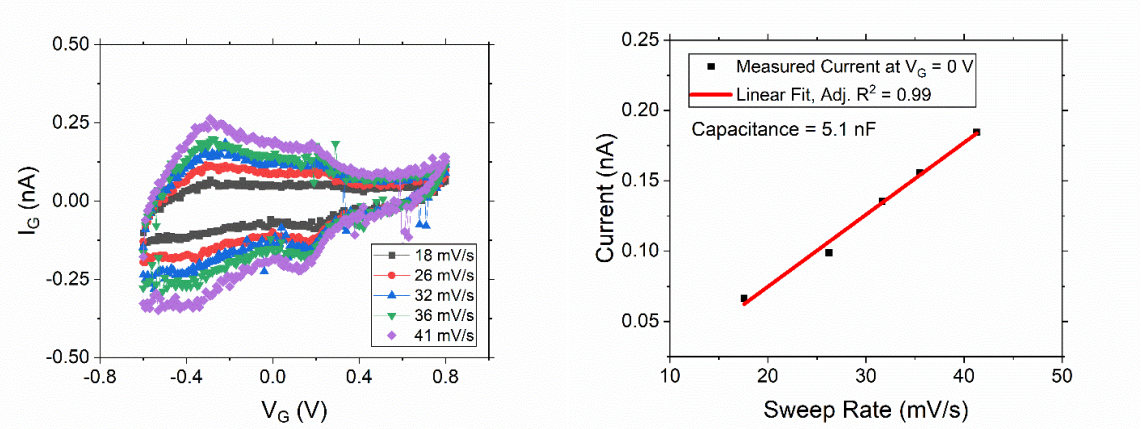

Fig. B.3. Displacement Currents. (a) An example of the displacement current measurements for EGTs with the same specifications as those used in the main text. The source-drain bias is fixed at 0 V, and the gate voltage is swept from 0.8 V to -0.6 V in forward and reverse sweeps. The EGT device has the same dimensions as those in the main text (L = 10 µm, W = 50 µm, Gate = 150x channel area). (b) The current at V_G = 0 V for each sweep is plotted with a linear fit to the data, and the slope yields a capacitance of 5.1 nF, which is the series sum of C_0 and C_1.

Fig 5.11 shows an example of displacement current measurements to obtain the capacitance of C_0 and C_1 (the semiconductor/dielectric and FG1-ion-gel interfaces respectively) in series. This measurement along with the extraction of C_0 and C_1 from the fit of an example EGT allows us to calculate the values of C_0 and C_1 that can be used to predict the gain and sensitivity of the device. The current at V_G = 0 V is plotted against the sweep rate and a linear fit yields a capacitance of 5.1 nF. The average for 3 devices is found to be 5.6 nF and using C_0/C_1 = 4 (extracted from the fit in Fig 5.2), we obtain C_0 = 28 nF, and C_1 = 7 nF. The specific capacitance of the ion-gel-gold interface is calculated to be 9.3 µF/cm^2 using C_1 = 7 nF and the area of gate (FG1) pad. This is lower than the previously reported value of 12.5 µF/cm^2 but is of similar magnitude and the discrepancy could be due to organic contaminants that lower the specific capacitance. The value of C_0, however, is roughly an order of magnitude larger than that predicted by multiplying previously reported

values of specific capacitance with the channel dimensions. This variation in channel capacitance is believed to be largely due to printing differences between studies. While the designed channel in this work is 10 μm x 50 μm, the actual printed film can be 5x larger in effective area, as the printing resolution is about 30 μm and using multiple passes to ensure continuous films can result in both thicker and wider films than the channel dimensions themselves. As the electrochemical transistor relies on volumetric doping of the semiconductor film,[63] larger thicknesses (~2x previous work) and areas (~5x designed channel) can result in capacitances an order of magnitude higher than initially anticipated during electrode design.

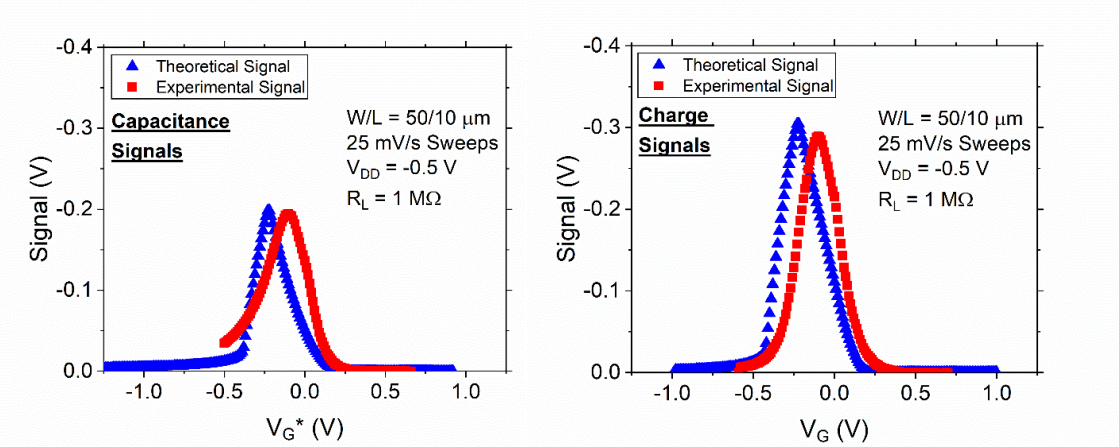

Fig B.4. Theoretical Difference Curves. (a) Signals generated from capacitance-based inputs from experiment (in red) and theory (blue) are shown here. V_G* represents shifting of the inverters to account for differences in starting points for the EGTs. (b) Charge-based signal curves from experiment and theory are shown. The difference in starting point is due to the difference in assumed V_T (as extracted from the control EGT in Fig 5.3a) and the V_T of the device used to calculate the charge signal in this example.

Appendix C – Experimental Protocols

More detailed experimental protocols are written here.

Electrode Deposition:

1. Si/SiO_2 wafers were heated to 115 ^{O}C in the clean room to remove residual moisture

2. Spin coating of S1813 photoresist at 4000 rpm for 30s was carried out after the wafer cools

3. Baking of the wafer at 115 ^{O}C for 1 min was carried out

4. A mask with the desired electrode features, also prepared in the nanofabrication facility, was utilized to expose the wafer for 5s (this was changed depending on the spin coating and resist parameters)

5. Development of the wafer with a 1:5 mixture of 351 developer and water was carried out for approximately 40s or when larger features were clearly visible

6. Rinsing with DI water, drying with nitrogen was completed and inspection of the wafer can confirm presence of the required designs on the wafer

7. E-beam deposition was used to deposit 5 nm Cr and 50 nm Au on the wafers

8. Lift-off was carried out by leaving the gold deposited wafers in commercial 1165 remover or 50:50 by volume mixture of acetone and isopropylalcohol (IPA) overnight

9. Rinsing with acetone, Methanol, and IPA followed by DI water and drying with nitrogen yielded the final electrode patterns

Aerosol Jet Printing:

1. P3HT polymer was mixed with chloroform at 1 mg/mL and magnetically stirred at 400 rpm and 60 ^{O}C, with 2-3 mL of final solution mixed for each run

2. Ion gel was prepared by mixing SEAS polymer, the ionic liquid EMI-TFSI and ethyl acetate in a 1:9:90 ratio by mass. Ion gel was prepared for multiple runs and was stored in air, but with a seal

3. 2 mL of the P3HT solution was loaded into a printing vial (with two glass tubes for entry and exit of carrier gas) with 10% by volume terpineol

4. A 150 μm nozzle was attached to the printer head assembly and the stage heater was switched on and set to 60 ^{O}C. Sonicator and gas flows were also switched on once the tubing was completed

5. The P3HT was printed between the source and drain electrodes (ideally) to a target thickness of 50-75 nm, with observed film color under the printer microscope utilized as an assessment of the film thickness (as observed in previous work)[88]

6. Ion gel is printed to complete the devices to thicknesses that distinguish the centers of the films from the edges on the printer microscope. Being an electrolyte dielectric operated in quasi-static mode, the thickness of the gel does not affect the device operation unless it is too thin

7. Polystyrene (5 mg/mL in chloroform with 1-5% by volume terpineol) was printed to enhance time stability of EGT devices. Only visual confirmation of film continuity is obtained through the printer microscope

PDMS wells and Microfluidic Device Fabrication:

1. Si/SiO_2 wafers were cleaned with a piranha etch, and rinsed with DI water, and baked at 200 ^{O}C for 5 min.

2. SU8 2100 photolithography was carried out on a Si/SiO_2 wafer with a mask containing the microfluidic patterns, following the commercially available data sheet (from www.microchem.com) closely for operating parameters to obtain 100 μm features (a 10% error was observed for feature thickness)

3. Development was carried out with commercial SU8 developer as well

4. HMDS treatment was carried out for 30 min after rinsing with the developer and IPA and drying with nitrogen

5. Al foil was utilized to create a boundary for the wafer to contain the PDMS mixture

6. Sylgaard PDMS monomer and crosslinker were mixed at a 10:1 ratio by mass and centrifuged for 10 min

7. The mixture is poured into the SU8 mold prepared on the wafer and heated in a 75 ^{O}C oven for 2 hours

8. After 2 hours, the crosslinked and solidified PDMS was taken out of the oven and was cut out at the edges so that the border was not

9. For microfluidic devices, a 1 mm punch was utilized to create channels between the features on the bottom and the upper surface, through which fluids can be injected into the device. For wells, the required internal shapes were cut out with a blade

10. Finally the well or device was separated from the remaining PDMS for use

Functionalization:

1. The required thiol molecules (MUA or C8- to C16-thiols) were dissolved at 1 mM concentrations in 200 proof ethanol and shaken lightly until visible dissolution for 1 min

2. For well-based functionalization, these solutions are utilized to fill the PDMS wells close to the brim, and refilled every 10 minutes, or if the solution height dropped to less than 75% of the well height

3. For fluid channel-based functionalization, a syringe was used to fill the microchannel (horizontal, in contact with FG2 surface) and the connecting channel (vertical, made with a punch) to the brim with functionalization solution and refilling pulses were added when the fluid height in the connecting channel reduced to 50% of the channel height

4. At the end of the functionalization period, the well or channel was removed and a well encompassing both FG2 and CG was attached to the wafer and filled with solutions with specific electrolyte concentrations and pH as need for the study

Testing:

1. A custom LabView code was utilized to control Keithley 2400 for application of gate voltages for both transfer and inverter curve measurements at 10 mV or 50 mV step sizes for 25 mV/s or 50 mV/s sweep rates respectively (or other sweep rates utilized)

2. A Keithley 2611B instrument applied drain voltage and measured drain current respectively for transfer curves

3. For inverter curves, a Keithley 2400 applied gate voltages, a Keithley 2611B applied the supply voltage, and a Keithley 2612 instrument measured output voltages

4. A 3 s hold of the drain or supply voltage preceded the application of gate voltage and measurement of current or voltage in both cases to reduce transient currents.